Unterschrift Betreuer

TECHNISCHE UNIVERSITÄT WIEN
Vienna University of Technology

MedAustron

DIPLOMARBEIT

Kommissionierung eines Helium Ionenstrahls im MedAustron Injektorbeschleuniger

Source Branch, LEBT und LINAC

durchgeführt zur Erlangung des akademischen Grades Diplom Ingenieur (Dipl.-Ing.), im Rahmen des Studiums

Masterstudium Technische Physik
Studienkennzahl: 066461

eingereicht an der Technischen Universiät Wien, Atominstitut (ATI)

von

Matthias Kausel, BSc
Mat.Nr.: 01608746

[redacted]

unter der Betreuung von
Privatdoz. Dipl.-Ing. Dr.techn. Michael Benedikt

in Zusammenarbeit mit
EBG MedAustron GmbH
Marie-Curie-Straße 5, 2700 Wiener Neustadt

unter lokaler Betreuung von
Nadia Gambino MSc, PhD

Wien, Dezember 2022

Unterschrift Student

Signature of Supervisor

TECHNISCHE UNIVERSITÄT WIEN
Vienna University of Technology

MedAustron

DIPLOMA THESIS

Helium Beam Commissioning at the Injector of the MedAustron Ion Cancer Treatment Facility

Source Branch, LEBT and LINAC

carried out for the purpose of obtaining the degree of Diplom Ingenieur (Dipl.-Ing.), in the scope of the

Master Programme Technical Physics
Study Code: 066461

submitted at Vienna University of Technology, Atominstitut (ATI)

by

Matthias Kausel, BSc
Mat.Nr.: 01608746

under the supervision of
Privatdoz. Dipl.-Ing. Dr.techn. Michael Benedikt

in collaboration with
EBG MedAustron GmbH
Marie-Curie-Straße 5, 2700 Wiener Neustadt

under local supervision of
Nadia Gambino MSc, PhD

Vienna, December 2022

Signature of Student

Eidesstattliche Erklärung

Ich erkläre an Eides statt, dass die vorliegende Arbeit nach den anerkannten Grundsätzen für wissenschaftliche Abhandlungen von mir selbstständig erstellt wurde. Alle verwendeten Hilfsmittel, insbesondere die zugrunde gelegte Literatur, sind in dieser Arbeit genannt und aufgelistet. Die aus den Quellen wörtlich entnommenen Stellen, sind als solche kenntlich gemacht. Das Thema dieser Arbeit wurde von mir bisher weder im In- noch Ausland einer Beurteilerin/einem Beurteiler zur Begutachtung in irgendeiner Form als Prüfungsarbeit vorgelegt.

Wien, Dezember 2022

Unterschrift Student

Statutory Declaration

I declare that I have authored this thesis independently and performed the associated research myself, using only literature cited in this volume. If text passages from sources are used literally, they are marked as such. I confirm that this work is original and has not been submitted elsewhere for examination, nor is it currently under consideration for a thesis elsewhere.

Vienna, December 2022

Signature of Student

Kurzfassung

Der MedAustron Beschleunigerkomplex in Wiener Neustadt, Österreich, ist ein hochmoderner Ionenbeschleuniger, welcher Ionenstrahlen für klinische Behandlung sowie Forschungszwecke zur Verfügung stellt. Der Komplex basiert auf einem Synchrotron und beschleunigt Protonen auf bis zu 252.7 MeV sowie Kohlenstroffionen auf bis zu 402.8 MeV/u zur klinischen Behandlung. Insgesamt gibt es vier Bestrahlungsräume, wobei drei dem klinischen Betrieb und einer der nicht-klinischen Forschung gewidmet ist. Im nicht-klinischen Bestrahlungsraum steht Protonenstrahl von bis zu 800 MeV zur Verfügung.

In den letzten Jahren wurde die Idee geboren, die dritte vorhandene und bis dahin ungenutzte Ionenquelle zur Erzeugung eines $^4He^{2+}$-Ionenstrahls zu verwenden. Diese Idee manifestierte sich in einem Entwicklungsprojekt mit dem Ziel bis Ende 2024 Heliumstrahl im nicht-klinischen Bestrahlungsraum bereitzustellen. In dieser Diplomarbeit wird die Kommissionierung des Injektorbeschleunigers mit $^4He^{2+}$ präsentiert und diskutiert. Dies beinhaltet die Erzeugung eines stabilen und reproduzierbaren Heliumstrahls durch die ECR Ionenquelle, die Konfiguration der vorhandenen Magnete zur optimalen Injektion in den LINAC sowie das Konfigurieren der LINAC-Elemente für eine optimale Beschleunigung des Ionenstrahls auf 7 MeV/u.

Abstract

The MedAustron facility, located in Wiener Neustadt, Austria, is a state of the art ion acceleration complex, delivering ion beams for cancer treatment and research purposes. The synchrotron-based complex provides proton beams up to 252 MeV and carbon ion beams up to 402.8 MeV/u for cancer treatment. Four irradiation rooms are available, three of which are dedicated to patient treatment and one to non-clinical research. The non-clinical research beamline is also commissioned for proton energies up to 800 MeV.

In recent years, the possibility of using the third available ECR ion source to produce $^{4}He^{2+}$ beam was explored. These efforts ultimately resulted in the initiation of a dedicated development project, which aims for delivering $^{4}He^{2+}$ beam into the non-clinical irradiation room by the end of 2024. Within this diploma thesis, the commissioning strategy and results for the source branch, LEBT and LINAC of the MedAustron injector are presented and discussed. This includes the setup of the ECR ion source to produce a stable high intensity $^{4}He^{2+}$ beam, the setup and optimization of the available magnets for optimum injection into the LINAC as well as the setup and optimization of the LINAC elements for acceleration of the $^{4}He^{2+}$ beam to 7 MeV/u.

Acknowledgements

I want to take the opportunity to thank the people, who made this diploma thesis possible and continuously supported me in various ways. Firstly, I want to thank Nadia Gambino MSc, PhD in her role as my local supervisor at EBG MedAustron GmbH. I greatly appreciate the time and effort put into valuable discussions from which I benefited greatly, not only regarding my education, but also my personal development. Moreover, I want to thank her in the role of project lead of the *HelioS3* project, for allowing me to be a substantial part of the project team as well as putting trust in me and my work. Lastly, I want to thank her for the valuable comments and annotations to this very diploma thesis, which certainly increased its quality substantially. Secondly, I want to thank Dipl.-Ing. Dr. Claus Schmitzer for the continuous support on theoretical as well as technical issues I faced. Furthermore, I want to thank him in his role as lead of the AVID group for the possibility to being employed at EBG MedAustron GmbH for the time it took to execute the required work constituting this diploma thesis. I want to thank Valeria Rizzoglio MSc, PhD for the many valuable discussions, especially in the light of the beam dynamics simulations and data analysis. Furthermore, I want to thank her for the good collaboration within the commissioning shifts. I want to thank Dr. Eng. Liviu Penescu for the good collaboration during the commissioning shifts as well as valuable inputs based on his vast experience in the field of accelerator beam commissioning. Furthermore, I want to thank the members of the AVID group at EBG MedAustron GmbH, which through their continuous technical support made the helium commissioning, and thus this diploma thesis, possible in the first place. Of course, I want to thank Privatdoz. Dipl.-Ing. Dr.techn. Michael Benedikt for supervising this diploma thesis and providing the excellent particle accelerator lecture at the Vienna University of Technology, which allowed for a profound first understanding of the working principles of particle accelerators. Furthermore, I want to thank DDipl.-Ing. Dr.techn. Elisabeth Renner for correcting and proofreading this diploma thesis. I want to thank my friend and flatmate Dipl.-Ing. Jakob Sam, BA for helping me out in the creation of the figures for the accelerator physics chapter. Further, I want to thank my sister Dipl.-Ing. Alexandra Kausel and my friend Matthias Danner, BSc for proofreading this diploma thesis. Last, but not least, I want to thank my whole family for continuously supporting me throughout my studies, which I could certainly not have done without them.

Contents

1 Introduction

1.1 Ion Therapy Cancer Treatment

Over the last few decades ion therapy became an established alternative to conventional photon or electron irradiation cancer treatment. Compared to photon or electron irradiation therapy, which deposits most of the dose right after the skin, ion therapy allows for the efficient deposition of dose within the tumor while causing minimal damage to the surrounding healthy tissue. This is possible due to the fact that the interaction of the ions with the tissue results in a peak-like deposition of dose after a certain penetration depth. The exact shape and penetration depth of this so-called Bragg peak depends on the employed particle type and the incident energy. Consequently, by scanning over several incident ion beam positions and energies, the Bragg peak behavior allows to deposit the desired dose precisely within the tumor [1].

According to the Particle Therapy Co-Operative Group (PTCOG) [2], by the end of 2021, over 325 thousand patients have been treated with particle therapy. Overall, 280 thousand patients were treated with proton beam. Treatment with carbon ions amounts to around 42 thousand people, while only approximately 3500 patients were treated with other particle types.

1.2 Helium Ion Therapy

Besides the well-established proton and carbon ion therapy, alternative ions, such as helium, are actively explored for potential clinical application. Historically, helium ion therapy has not been researched extensively. Even though successful clinical trials were carried out at the Lawrence Berkeley National Laboratory as early as 1975 [3], with the trial shutdown and the establishment of proton and carbon ion radiotherapy, helium ion therapy moved into the background and active research came to a halt. However, according to recent studies [4], irradiation with helium ions could offer some favorable physical and biological properties for cancer treatment, that render it very interesting for modern oncology. Consequently, the general interest in helium ion beams for research

purposes, and in the long-term clinical cancer treatment, is growing again. Commissioning efforts at Heidelberg Ion-Beam Therapy Center (HIT) allowed for the first irradiation with helium in October 2021 [5]. However, with only a few facilities world-wide capable of delivering suitable helium ion beam, the availability is limited. Consequently, an opportunity arises for ion treatment facilities to be at the forefront of research in the field of helium ion therapy.

The MedAustron Ion Therapy Center provides clinical proton and carbon beam for cancer treatment as well as research purposes. With an unused third ion source available at the facility, the idea of also providing helium beam at the MedAustron facility has emerged recently. Within a first commissioning effort, helium beam is planned to be available for non-clinical research applications by the end of 2024. At the time of the writing, a potential clinical application at the MedAustron facility is still to be evaluated. Once available, the MedAustron ion therapy center will be among one of the few facilities that provide helium ions for research and clinical studies.

1.3 MedAustron Ion Therapy Center

The conducted work constituting this diploma thesis has been carried out in cooperation with EBG MedAustron GmbH. EBG MedAustron GmbH was founded in 2007 to construct and operate the MedAustron ion cancer therapy and research facility in Wiener Neustadt, Lower Austria. With its proximity to Vienna and the local hospital, the facility is easily accessible to patients as well as researchers and staff. The MedAustron ion treatment center stands out as it is one of few facilities worldwide that offers both proton and carbon treatment.

The EBG MedAustron GmbH was founded as a medical adaptation of the suggested AUSTRON project, which intended to establish a research center for various disciplines as early as 1990 [6]. Soon after the foundation of EBG MedAustron GmbH collaborations with CERN in Geneva, INFN in Rome as well as CNAO in Pavia were established in order to utilize the latest know-how in particle acceleration and ion therapy. The groundbreaking of the MedAustron facility took place in March 2011. After the completion of the building, the installation and the initial commissioning of the accelerator as a medical product, the first patient was treated with proton beam in December 2016. The development and parallel commissioning to clinical operation enabled for the first treatment with carbon ions in July 2019.

The accelerator layout of the MedAustron ion cancer treatment facility is shown in Fig. 1.1. Three identical ion sources are installed at the facility, two of which are used for clinical treatment. In agreement with the MedAustron naming convention [8], the sources will be referred to as S1, S2 and S3 within this diploma thesis. S1 and S2 are used to generate protons and carbon ions, respectively. S3, however, is not used for clinical treatment up to now and allows for parallel research and development activities.

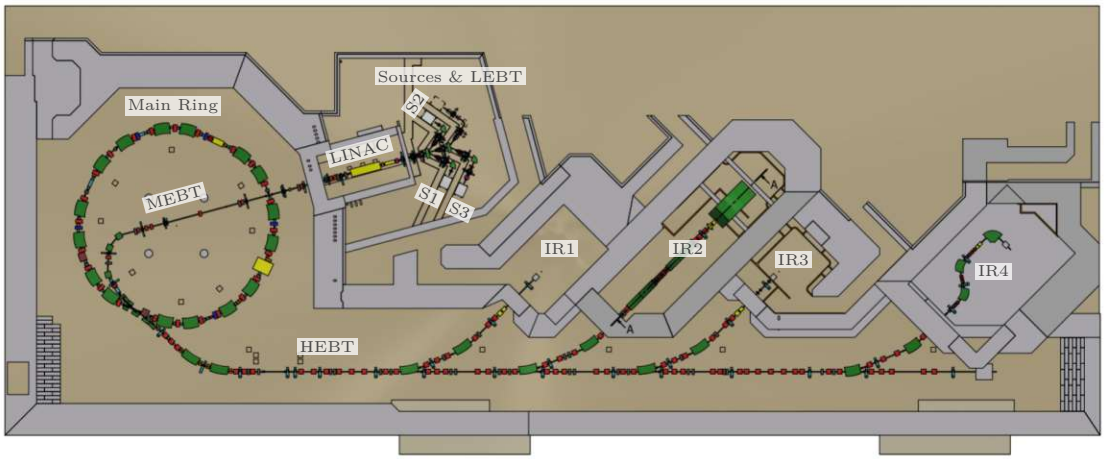

Fig. 1.1: MedAustron accelerator layout (adapted from [7]).

Proton and carbon beams are extracted at an energy of 8 keV/u from the respective ion source. After passing a spectrometer magnet to select the desired charge state and filter unwanted ion species, the particles are transported to the Low Energy Beam Transfer Line (LEBT). The beam is then pulsed and injected into the Linear Accelerator (LINAC), where the beam pulse is bunched and accelerated to 7 MeV/u. Further transport through the Medium Energy Beam Transfer Line (MEBT) and consequent injection into the Main Ring (synchrotron) allows for an acceleration to the clinical energies of 62.4 MeV to 252.7 MeV for proton beam and 120 MeV/u to 402.8 MeV/u for carbon ions. At the desired energy, the particles are extracted via a betatron core driven slow extraction mechanism. After the extraction from the Main Ring, the beam is transported through the High Energy Beam Transfer Line (HEBT) into one of the four irradiation rooms. The first room, IR1 is dedicated to Non-Clinical Research (NCR) activities. It is primarily used by the Vienna University of Technology, the Institute for High Energy Physics of the Austrian Academy of Sciences (HEPHY) and the Medical University of Vienna. The other three irradiation rooms, IR2, IR3 and IR4, are used for clinical treatment. IR2 is capable of horizontal and vertical irradiation, while IR3 is equipped with only a horizontal beamline. A proton gantry is available in IR4.

In the context of this diploma thesis, it is useful to the introduce the MedAustron injector in more detail. The injector layout is shown in Fig. 1.2. The S3 branch (1 in Fig. 1.2) consists of the third electron cyclotron resonance ion source (ECRIS), from which ion beam can be extracted with energies up to few keV/u. A focus electrode, located within the source extraction system, as well as a solenoid and quadrupole magnet allow for a focusing of the desired ion beam onto the spectrometer dipole magnet. Furthermore, two corrector dipole magnets are available in order to optimize the beam steering. Within the S3 branch and immediately after the spectrometer magnet, beam diagnostic devices, such as Faraday cups, wire scanner profile monitors and movable slit plates are installed. The LEBT (2 in Fig. 1.2) mostly consists of quadrupole triplets and corrector dipoles,

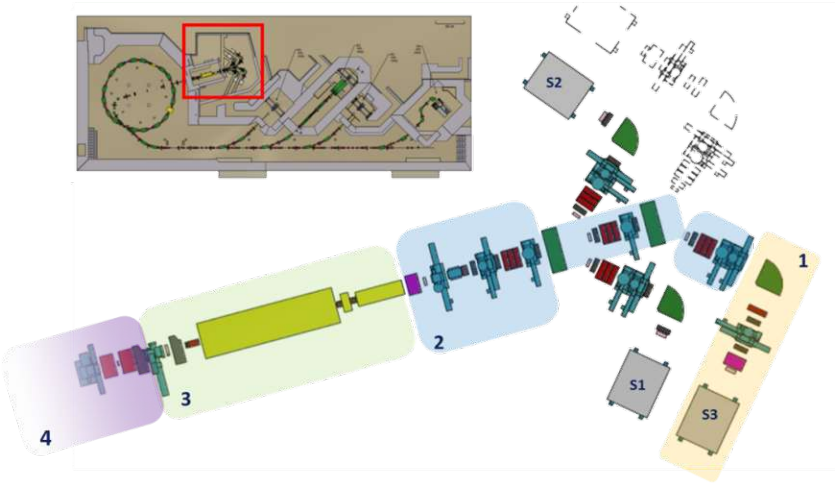

Fig. 1.2: MedAustron injector layout (adapted from [7]).

which are used to optimize the beam transport and injection into the LINAC. Switching dipole magnets are installed at the intersection of the different source branches. These dipole magnets allow to efficiently switch the source that injects the beam into the common beam lines. Similarly to the source branch, the LEBT features Faraday cups, wire scanners and movable slit plates. At the end of the LEBT the beam is pulsed into macropulses of up to 50 µs by an electrostatic deflector. The intensity after the pulsing can be measured non-invasively via a current transformer. A solenoid magnet allows for the focusing of the beam into the radio frequency quadrupole (RFQ), which is the first acceleration element of the LINAC section (3 in Fig. 1.2). The RFQ accelerates the ions to energies of several hundred keV/u, while bunching the macropulse into microbunches of a few nanoseconds in length. The accelerated beam traverses the Intertank Matching Section (IMS), where the beam intensity can be measured via a current transformer. In the IMS, quadrupole doublets and corrector dipoles allow for the optimized injection into the interdigital H-mode drift tube LINAC (IH-DTL). The IH-DTL, which is also referred to as interdigital H-mode (IH)-tank, accelerates the ions up to energies of a few MeV/u. Three quadrupole triplets within the IH-tank allow to compensate for the defocusing effects present within DTL structures. After the IH-tank, the beam can be characterized via Faraday cups, profile grid monitors, movable slits and current transformers. A stripping foil allows to change the charge state for specific ion types. The energy of the beam can be measured via time of flight (TOF) measurements within the MEBT.

1.4 Overview

This diploma thesis focuses on the description of the $^4He^{2+}$ ion beam commissioning process within the S3 branch, the LEBT and the LINAC of the MedAustron accelerator complex. It is structured as following. Firstly, in chapter 2, the fundamentals of accelerator physics as well as the functionality of some special devices within the MedAustron injector are discussed. In chapter 3, the employed commissioning tools are presented. The core of this diploma thesis is the discussion of the commissioning strategies and results within the S3 branch, LEBT and LINAC in chapter 4, 5 and 6, respectively. In each of these chapters, a brief introduction is given, which shall highlight the individual challenges of the commissioning process in the respective part of the accelerator. This is followed by the initial setup and the optimizations applied. The commissioned setpoint is characterized and the stability and reproducibility is discussed. The main achievements are summarized and future perspectives are assessed within chapter 7.

2 Accelerator Physics Basics

In this chapter the basic functionality of the different beam lattice devices installed in the source branch, the LEBT and the LINAC of the MedAustron injector are discussed. This includes the general description of charged particle motion in drift spaces, dipole, quadrupole and solenoid magnets within the framework of transverse linear beam dynamics as well as the fundamentals of beam generation via ECRIS and acceleration via radio frequency (RF) devices, such as the RFQ and LINAC. A proper understanding of the underlying working principles is crucial for the interpretation of the simulation and experimental results presented in chapter 4, 5 and 6.

2.1 Transverse Linear Beam Dynamics

Transverse beam dynamics describes the transverse particle motion inside a beam lattice. It emerges naturally from the consideration of a curvilinear reference system along the beamline (see Fig. 2.1) and, within linear approximation, simple and efficient solutions to the equations of motion can be found. The general equations of motion in the curvilinear reference system are derived from the Lorentz force and given by the following expressions. A derivation of these equations of motion can be found in Appendix A and [10].

$$\begin{aligned} x'' - h\kappa_x - \frac{\sigma''}{\sigma'}x' &= \frac{q\sigma'}{p}(y'B_s - hB_y) \\ y'' - h\kappa_y - \frac{\sigma''}{\sigma'}y' &= -\frac{q\sigma'}{p}(x'B_s - hB_x) \\ x'\kappa_x + y'\kappa_y + h' - \frac{\sigma''}{\sigma'}h &= \frac{q\sigma'}{p}(x'B_y - y'B_x) \end{aligned} \tag{2.1}$$

Here, x and y are the transverse coordinates and s is the longitudinal coordinate of the curvilinear reference system. The derivatives are with respect to the longitudinal coordinate s, which parameterizes the ideal beam path trajectory. The parameter σ parameterizes the real beam trajectory (see Fig. 2.1). The abbreviation $h = 1+\kappa_x x+\kappa_y y$ is used, where $\kappa_x = \frac{1}{\rho_x}$ and $\kappa_y = \frac{1}{\rho_y}$ are the curvatures of the ideal beam trajectory

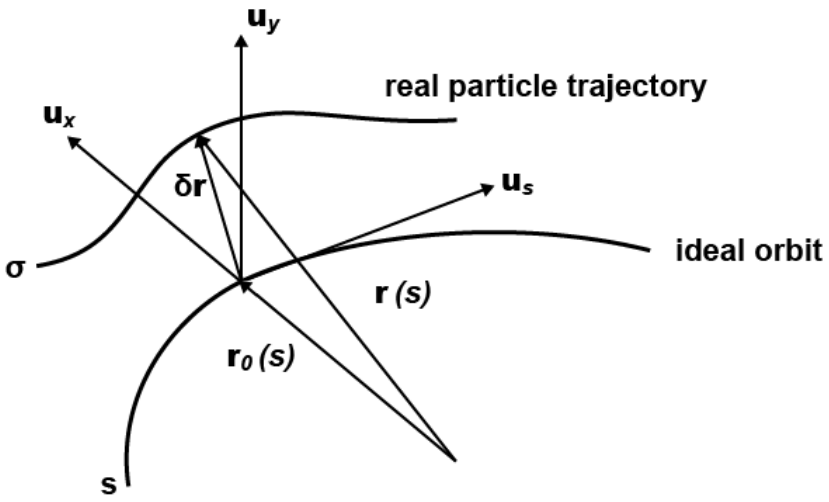

Fig. 2.1: Illustration of the curvilinear reference system. The orthogonal unit vectors $\boldsymbol{u}_x$,$\boldsymbol{u}_y$ and $\boldsymbol{u}_s$ are moving along the designed orbit parameterized by s, whereas the real particle moves along another trajectory parameterized by σ. Each point on the real particle trajectory can be uniquely identified by a position vector on the design orbit $\boldsymbol{r}_0$ and a linear combination of the transverse unit vectors $\delta\boldsymbol{r} = x\boldsymbol{u}_x + y\boldsymbol{u}_y$. Adapted from Fig. 4.2 in [9].

with the local bending radii $\rho_{x,y}$. The magnetic field is given in curvilinear reference system coordinates $\boldsymbol{B} = (B_x, B_y, B_s)$. The solution to this set of differential equations is complicated, especially as the equations of motion depend on parameters that are not very intuitive and not easily accessible to measurements. For a lattice comprising only dipole and quadrupole magnets, one can linearize the equations of motion by considering only the transverse magnetic fields, i.e. $B_s = 0$, and expanding up until the quadrupole term. By further considering only lattices which do not feature bending in the vertical plane, the equations of motion can be approximated by

$$\begin{aligned} x'' + K_x(s)x &= A_x(s)\delta \\ y'' - K_y(s)y &= 0. \end{aligned} \tag{2.2}$$

Here, $\delta = \frac{\Delta p}{p_0}$ is the fractional offset from the reference momentum. The focusing strengths $K_x(s)$, $K_y(s)$ and the dispersive term $A(s)$ depend on the properties of the beam lattice element. In principle, these functions can have an arbitrary dependence on s. For the assumption of ideal dipole and quadrupole magnets, $K_x(s)$, $K_y(s)$ and $D(s)$ correspond to piecewise constant functions of the curvature κ_x and the normalized magnetic field gradient K_0.

$$K_x(s) = \begin{cases} 0 & \text{for drift spaces} \\ \kappa_x^2 & \text{for dipole magnets} \\ K_0 & \text{for quadrupole magnets} \end{cases}$$

$$K_y(s) = \begin{cases} 0 & \text{for drift spaces} \\ 0 & \text{for dipole magnets} \\ K_0 & \text{for quadrupole magnets} \end{cases} \tag{2.3}$$

$$A_x(s) = \begin{cases} 0 & \text{for drift spaces} \\ \kappa_x & \text{for dipole magnets} \\ 0 & \text{for quadrupole magnets} \end{cases}$$

2.1.1 Single Particle Solutions and Matrix Formalism

The advantage of the fully linearized equations of motion in Eq. (2.2) is that they only depend on the magnetic field configuration and can be solved analytically. In the following section, which is largely based on [11] and [10], the equations of motion are solved and the solutions are discussed for simple drift spaces, ideal dipole and quadrupole magnets. Note that within transverse linear beam dynamics only fields up to quadrupole order are considered, as higher order terms would lead to non-linear contributions to the equations of motion.

Drift Spaces

Drift spaces are characterized as regions of no electric and magnetic fields. In the absence of a magnetic field K_x and K_y vanish according to Eq. (2.3) and thus the equations of motion in Eq. (2.2) can be integrated easily with the initial positions x_0, y_0 and the initial angles with respect to the ideal beam trajectory x_0', y_0'.

$$\begin{aligned} x(s) &= x_0 + x_0' s \\ x'(s) &= x_0' \end{aligned} \qquad \begin{aligned} y(s) &= y_0 + y_0' s \\ y'(s) &= y_0' \end{aligned} \tag{2.4}$$

The motion of a single particle is uniform and non-accelerated as it is not subjected to any external force. The solution can also be written in terms of a matrix-vector multiplication. The mapping from the initial state vector $\boldsymbol{u}_0$ to the one of interest $\boldsymbol{u}(s)$ is called transfer matrix and denoted by $\boldsymbol{M}_{\text{Drift}}$.

$$\boldsymbol{u}(s) = \boldsymbol{M}_{\text{Drift}}\,\boldsymbol{u}_0 \tag{2.5}$$

This equation may be written in terms of components, which allows for the identification of the transfer matrix $\boldsymbol{M}_{\text{Drift}}$,

$$\begin{pmatrix} x(s) \\ x'(s) \\ y(s) \\ y'(s) \end{pmatrix} = \underbrace{\begin{pmatrix} 1 & s & 0 & 0 \\ 0 & 1 & 0 & 0 \\ 0 & 0 & 1 & s \\ 0 & 0 & 0 & 1 \end{pmatrix}}_{\boldsymbol{M}_{\text{Drift}}} \begin{pmatrix} x_0 \\ x_0' \\ y_0 \\ y_0' \end{pmatrix}. \tag{2.6}$$

Dipole Magnets

By considering the homogeneous magnetic field within ideal horizontal dipole magnets, one obtains $K_x = \kappa_x^2 > 0$ and $K_y = 0$. In this case the horizontal equation of motion becomes the differential equation of a harmonic oscillator, while the vertical equation is equivalent to the one of a drift space. Consequently, the solutions to the equation of motion are given by the following expressions.

$$\begin{aligned} x(s) &= \cos\left(|\kappa_x|\, s\right) + \frac{1}{|\kappa_x|}\sin\left(|\kappa_x|\, s\right) + \frac{1}{\kappa_x}\delta \\ x'(s) &= -|\kappa_x|\sin\left(|\kappa_x|\, s\right) + \cos\left(|\kappa_x|\, s\right) \\ \\ y(s) &= y_0 + y_0' s \\ y'(s) &= y_0' \end{aligned} \tag{2.7}$$

In contrast to the drift space, these solutions cannot be written in terms of a matrix-vector multiplication in the four dimensional transverse phase space. This is due to the dispersive term $\frac{1}{\kappa_x}\delta$. This problem can be eliminated by adding the fractional momentum offset δ as a phase space variable. Then the transfer matrix for dipole magnets $\boldsymbol{M}_{\text{Dipole}}$ is defined by the following matrix equation.

$$\begin{pmatrix} x(s) \\ x'(s) \\ y(s) \\ y'(s) \\ \delta \end{pmatrix} = \underbrace{\begin{pmatrix} \cos\left(|\kappa_x|\, s\right) & \frac{1}{|\kappa_x|}\sin\left(|\kappa_x|\, s\right) & 0 & 0 & \frac{1}{\kappa_x} \\ -|\kappa_x|\sin\left(|\kappa_x|\, s\right) & \cos\left(|\kappa_x|\, s\right) & 0 & 0 & 0 \\ 0 & 0 & 1 & s & 0 \\ 0 & 0 & 0 & 1 & 0 \end{pmatrix}}_{\boldsymbol{M}_{\text{Dipole}}} \begin{pmatrix} x_0 \\ x_0' \\ y_0 \\ y_0' \\ \delta \end{pmatrix} \tag{2.8}$$

The curvature of the beam trajectory is proportional to the vertical magnetic field B_y according to $\kappa_x = \frac{q}{p}B_y$ (see also Eq. (A.18) in Appendix A). Therefore, dipole magnets

can be used to steer the beam along a predefined path. The argument of the trigonometric functions in the solution can be identified as the bending angle $\theta = \kappa_x s = s/\rho_x$. Apart from defining the ideal beam trajectory, dipoles can also be used to correct the real particle trajectory both horizontally and vertically. Corrector dipoles can equivalently be described by the matrix formalism. However, the transfer matrix $\boldsymbol{M}_{\text{Dipole}}$ only describes dipoles with vertical magnetic field, thus curving the trajectory in the horizontal plane as this assumption was used in the derivation of the linearized equations of motion. It can be shown that the differential equations for vertical dipoles are identical to the horizontal ones when x and y are swapped (see Eq. (A.33) with only $\kappa_y \neq 0$ in Appendix A). Hence, it is immediately possible to write down the transfer matrix for a vertical bending dipole magnet by exchanging the solutions for the horizontal and vertical axis.

$$\boldsymbol{M}^{\text{ver}}_{\text{Dipole}} = \begin{pmatrix} 1 & s & 0 & 0 & 0 \\ 0 & 1 & 0 & 0 & 0 \\ 0 & 0 & \cos\left(|\kappa_y|\, s\right) & \frac{1}{|\kappa_y|}\sin\left(|\kappa_y|\, s\right) & \frac{1}{\kappa_y} \\ 0 & 0 & -\kappa_y \sin\left(|\kappa_y|\, s\right) & \cos\left(|\kappa_y|\, s\right) & 0 \end{pmatrix}. \tag{2.9}$$

Quadrupole Magnets

Due to the Maxwell equations for stationary magnetic fields in vacuum (see Eq. (A.30) in Appendix A) the gradients in the horizontal and in the vertical direction are not independent. The simplest inhomogeneous magnetic field configuration that fulfills the requirement of the Maxwell equations is the quadrupole field with a constant field gradient g. The magnetic field configuration inside a quadrupole can be written as follows.

$$B_x = gy, \qquad B_y = gx \tag{2.10}$$

An illustration of the magnetic field configuration can be seen in Fig. 2.2. The correspondence to the normalized gradient K_0 is given by the magnetic rigidity $B\rho$ (see Eq. (A.21) in Appendix A for more details) and can be written as

$$g = B\rho K_0 = \frac{p_0}{q} K_0. \tag{2.11}$$

Due to the equality of the magnetic gradients, one only has to consider two different cases in the analysis of quadrupole magnets, namely $K_0 > 0$ and $K_0 < 0$. If one considers $K_0 > 0$, the solution of the equations of motion is given by

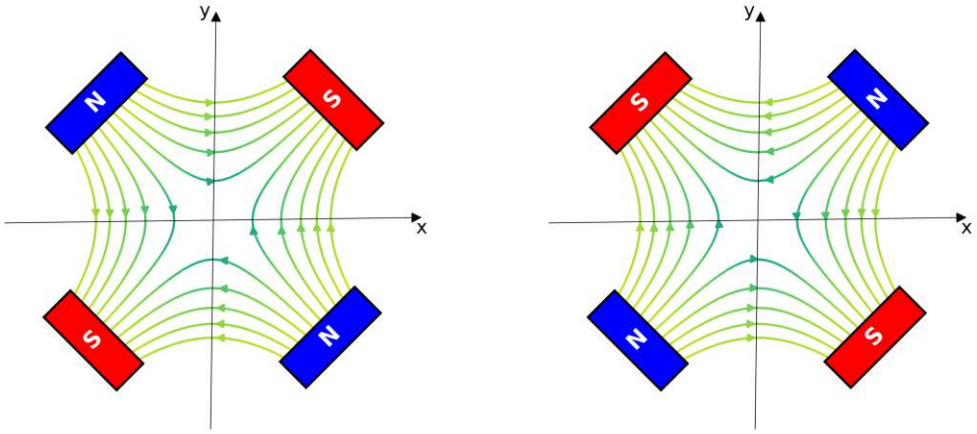

Fig. 2.2: Schematic of quadrupolar fields with positive (left) and negative (right) field gradient. Inspired by Fig. 7 in [10].

$$
\begin{aligned}
x(s) &= x_0 \cos\left(\sqrt{K_0}s\right) + x_0' \frac{1}{\sqrt{|K_0|}} \sin\left(\sqrt{K_0}s\right) \\
x'(s) &= -x_0 \sqrt{K_0} \sin\left(\sqrt{K_0}s\right) + x_0' \frac{1}{\sqrt{|K_0|}} \cos\left(\sqrt{K_0}s\right) \\
y(s) &= y_0 \cosh\left(\sqrt{K_0}s\right) + y_0' \frac{1}{\sqrt{|K_0|}} \sinh\left(\sqrt{K_0}s\right) \\
y'(s) &= y_0 \sqrt{K_0} \sinh\left(\sqrt{K_0}s\right) + y_0' \frac{1}{\sqrt{|K_0|}} \cosh\left(\sqrt{K_0}s\right).
\end{aligned}
\tag{2.12}
$$

It is evident, that for positive K_0, the quadrupole magnet focuses in the horizontal plane and defocuses in the vertical plane. Conventionally, such quadrupole magnets are called focusing quadrupoles, even though they only focus in the horizontal plane. Quadrupole magnets with negative K_0 are referred to as defocusing as they defocus the beam in the horizontal and focus it in the vertical plane. Furthermore, it is evident from the solution in Eq. (2.12) that ideal quadrupoles do not introduce any dispersion within linear beam dynamics, which again allows for a description in four-dimensional transverse phase space without the dispersion. The transfer matrix for a focusing quadrupole magnet can be identified as

$$\boldsymbol{M}^{\mathrm{F}}_{\mathrm{Quad}} = \begin{pmatrix} C(s) & \frac{1}{\sqrt{K_0}}S(s) & 0 & 0 \\ -\sqrt{K_0}S(s) & C(s) & 0 & 0 \\ 0 & 0 & Ch(s) & \frac{1}{\sqrt{|K_x|}}Sh(s) \\ 0 & 0 & \sqrt{K_0}Sh(s) & Ch(s) \end{pmatrix}. \tag{2.13}$$

Here, the abbreviations $C(s) = \cos(\sqrt{K_0}s)$, $S(s) = \sin(\sqrt{K_0}s)$, $Ch(s) = \cosh(\sqrt{K_0}s)$ and $Sh(s) = \sinh(\sqrt{K_0}s)$ have been used. For defocusing quadrupoles with $K < 0$ the transfer matrix can be written as

$$\boldsymbol{M}^{\mathrm{D}}_{\mathrm{Quad}} = \begin{pmatrix} Ch(s) & \frac{1}{\sqrt{K_0}}Sh(s) & 0 & 0 \\ -\sqrt{K_0}Sh(s) & Ch(s) & 0 & 0 \\ 0 & 0 & C(s) & \frac{1}{\sqrt{|K_x|}}S(s) \\ 0 & 0 & \sqrt{K_0}S(s) & C(s) \end{pmatrix}. \tag{2.14}$$

It can be shown that certain combinations of quadrupole magnets with different gradients are capable of achieving a net focusing of the beam in both planes [12].

Coupled Motion in Solenoidial Magnetic Fields

In order to describe particle movement in solenoid magnets, one cannot use the linearized equations of motion in Eq. (2.2) as the longitudinal magnetic field has been set to zero in their derivation. Consequently, one has to go back to the most general form of the equations of motion in a curvilinear reference system given by Eq. (2.1) and set B_x and B_y as well as κ_x and κ_y to zero. This can be done as an ideal solenoid magnet is assumed to only have longitudinal field components. Under the assumption of a uniform magnetic field, linearization similar to the one used to derive Eq. (2.2) yields

$$\begin{aligned} x''(s) &= \frac{q}{p_0}(1-\delta)B_s y'(s) \\ y''(s) &= -\frac{q}{p_0}(1-\delta)B_s x'(s). \end{aligned} \tag{2.15}$$

These equations of motion are coupled and consequently the coordinates of the planes influence each other. However, it turns out that a decoupling can be achieved by a rotation of the coordinate system. The rotation angle increases directly proportional to the longitudinal position within the magnet $(s - s_0) \rightarrow s$, where the beam entry point of the magnet is chosen at $s_0 = 0$ for simplicity. This corresponds to a continuous change of basis within the magnet as the basis vectors and thus the coordinates rotate uniformly depending on the position within the solenoid magnet. In order to achieve the decoupling via coordinate system rotation the coordinates x and y are written in

complex form and subsequently rotated in the complex plane. The coordinates of the rotated coordinate system are referred to as v and w.

$$(x+iy) \quad \rightarrow \quad R := (x+iy)e^{-i\Phi s} = v + iw \quad \Leftrightarrow \quad (x+iy) = Re^{i\Phi s} \tag{2.16}$$

Here, the abbreviation $\Phi = -\frac{1}{2}\frac{q}{p_0}B_s(1-\delta)$ is introduced. The equation of motion for the complex variable $(x+iy)$ is given by

$$(x+iy)'' + i\frac{q}{p_0}B_s(x+iy)' = 0 \quad \rightarrow \quad (x+iy)'' - 2i\Phi(x+iy)' = 0. \tag{2.17}$$

Splitting of real and imaginary part of this equation yields the equations of motion in Eq. (2.15) again. The derivatives of Eq. (2.16) can be explicitly calculated.

$$\begin{aligned} (x+iy)' &= R'e^{i\Phi s} + i\Phi Re^{i\Phi s} \\ (x+iy)'' &= R''e^{i\Phi s} + 2i\Phi R'e^{i\Phi s} - \Phi^2 Re^{i\Phi s} \end{aligned} \tag{2.18}$$

Insertion of Eq. (2.18) into the complex differential equation Eq. (2.17) and considering that the division through $e^{i\Phi s}$ is possible for every s yields the following expression.

$$R'' + \Phi^2 R = 0 \quad \rightarrow (w+iv)'' + \Phi^2(w+iv)' = 0. \tag{2.19}$$

Separate consideration of the real and imaginary part of this equation yields two uncoupled equations of motion in the rotated reference frame.

$$\begin{aligned} w'' + \Phi^2 w &= 0 \\ v'' + \Phi^2 v &= 0 \end{aligned} \tag{2.20}$$

Note, that these equations are equivalent to the equations of motion for the focusing plane of a quadrupole magnet. In order to develop a matrix formalism for solenoid magnets, one has to consider two aspects. Firstly, the dispersion does not enter linearly into the solution anymore. As a result it is not possible to treat the dispersion within the matrix formalism. For the sake of only providing a basic understanding, the dispersion will be disregarded and a four dimensional phase space $\boldsymbol{u} = (x, x', y, y')^T$ will be considered. Secondly, the uncoupled equations of motion are not given in the usual horizontal and vertical coordinates, but in a rotating reference system, which turns counter clockwise with increasing longitudinal position s. As it was already stated that the solenoid acts like a quadruple magnet in the rotating reference system, the 4×4 transfer matrix of a solenoid magnet can be split into a quadrupole like focusing transformation followed by a rotation into the transverse coordinates of the curvilinear reference system as follows.

$$\boldsymbol{u}(s) = \boldsymbol{M}_{\mathrm{R}}\boldsymbol{M}_{\mathrm{F}}\boldsymbol{u}_0 \tag{2.21}$$

The focusing matrix $\boldsymbol{M}_{\mathrm{F}}$ can be derived immediately, due to its similarity to the quadrupole transfer matrix.

$$\boldsymbol{M}_{\mathrm{F}} = \begin{pmatrix} \cos(\Phi s) & -\frac{1}{\Phi}\sin(\Phi s) & 0 & 0 \\ \Phi\sin(\Phi s) & \cos(\Phi s) & 0 & 0 \\ 0 & 0 & \cos(\Phi s) & -\frac{1}{\Phi}\sin(\Phi s) \\ 0 & 0 & \Phi\sin(\Phi s) & \cos(\Phi s) \end{pmatrix} \tag{2.22}$$

The rotation matrix $\boldsymbol{M}_{\mathrm{R}}$ can be derived from the definition Eq. (2.16), its derivative Eq. (2.18) and the Euler formula for the complex exponential function.

$$\boldsymbol{M}_{\mathrm{rot}} = \begin{pmatrix} \cos(\Phi s) & 0 & \sin(\Phi s) & 0 \\ \Phi\sin(\Phi s) & \cos(\Phi s) & -\Phi\cos(\Phi s) & \sin(\Phi s) \\ -\sin(\Phi s) & 0 & \cos(\Phi s) & 0 \\ -\Phi\cos(\Phi s) & -\sin(\Phi s) & \Phi\sin(\Phi s) & \cos(\Phi s) \end{pmatrix} \tag{2.23}$$

Consequently, the full transformation is given by the following expression.

$$\boldsymbol{M}_{\mathrm{sol}} = \begin{pmatrix} \cos^2(\Phi s) & -\frac{1}{2\Phi}\sin(2\Phi s) & \frac{1}{2}\sin(2\Phi s) & -\frac{1}{\Phi}\sin^2(\Phi s) \\ \Phi\sin(2\Phi s) & \cos(2\Phi s) & -\Phi\cos(2\Phi s) & \sin(2\Phi s) \\ -\frac{1}{2}\sin(2\Phi s) & \frac{1}{\Phi}\sin^2(\Phi s) & \cos^2(\Phi s) & -\frac{1}{2\Phi}\sin(2\Phi s) \\ \Phi\cos(2\Phi s) & -\sin(2\Phi s) & \Phi\sin(2\Phi s) & \cos(2\Phi s) \end{pmatrix} \tag{2.24}$$

More details on the transverse dynamics within solenoids can be found in [13] on which this section is based.

2.1.2 General Solution to the Equations of Motion

While the matrix formalism is a simple and straight-forward way to solve the linearized equations of motion for charged particles in a beam lattice, it does not give much insight into the beam dynamics itself. However, especially for periodic beam lattices, the large amount of full turns of a particle in circular accelerators renders the matrix formalism impractical for calculations. Therefore, it is useful to study the general solution of the linearized equations of motion. In the following section the notation $u = x, y$ will be introduced and dispersive effects will be neglected. As a consequence, the linearized horizontal equation of motion is given by

$$u''(s) + K_u(s)u(s) = 0. \tag{2.25}$$

This differential equation is a Hill-type differential equation [14]. The conventional form of the solution used in accelerator physics is given by

$$u(s) = \sqrt{\epsilon}\sqrt{\beta(s)}\cos\left(\mu(s) + \phi\right). \tag{2.26}$$

This equation describes a non-trivial oscillation in the position $u(s)$. The integration constants, ϵ (emittance) and ϕ (initial phase offset), are constants of motion as they are independent of s and thus also time independent. The beta function $\beta(s)$ is determined by $K_u(s)$, i.e. the magnet strengths. Furthermore, the amplitude of the oscillation $u_{\max} = \sqrt{\epsilon\beta(s)}$ evolves throughout the beam lattice. A relation between the phase advance of the oscillation $\mu(s)$ and the beta function $\beta(s)$ can be found by inserting the solution given in Eq. (2.26) into the Hill differential equation in Eq. (2.25).

$$\beta(s)\mu'(s) = 1 \tag{2.27}$$

Consequently, the phase advance is given by

$$\mu(s) = \int_{s_0}^{s} \frac{ds'}{\beta(s')}. \tag{2.28}$$

The integration variable name is chosen to be s' in order to differentiate it from the upper bound of the integral s. For periodic structures, the phase advance over a full circumference is called tune Q, which is an important property to the resonance behavior of the oscillations. While the tune is not a crucial parameter in the injector section of the accelerator and thus not really relevant for this thesis, it is essential for the acceleration and extraction of synchrotrons and is mentioned for completeness.

$$Q = \frac{1}{2\pi}\oint \frac{ds}{\beta(s)} \tag{2.29}$$

As a next step the motion of the particle in phase space will be discussed. The derivative of the position $u'(s)$ is calculated as

$$u'(s) = -\sqrt{\frac{\epsilon}{\beta(s)}}\left[\alpha(s)\cos\left(\mu(s) + \phi\right) + \sin\left(\mu(s) + \phi\right)\right]. \tag{2.30}$$

Here, the alpha function $\alpha(s) = -\frac{1}{2}\beta'(s)$ has been introduced. The derivative $u'(s)$ can now be expressed via $u(s)$ by insertion of Eq. (2.26).

$$u'(s) = -\frac{\alpha(s)}{\beta(s)}u(s) - \sqrt{\frac{\epsilon}{\beta(s)}}\sin\left(\mu(s) + \phi\right) \tag{2.31}$$

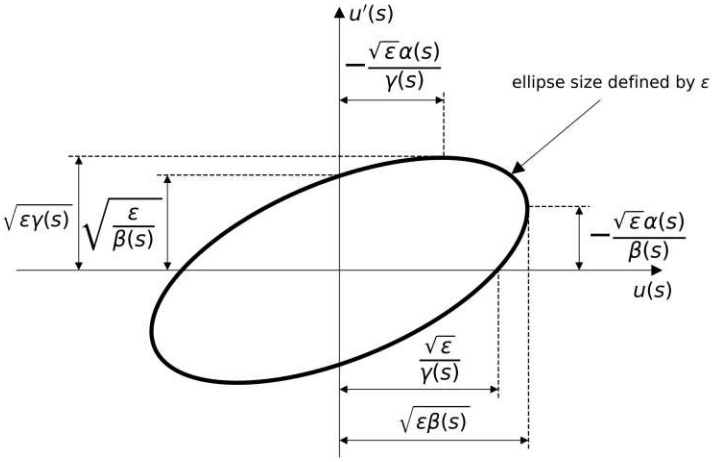

Fig. 2.3: Illustration of single particle emittance and Twiss functions. The Twiss functions define the local orientation and the emittance the size of the ellipse in phase space u, u'. Inspired by Fig. 11 in [10].

By applying some transformations this can be rewritten in the following form.

$$\alpha(s)u(s) + \beta(s)u'(s) = \sqrt{\epsilon\beta(s)}\sin\left(\mu(s) + \phi\right) \tag{2.32}$$

Squaring and summing over this equation as well as using the trigonometric relation $\cos^2(a) + \sin^2(a) = 1$ and the definition $\gamma(s) = \frac{1+\alpha(s)^2}{\beta(s)}$ yields

$$\gamma(s)u(s)^2 + 2\alpha(s)u(s)u'(s) + \beta(s)u'(s)^2 = \epsilon. \tag{2.33}$$

Equation (2.33) describes an ellipse in phase space with constant area ϵ. Its shape is determined by the so-called Twiss or Courant-Snyder functions $\alpha(s)$, $\beta(s)$ and $\gamma(s)$ (see Fig. 2.3). The area of the ellipse is given by $A = \pi\epsilon$. A particle in a closed beam lattice can only occupy configurations on this phase space ellipse. The phase advance $\mu(s)$ can be interpreted as the "distance" the particle has moved along this phase space ellipse when it passes the ideal beam path position defined by s. By considering multiple turns within a periodic beam lattice, it is apparent that for rational tunes the particle will only cover a discrete number of points along the ellipse, whereas for irrational tunes the particle occupies a new point on the ellipse after each turn. A more detailed discussion can be found in [11] on which this section is based.

2.2 Statistical Treatment of Linear Beam Dynamics

As already mentioned in the introduction of this chapter, it is not feasible to treat each particle separately with the formalisms developed in the previous section. Therefore, a statistical treatment of the particle motion is desirable, which allows for the characterization of the beam properties via easily comprehensible quantities. In the following section, the ion beam will be considered as an ensemble of N individual charged particles that are moving along the beam lattice with a certain position and velocity distribution.

2.2.1 Phase Space and Liouville's Theorem

The equations of motion for a classical point-like particle are of second order. Therefore, there are six degrees of freedom in the solution. These six degrees of freedom are determined by the three components of the initial particle position and the three components of the initial particle momentum. Then, particle motion can be characterized by a trajectory in the six-dimensional canonical phase space $(\boldsymbol{r}, \boldsymbol{p})$. For an ensemble of N particles the phase space is $6N$-dimensional. Conventionally, the components of the phase space are chosen as the canonical variables of the particles, i.e. the position and momentum. However, as the longitudinal momentum usually is substantially larger than the transverse components $p_s \gg p_x, p_y$, the following paraxial approximation holds.

$$x' = \tan(\varphi_x) \approx \varphi_x, \quad y' = \tan(\varphi_y) \approx \varphi_y \quad \Rightarrow \quad \begin{cases} p_x = p_s \tan(\varphi_x) \approx p_s \varphi_x \\ p_y = p_s \tan(\varphi_y) \approx p_s \varphi_y \end{cases} \tag{2.34}$$

By applying these approximations the geometrical phase space can be defined by the transverse components x and y, their derivatives x' and y' as well as the longitudinal position s and its momentum p_s. The geometrical phase space can be understood as the space of particle position x, y and particle velocity angle with respect to the longitudinal axis $\varphi_{x,y}(s)$. It is equivalent to the canonical phase space within the paraxial approximation defined in Eq. (2.34). This can be easily made plausible as within the paraxial approximation $p_{x,y}$ is directly proportional to $\varphi_{x,y}$ and thus the transformation from canoncial to geometrical phase space only consists of rescaling the momenta axis.

Within the branch of statistical physics, Liouville's theorem is fundamental and therefore essential to the considerations of a charged particle ensemble. The latter states that the occupied volume of a system in canonical phase space is a conserved, if only conservative forces are acting on the system. For uncoupled subspaces of the canonical phase space the occupied volume is conserved individually. Therefore, as the equations of motion in Eq. (2.2) are not coupled for drift spaces, dipole and quadrupole magnets, it follows that the volume of the occupied states in the horizontal and the vertical subspace of canonical phase space is conserved individually. For solenoid magnets a coupling of the

transverse components x, y is apparent in the equations of motion Eq. (2.15). Therefore, for solenoidal fields, the occupied volumes in the horizontal and the vertical canonical phase space are not conserved individually. Only the four dimensional transverse canonical phase space volume is conserved [15].

2.2.2 Beam Emittance

The phase space volume occupied by a distribution of charged particles is an important measure for the characterization of particle beams. In the two-dimensional horizontal or vertical phase spaces the beam emittance ϵ is related to the occupied area by

$$A = \pi\epsilon. \tag{2.35}$$

For decoupled equations of motion, e.g. for lattices comprising only drift spaces, dipole and quadrupole magnets, the beam emittance is conserved for both transverse ϵ_x, ϵ_y and the longitudinal plane ϵ_z due to Liouville's theorem. The beam emittance can be quantified by fitting an ellipse to the particle distribution (see Fig. 2.4). These ellipses can be represented by their enclosed area as well as Twiss functions similarly to the discussion of the single particle emittance in section 2.1.2. Within this diploma thesis the root-mean-square (rms) emittance ϵ_{rms} is primarily used. It is calculated as the root-mean-square to the particle distribution. For a Gaussian distribution, around 40 % of the particles are enclosed within this rms emittance. For an arbitrary distribution, the Twiss functions of the rms fit are related to the moments of the distribution by

$$\begin{aligned} \langle u^2 \rangle &= \epsilon_{\mathrm{rms}}\beta \\ \langle u'^2 \rangle &= \epsilon_{\mathrm{rms}}\gamma \\ \langle uu' \rangle &= -\epsilon_{\mathrm{rms}}\alpha. \end{aligned} \tag{2.36}$$

The emittance in geometrical phase space u, u' is only conserved if the longitudinal momentum p_s is constant. This can be easily understood by considering that $u' = \frac{p_u}{p_s} \approx \varphi_u$ decreases with increasing p_s. This decrease in transverse beam emittance is referred to as adiabatic damping. An energy-independent measure of the beam size in phase space is given by the normalized emittance ϵ_{n}, which is defined as

$$\epsilon_{\mathrm{n}} = \beta\gamma\epsilon. \tag{2.37}$$

Note, that here β and γ are the relativistic parameters and not the Twiss functions. In the context of this diploma thesis, the measurement and analysis of the beam emittance will be crucial to the reproducibility measurements after the source branch (see sectio 4.5.2) and to the setup of the beam dynamics simulations in the LEBT (see section 5.1).

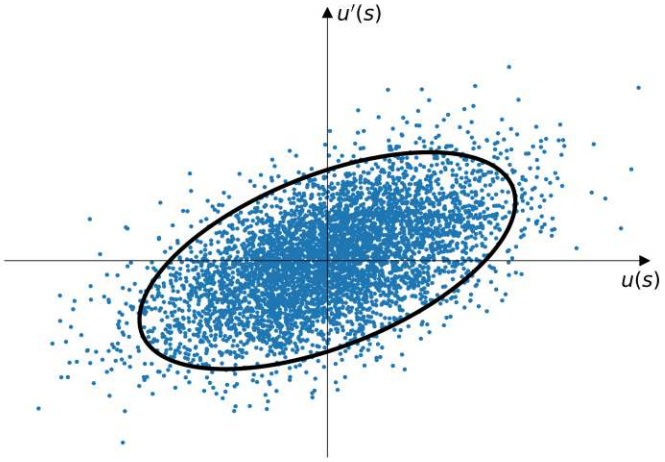

Fig. 2.4: Illustration of the Beam Emittance. The blue dots represent the particle distribution. Inspired by Fig. 13 in [10].

2.2.3 Beam Matrix

The enclosing of particle distributions within ellipses characterized by the rms emittance and the Twiss functions can be generalized to higher dimensions via the beam matrix formalism. By assuming that $\boldsymbol{u}$ is an n-dimensional phase space vector and the beam matrix $\boldsymbol{\sigma}$ is a symmetric $n \times n$ matrix, one can write the general form of the ellipse equation in n dimensions as follows.

$$\boldsymbol{u}^T \boldsymbol{\sigma}^{-1} \boldsymbol{u} = 1 \tag{2.38}$$

As discussed in section 2.1.1, matrix multiplication can be used to describe the transport of a particle beam through a lattice. This allows for a simple derivation of the beam matrix evolution behavior along the beam lattice. For this, one denotes the initial position phase space vector and beam matrix by $\boldsymbol{u}_0$, $\boldsymbol{\sigma}_0$, and the final ones by $\boldsymbol{u}_1$, $\boldsymbol{\sigma}_1$. The transfer matrix from initial to final state is given by $\boldsymbol{M}$. By requiring that both the initial and the final state have to fulfill the generalized ellipse equation in Eq. (2.38), the transformation of the beam matrix can be derived as follows.

$$\boldsymbol{u}_0^T \boldsymbol{\sigma}_0^{-1} \boldsymbol{u}_0 = \boldsymbol{u}_1^T \boldsymbol{\sigma}_1^{-1} \boldsymbol{u}_1 \stackrel{!}{=} 1$$

$$\left(\boldsymbol{M}^{-1}\boldsymbol{u}_1\right)^T \boldsymbol{\sigma}_0^{-1} \left(\boldsymbol{M}^{-1}\boldsymbol{u}_1\right) = \boldsymbol{u}_1^T \boldsymbol{\sigma}_1^{-1} \boldsymbol{u}_1 \tag{2.39}$$

$$\boldsymbol{u}_1^T (\boldsymbol{M}^{-1})^T \boldsymbol{\sigma}_0^{-1} \boldsymbol{M}^{-1} \boldsymbol{u}_1 = \boldsymbol{u}_1^T \boldsymbol{\sigma}_1^{-1} \boldsymbol{u}_1$$

A comparison of the left and the right side of this yields a relation between $\boldsymbol{\sigma}_0$ and $\boldsymbol{\sigma}_1$

$$\begin{aligned} \boldsymbol{\sigma}_1^{-1} &= (\boldsymbol{M}^{-1})^T \boldsymbol{\sigma}_0^{-1} \boldsymbol{M}^{-1} \\ \boldsymbol{\sigma}_1^{-1} &= (\boldsymbol{M}^T)^{-1} \boldsymbol{\sigma}_0^{-1} \boldsymbol{M}^{-1} \\ \boldsymbol{\sigma}_1^{-1} &= (\boldsymbol{M} \boldsymbol{\sigma}_0 \boldsymbol{M}^T)^{-1} \\ \boldsymbol{\sigma}_1 &= \boldsymbol{M} \boldsymbol{\sigma}_0 \boldsymbol{M}^T. \end{aligned} \tag{2.40}$$

Here, it was used that the inverse of a transposed matrix is equal to the transpose of the inverse of this matrix, i.e. $(\boldsymbol{A}^{-1})^T = (\boldsymbol{A}^T)^{-1}$. The transformation of the beam matrix is fairly simple, and the enclosing ellipse of a particle distribution can be easily traced through the beam lattice via matrix multiplication. Apart from this, one can also give context to the beam matrix elements. For this, it is beneficial to consider Eq. (2.38) in the two-dimensional geometrical phase space.

$$\sigma_{11} u^2 + \sigma_{12} u u' + \sigma_{21} u u' + \sigma_{22} u'^2 = 1 \tag{2.41}$$

A comparison with the emittance equation in Eq. (2.33) immediately yields the beam matrix elements

$$\boldsymbol{\sigma} = \begin{pmatrix} \sigma_{11} & \sigma_{12} \\ \sigma_{11} & \sigma_{12} \end{pmatrix} = \epsilon \begin{pmatrix} \beta & -\alpha \\ -\alpha & \gamma \end{pmatrix}. \tag{2.42}$$

A major implication of the appearance of the Twiss functions in the beam matrix is that the evolution of the Twiss functions along a beam lattice can be calculated by the transformation of the beam matrix. In terms of the statistical description of particle beams the beam matrix elements can also be correlated to the variances of the beam distribution according to Eq. (2.36).

$$\boldsymbol{\sigma} = \begin{pmatrix} \langle u_i^2 \rangle & \langle u_i u_i' \rangle \\ \langle u_i u_i' \rangle & \langle u_i'^2 \rangle \end{pmatrix} \tag{2.43}$$

By calculating the square root of the determinant, one can retrieve the rms emittance.

$$\sqrt{\det(\boldsymbol{\sigma})} = \sqrt{\langle u_i^2\rangle\langle u_i'^2\rangle - \langle u_i u_i'\rangle^2} = \epsilon_{\text{rms}} \tag{2.44}$$

A more detailed description of the concept of beam emittance and beam matrix can be found in [15] on which the previous sections are based.

Space Charge Effects

As a last part of the discussion of the statistical treatment of ion beams, the effect of space charge is discussed. A really good description of space charge effects, that goes far beyond what can be presented in this diploma thesis is given in [16] on which this section is based. Up until now, the discussion focused on the motion of particles in external fields. Additionally, internal forces between the charged particles impact the propagation of the beam. Furthermore, as the particles are moving at a certain velocity, they are also subjected to magnetic fields produced by the other moving ions. In a very simplified model a functional form of the space charge force can be derived as follows. Firstly, a cylindrical particle distribution, with radius a and constant line density λ, that moves with constant velocity $v_s = \beta_s c$ is considered. The electric and magnetic field components in cylindrical coordinates can be calculated immediately by applying Gauss' and Ampere's law.

$$\begin{aligned} E_r(r) &= \frac{\lambda}{2\pi\epsilon_0}\frac{r}{a^2} \\ B_\theta(r) &= \frac{\lambda\beta_s}{2\pi\epsilon_0 c}\frac{r}{a^2} \end{aligned} \tag{2.45}$$

The other field components are zero due to symmetry considerations. From Eq. (2.45) it is immediately evident that

$$B_\theta(r) = \frac{\beta_s}{c}E_r(r). \tag{2.46}$$

Inserting these fields into the Lorentz force yields the space charge force which is directed radially outwards.

$$F_r = q(E_r + \beta_s c B_\theta) \tag{2.47}$$

Inserting Eq. (2.46) yields

$$F_r = qE_r(1 - \beta_s^2). \tag{2.48}$$

Usually, for ion beams the paraxial approximation is valid and thus the velocity can be approximated by its component along the longitudinal axis $\beta^2 = \beta_x^2 + \beta_y^2 + \beta_s^2 \approx \beta_s^2$ (see also Eq. (2.34)). Consequently, the radial Lorentz force can be written as follows.

$$F_r = qE_r(1 - \beta^2) \tag{2.49}$$

It is evident that for low velocities the space charge force is dominated by the first term, which is a result of the Coulomb repulsion. However, for relativistic velocities, the radial force is decreasing due to an increase of the second term, which corresponds to the magnetic field component. Hence, space charge effects are especially pronounced in the low energy regime of an accelerator such as the source branch and the LEBT.

2.3 Specific Elements of the MedAustron Injector

The treatment of particle beams in terms of transverse coordinates as discussed in the previous sections is well suited to describe beam transport through lattices including dipole, quadrupole and solenoid magnets. However, the beam generation and acceleration is not yet covered by the discussions within the previous section. For this reason the basic functionality of the employed ion sources and acceleration devices at the MedAustron injector are presented in the following sections.

2.3.1 Electron Cyclotron Resonance Ion Source (ECRIS)

Electron cyclotron resonance ion sources (ECRIS) are plasma based ion sources capable of producing continuous high intensity multiply-charged ion beams that find application in numerous fields including research as well as industrial activities. Due to their stability and reliability together with low required maintenance effort, they are often the ion source of choice for synchrotron-based particle accelerator facilities.

An ECRIS produces ion beams by sustaining a stable plasma from which ions can be extracted via application of electrostatic fields. While the extraction of the ion beam from a plasma consisting of positively charged ions and electrons is very intuitive, the mechanism used to ignite and sustain the plasma is not as straight-forward. In general, plasma can be ignited by excitation of neutral gas atoms or molecules through electromagnetic waves or heating them up to a point where the atoms or molecules get ionized by thermal ionization. Even though the plasma consists of charged particles microscopically, there is a tendency to electric neutrality on macroscopic scales. This is a result of large retracting electrostatic fields arising from particle displacements within

the plasma. The quasi-neutrality is assured at length scales significantly larger than the so-called Debye length λ_D [17].

$$\lambda_\mathrm{D} = \sqrt{\frac{\epsilon_0 T_\mathrm{e}}{ne^2}} \tag{2.50}$$

Here, T_e is the electron temperature, n is the electron density and e is the electron charge. It can be shown that, within the plasma state, collective interactions dominate the binary interactions at scales larger than λ_D. The collective response to external perturbation is a key property of the plasma state. A necessary condition for the occurrence of these collective responses is given by the following expression, where $n\lambda_\mathrm{D}^3$ is the so-called plasma parameter.

$$n\lambda_\mathrm{D}^3 \gg 1 \tag{2.51}$$

Furthermore, as a result of the collective behavior, perturbations can propagate through the plasma nearly undisturbed, thus allowing for the approximation of particle dynamics within a plasma as single charged particle motion in external electromagnetic fields [17].

By treating the simplified case of an electron as free particle within a radio frequency (RF) electric field, $\boldsymbol{E} = E_0 \sin(\omega_\mathrm{rf} t)\hat{\boldsymbol{e}}_{\boldsymbol{y}}$, and a homogeneous magnetic field, $\boldsymbol{B} = B_0 \hat{\boldsymbol{e}}_{\boldsymbol{z}}$, it can be shown that the solutions to the equations of motion are given by the following expressions, provided that the exciting RF frequency ω_rf equals the cyclotron frequency $\omega_\mathbf{c} = |q|\, B_0/m$, the initial particle is initially located at the origin of the chosen cartesian coordinate system and the initial velocity is zero. A full derivation can be found in [18].

$$\begin{aligned} x(t) &\propto \cos(\omega_\mathrm{c} t) + \omega_\mathrm{c} t \sin(\omega_\mathrm{c} t) - 1 \\ y(t) &\propto \sin(\omega_\mathrm{c} t) - \omega_\mathrm{c} t \cos(\omega_\mathrm{c} t) \\ z(t) &= 0 \end{aligned} \tag{2.52}$$

From this solution it is evident that after some time the second term, which is proportional to t dominates and the radius of the particle trajectory increases steadily. With the radius also the tangential velocity $v_\mathrm{t} = \sqrt{x^2 + y^2}\omega_\mathrm{c}$ increases accordingly. Therefore, the kinetic energy of the particle is increased while absorbing energy from the RF field. As this phenomena occurs when the excitation RF frequency ω_rf is equal to the cyclotron frequency ω_c, it is called cyclotron resonance or specifically for electrons, electron cyclotron resonance (ECR). Therefore, the fundamental condition for ECR is given by

$$\omega_\mathrm{rf} = \omega_\mathrm{c}. \tag{2.53}$$

At this point it has to be noted, that the field configuration used to derive these results is highly simplified. In real ECRIS applications right-handed circularly polarized electromagnetic waves, so-called R waves, are injected into a resonant cavity where the plasma is generated. It can be shown, that with the application of R waves, ECR can also occur for non-zero initial particle velocities (see [19] for more details).

The ECR mechanism is utilized in ECR ion sources, in order to continuously provide high energy electrons to ionize atoms and molecules via impact ionization, thus sustaining a plasma inside the ECRIS. To increase the number of electrons available for ionization, it is common to introduce an electrode, the so-called DC bias electrode, into the plasma. By adapting the DC bias electrode voltage, it is possible to adjust the number of electrons introduced to the ECR plasma. Consequently, the DC bias electrode allows to optimize the ionization efficiency within the ECRIS plasma.

The confinement of the plasma within the resonance cavity in ECRIS is achieved via a magnetic field configuration that allows for longitudinal and transverse particle confinement. The longitudinal confinement is achieved via a simple magnetic mirror configuration, which consists of two coils operated with direct current flowing in the same direction. By superimposing this magnetic mirror configuration with a multipole magnet (usually a sextupole), a field configuration is achieved. In contrast to the simple magnetic mirror, this field configuration is also capable of confining the particles radially. A more detailed overview on the mechanisms of particle confinement in ECR plasmas is given in [20].

In order to properly understand the commissioning of the source branch, the three identical Pantechnik Supernanogan ECRIS [21], which are installed at the MedAustron accelerator facility, are discussed briefly. The sources are equipped with an RF generator and amplifier system, which allows for the injection of RF waves of approximately 14.5 GHz into the plasma chamber. The resonance behavior of the cavity can be fine tuned to the injected frequency. An absorbed power of up to 300 W can be achieved. In order to improve the ionization efficiency, a DC bias electrode, which is set on a voltage of a few hundred volts, is introduced into the plasma. The magnetic confinement is achieved by superposition of a sextupole and two solenoidal magnetic fields. The whole source body, consisting of the plasma chamber and the magnets, can be placed at high voltages of up to 30 kV. A puller electrode placed at a comparably low voltage of around -2 kV to -500 V is used to extract the ions from the plasma chamber and repel the electrons. After the extraction, a focus electrode allows to adapt the beam size in order to optimize the beam transport. A spectrometer magnet is used at the end of the source branch in order to select the desired ion type based on its charge-to-mass ratio (see also [22] for more details).

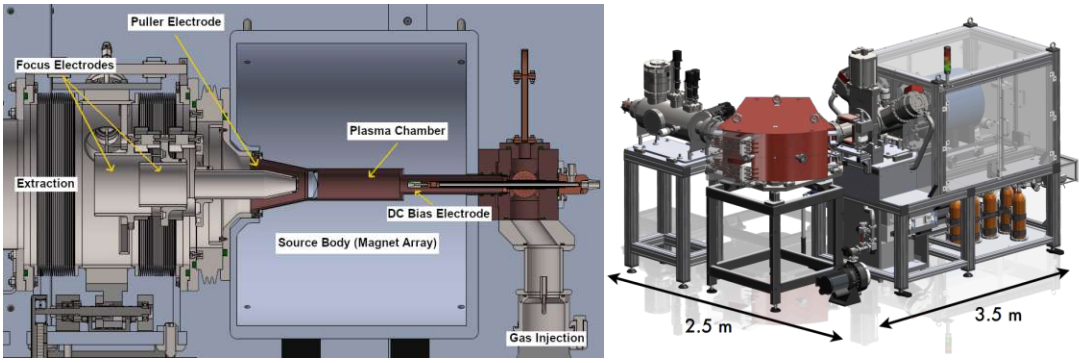

Fig. 2.5: Pantechnik Supernanogan. Cross-section of the source (left) [7] and illustration of the Pantechnik Supernanogan [21] (right).

2.3.2 Interdigital H-Mode Drift Tube LINAC (IH-DTL)

The interdigital H-mode drift tube LINAC (IH-DTL) structure is often used as primary acceleration device within injectors of ion accelerator facilities to accelerate bunched particle beams from the energy regime of several hundreds of keV/u to a few MeV/u. A drift tube LINAC (DTL) consists of a cavity in which a standing electromagnetic RF wave is oscillating[1]. Within the cavity, conducting drift tubes are installed which serve the purpose of shielding the particles if the momentary fields are not favorable for acceleration. However, if the conditions are favorable, which means there is a component of the electric field in the direction of the desired acceleration, the particles should fly through a gap in the drift tube structure, in order to be subjected to the accelerating forces. The length of the drift tubes and RF gaps depends on the particle velocity and the wavelength of the resonant standing wave. A condition for the length of the drift tubes can be derived easily by considering that the time of the shielding has to be half of the RF wave period.

$$L_n = v_n \frac{T}{2} = v_n \frac{1}{2f_{\mathrm{rf}}} = v_n \frac{\lambda_{\mathrm{rf}}}{2c} = \frac{1}{2}\beta_n \lambda_{\mathrm{rf}} \tag{2.54}$$

Here, n is the index of the drift tube, $v_n = \beta_n c$ is the particle velocity, f_{rf} is the radio frequency and λ_{rf} is the RF wavelength. From Eq. (2.54), it is evident, that the drift tubes have to get longer as the particles are accelerated in order to provide shielding during decelerating field configurations. In terms of the chosen electromagnetic mode inside the resonator cavity, intuitively, a transverse magnetic (TM) mode (see Appendix B) seems to be a good choice for the acceleration, as it exhibits longitudinal electric field components. Historically, the TM_{010} has been used in the so-called Alvarez

[1] An instructive example of cavity geometry, that can be solved analytically, is given by the so-called Pillbox cavity, which is described in Appendix B.

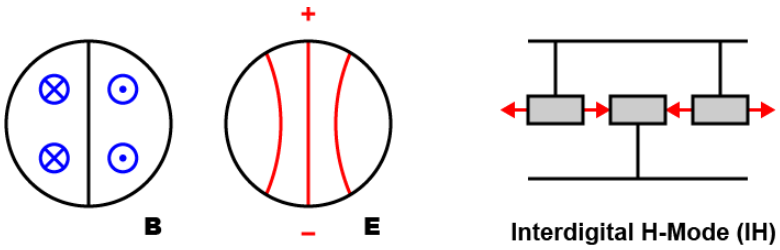

Fig. 2.6: Schematic field configuration (left) and cross-section (right) of an IH structure. IH structures make use of the TE_{110} electromagnetic mode. The magnetic field $\boldsymbol{B}$ is primarily oriented along the longitudinal axis and only has a small impact on the trajectory. The electric field $\boldsymbol{E}$ is primarily oriented along the transverse axis. However, through different grounding of the drift tubes a longitudinal electric field component is also present. Adapted from Fig. 10 in [24].

structure [23]. However, it turns out that using a transverse electric (TE) mode (see Appendix B), namely the TE_{110}, together with mounting consecutive drift tubes on opposite sides of the cavity (see Fig. 2.6) creates longitudinal electric field components that are capable of accelerating ions. The used TE_{110} mode is also called interdigital H-mode (IH) mode, which explains the name of this DTL structure [24, 25].

The phase stability in a DTL can be understood by considering the fields that particles are subjected to in the RF gaps. By design, a synchronous particle enters the acceleration field with a constant phase with respect to the RF wave ϕ_s after every drift tube. A slower particle enters the RF gap later and thus it must be subjected to a stronger field. If the latter condition is not met, the particle would be lost because of the non-favorable phase in the consecutive RF gaps. In contrast, a faster particle enters the RF gap sooner and has to be subjected to a smaller acceleration force to be transported through the structure. This can be achieved by choosing the ideal phase of the particle on the positive crest of the RF oscillation. However, when the off-momentum particles reach the ideal phase after traversing some RF gaps, they are still too slow or too fast with respect to the ideal particle motion. As a result, the real particles will oscillate around the synchronous phase. There is a boundary on how large a real particle's phase can get, i.e. how much later it can arrive at the RF gap, without being lost due to insufficient acceleration. This critical phase is given for $\phi = \phi_c = -\phi_s$ (see also Fig. 2.7). The synchronous and critical phase are fundamental parameters in the design of a DTL [25].

Longitudinal Beam Dynamics in DTL Structures

The following derivation of the longitudinal dynamics within DTL structures closely follows the one in [26]. As a first step to the mathematical description of longitudinal beam dynamics in a DTL, one has to assume a simplification that allows to neglect the complicated electric field configuration within a DTL. The assumption is that the particles

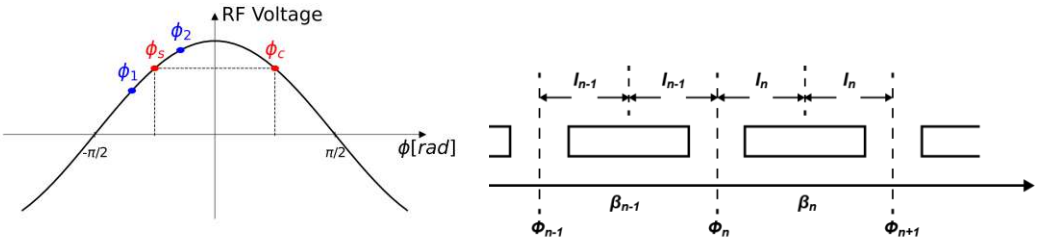

Fig. 2.7: DTL RF phase (left) and DTL cells (right). (left): The synchronous phase ϕ_s lies on the positive crest of the RF oscillation. A particle that enters the RF gap early has a smaller phase ϕ_1 and thus is subjected to a smaller field. A particle that arrives late is subjected to higher acceleration forces as long as its phase is lower than the critical phase $\phi_c = -\phi_s$. If a particle's phase exceeds ϕ_c the acceleration is lower than the one of the synchronous particle and it is lost. Inspired by Fig. 9 in [25]. (right): Decomposition of the DTL structure into single acceleration cells. Adapted from Fig. 6.2 in [26].

do not see any forces within the drift tubes and the RF gaps except for an acceleration impulse exactly at the center of each RF gap. Consequently, it is useful to introduce acceleration cells according to Fig. 2.7. Within each of these cells the particles drift with constant velocity and at the cell boundaries they receive an acceleration impulse. These boundaries will be referred to as (thin) gaps. They must not be confused with the physical RF gap between the drift tubes. However, as the thin gaps always lie within the physical RF gap, they can be referenced by the same index n. The phase changes from a gap $n-1$ to the next gap n can be written as follows.

$$\phi_n = \phi_{n-1} + \omega_{\mathrm{rf}} \frac{2l_{n-1}}{\beta_{n-1} c} \tag{2.55}$$

Here, ϕ is the RF phase, ω_{rf} is the resonant RF frequency, and β is the velocity in units of the vacuum light speed. The half cell length l is is given by

$$l_{n-1} = \frac{\beta_{s,n-1} \lambda_{\mathrm{rf}}}{2}. \tag{2.56}$$

In contrast to the discussion of transverse beam dynamics, here the subscript s indicates the synchronous particle and not the longitudinal coordinate, i.e. $\beta_{s,n-1}$ is the velocity of the synchronous particle in the cell indexed by $n-1$. With this definition, the phase change of a real particle with respect to the synchronous particle when traveling from gap $n-1$ to gap n, can be written as follows.

$$\Delta(\phi - \phi_s)_n = \Delta\phi_n - \Delta\phi_{s,n} = \frac{2\pi\beta_{s,n-1}}{\beta_{n-1}} - 2\pi = 2\pi\beta_{s,n-1}\left[\frac{1}{\beta_{n-1}} - \frac{1}{\beta_{s,n-1}}\right] \tag{2.57}$$

Here, it was used that for the synchronous particle the phase difference between two gaps is 2π. For small deviations of the real and synchronous particle velocity ($\delta\beta = \beta - \beta_s \ll 1$), the expression can be simplified by a Taylor expansion.

$$\frac{1}{\beta} - \frac{1}{\beta_s} = \frac{1}{\beta_s + \delta\beta} - \frac{1}{\beta_s} \approx -\frac{\delta\beta}{\beta_s^2} \tag{2.58}$$

By further using the relationship between the differential velocity and differential energy $\delta\beta = \delta W/(mc^2\gamma_s^3\beta_s)$, which can be derived as an approximation from the derivative $\frac{dW}{d\beta} = \frac{d}{d\beta}(m\gamma c^2)$, the difference equation for the change of phase can be written in terms of the particles energies.

$$\Delta(\phi - \phi_s)_n = -2\pi \frac{W_{n-1} - W_{s,n-1}}{mc^2\gamma_{s,n-1}^3\beta_{s,n-1}^2} \tag{2.59}$$

This difference equation links the particle energy to the RF phase in the gap. On the other hand, the energy gain of a particle within an RF gap n is given by the Panofsky equation.

$$\Delta W = qE_0TL_n\cos(\phi_n) \tag{2.60}$$

Here, q is the charge of the ions, E_0 is the average field along the center axis and L_n is the length of the RF gap. While this equation looks simple, the information of the complicated field configuration is still contained within the transit time factor T. It is a measure of the acceleration effectiveness within the RF gap and allows the comparison of the acceleration within the RF gaps to the acceleration within a DC field of the same voltage. In analogy to the considerations of the phase difference $\Delta(\phi - \phi_s)_n$, the Panofsky equation can be used to calculate the difference in energy gain of a particle with respect to the synchronous particle's energy.

$$\Delta(W - W_s)_n = \Delta W_n - \Delta W_{s,n} = qE_0TL_n(\cos(\phi_n) - \cos(\phi_{s,n})) \tag{2.61}$$

Equations (2.59) and (2.61) describe the motion in the longitudinal phase space in terms of two coupled difference equations, that can be solved numerically. However, by considering a continuous field limit, the stability of the motion can be studied via the following relations.

$$\Delta(\phi - \phi_s) \to \frac{d(\phi - \phi_s)}{dn}, \quad \Delta(W - W_s) \to \frac{d(W - W_s)}{dn} \tag{2.62}$$

Applying these limits and substituting the index n by the axial distance $s = n\beta_s\lambda_{\mathrm{rf}}$ gives the following pair of coupled differential equations.

$$\gamma_s^3\beta_s^3\frac{d(\phi-\phi_s)}{ds} = -2\pi\frac{W-W_s}{mc^2\lambda_{\mathrm{rf}}}$$
$$\frac{d(W-W_s)}{ds} = qE_0T(\cos(\phi)-\cos(\phi_s)) \tag{2.63}$$

Eliminating $W - W_s$ in these equations gives a second order differential equation.

$$\frac{d}{ds}\left[\gamma_s^3\beta_s^3\frac{d(\phi-\phi_s)}{ds}\right] = -2\pi\frac{qE_0T}{mc^2\lambda_{\mathrm{rf}}}(\cos(\phi)-\cos(\phi_s)) \tag{2.64}$$

Within the limitation of small acceleration rates, which is usually the case in DTL structures, E_0T, ϕ_s and $\beta_s\gamma_s$ can be assumed to be constant. Therefore, their derivatives with respect to s vanish. By introducing the following notation,

$$w = \delta\gamma = \frac{W-W_s}{mc^2}, \quad A = \frac{2\pi}{\beta_s^3\gamma_s^3\lambda_{\mathrm{rf}}}, \quad B = \frac{qE_0T}{mc^2}, \tag{2.65}$$

equations (2.63) and (2.64) can be simplified to

$$w' = \frac{dw}{ds} = B(\cos(\phi)-\cos(\phi_s))$$
$$\phi' = \frac{d\phi}{ds} = -Aw \tag{2.66}$$
$$\phi'' = -AB(\cos(\phi)-\cos(\phi_s)).$$

The second order differential equation in ϕ can be rewritten in terms of differentials.

$$d\phi' = -AB(\cos(\phi)-\cos(\phi_s))ds \tag{2.67}$$

Using $ds = d\phi/\phi'$ and the expression for ϕ' in Eq. (2.66), this can be expressed as

$$Awdw + B(\cos(\phi)-\cos(\phi_s))d\phi = 0. \tag{2.68}$$

Integration of this equation yields

$$\frac{Aw^2}{2} + B(\sin(\phi)-\phi\cos(\phi_s)) = H_\phi. \tag{2.69}$$

Here, H_ϕ is a constant with respect to the axial distance s. The similarities to a classical Hamiltonian allow for the identification of a kinetic and potential term in this solution. However, it has to be kept in mind that this solution is only Hamiltonian-like and does

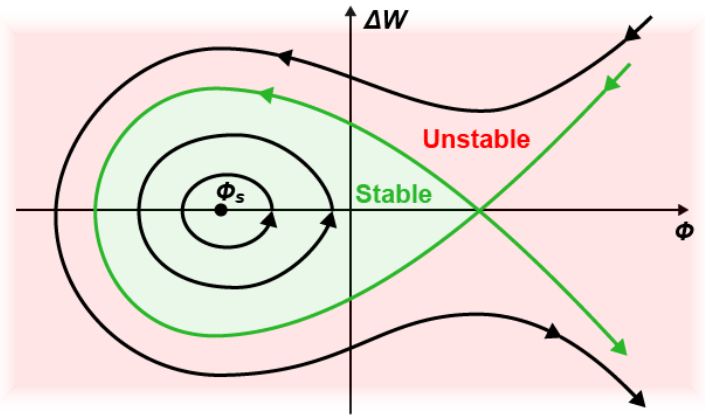

Fig. 2.8: Separatix and RF bucket. The separatix phase space trajectory defines regions of stable and unstable states of the system. The stable region within the separatix is also-called RF bucket. Adapted from Fig. 6.3 in [26].

not describe the time evolution of a system, but the evolution with respect to the axial distance s.

In analogy to classical dynamics, stability is found around minima of the potential energy (potential wells). The potential energy term is given by

$$V_\phi = B(\sin(\phi) - \phi\cos(\phi_s)). \tag{2.70}$$

It can be shown, that this potential forms a well for $-\pi \leq \phi_s \leq 0$. On the other hand, the Panovsky equation in Eq. (2.60) requires $-\pi/2 \leq \phi_s \leq \pi/2$ in order for acceleration to occur. Thus, the synchronous phase has to be negative. The stable phase region is then defined as $\phi_2 < \phi < -\phi_s$. The upper boundary is defined by the phase at which the field is smaller than for the synchronous field and the particle is consequently lost as discussed at the beginning of this section. The lower boundary can be found by solving $H_\phi(\phi_2) = H_\phi(-\phi_s)$. In analogy to the classical Hamiltonian formalism, this condition can be illustrated by considering that ϕ corresponds to the location and H_ϕ to the energy. If only conservative forces act on the system, the energy is constant and for an initial position with large enough potential energy the regions of maximum potential can be reached. The corresponding phase space trajectory is not closed. The necessary condition for this is that the initial energy is at least as large as the maximum of the potential. In terms of the discussed modified formalism within DTL structures, this corresponds to the phase ϕ being smaller than ϕ_2 defined by $H_\phi(\phi_2) = H_\phi(-\phi_s)$. The phase space trajectory that separates the stable from the unstable regions is called separatix (see also Fig. 2.8). One can find an expression for this trajectory easily by

considering that for $W = 0$, $\phi = -\phi_s$ has to be on the separatix and H_ϕ is a constant on every phase space trajectory.

$$\frac{Aw^2}{2} + B(\sin(\phi) - \phi\cos(\phi_s)) = B(\sin(-\phi_s) - \phi\cos(-\phi_s)) \tag{2.71}$$

In terms of the commissioning of helium beam, it is important to note, that the installed IH-DTL at the MedAustron facility is designed for the transport of ions with charge-to-mass ratio of 1/3, while the $^4He^{2+}$ beam has a charge-to-mass ratio of 1/2. Therefore, it is expected that the transmission efficiency will be reduced compared to the proton and carbon beams, for which the IH-DTL was designed for. It is expected that the amplitudes of the RF waves have to be considerably reduced in order to fulfill the phase requirements for the helium beam.

Transverse Dynamics in DTL Structures

Generally, the particles inside RF gaps will also experience transverse field components. The derivation of these transverse dynamics within DTL structures closely follows the discussions in [27]. It can be shown that the non-zero electromagnetic field components experienced by the particles are given by the following expressions.

$$\begin{aligned} E_s &= E_0 T J_0(Kr)\cos(\phi) \\ E_r &= -\gamma_s E_0 T J_1(Kr)\sin(\phi) \\ B_\theta &= -\frac{\gamma_s\beta_s}{c} E_0 T J_1(Kr)\sin(\phi) \end{aligned} \tag{2.72}$$

Here, $K = 2\pi/\gamma_s\beta_s\lambda_{\mathrm{rf}}$ and J_k is the k-th order spherical Bessel function. The radial Lorentz force can be written down straight-forwardly.

$$F_r = \frac{dp_r}{dt} = q(E_r - \beta c B_\theta) = -q\gamma_s(1-\beta\beta_s)J_1(Kr)E_0 T\sin(\phi) \tag{2.73}$$

The radial momentum gain within an RF gap of length L can be calculated by integration of the Lorentz force over the flight time T_L of the particle in the gap.

$$\Delta p_r = -\int_0^{T_L} q\gamma_s(1-\beta\beta_s)J_1(Kr)E_0 T\sin(\phi)dt \tag{2.74}$$

With the variable transformation $s \to \beta ct$, the integral can be written in terms of the axial distance s.

$$\begin{aligned}\Delta p_r &= -\int_0^L q\gamma_s(1-\beta\beta_s)J_1(Kr)E_0T\sin(\phi)\frac{ds}{\beta c} \\ &= -q\frac{\gamma_s(1-\beta\beta_s)}{\beta c}E_0TLJ_1(Kr)\sin(\phi)\end{aligned} \tag{2.75}$$

Under the assumption that the real particle velocities only differ slightly from the synchronous particle velocity, i.e. $\beta \approx \beta_s$ the radial momentum gain can be written as

$$\Delta p_r = -\frac{qE_0TLJ_1(Kr)\sin(\phi)}{\gamma_s\beta_s c}. \tag{2.76}$$

Furthermore, for $Kr \ll 1$, the spherical Bessel function can be approximated as $J_1(Kr) \approx Kr/2$. Therefore, one retrieves

$$\Delta p_r = -\frac{qE_0TLK\sin(\phi)}{2\gamma_s\beta_s c}. \tag{2.77}$$

As for longitudinal stability it is required that $\phi_s < 0$, it is ascertained that the phases of the accelerated real particles will be negative. This results in the transverse radial momentum to be positive, which corresponds to a defocusing force. To counteract this defocusing effect, conventionally quadrupole triplets are available within the DTL structure to refocus the beam.

Within the IH-DTL installed at the MedAustron accelerator facility, in total there are three quadrupole triplets which allow to optimize the optics. The setup of these magnets is not straight-forward, as there are no means of observing the beam properties within the IH-DTL.

2.3.3 Radio Frequency Quadruple (RFQ)

The first acceleration element after the extraction from the ion source is often chosen to be a radio frequency quadrupole (RFQ). It is necessary as acceleration with the conventional IH structure is not very efficient for small particle energies. This is due to large space charge effects as well as the impracticability of very small drift tube structures for small velocities. The common RFQ structure consists of four electrodes, which create an electric quadrupole field in the TE_{210} resonance mode. The electrode vanes exhibit sinusoidal modulations that allow the RFQ to act on the particle beam primarily in three different ways (see Fig. 2.9). Firstly, the transverse quadrupole components focus and defocus the beam similarly to magnetic quadrupoles. Due to the alternating RF voltage on the vanes, an alternate gradient structure and therefore a net beam focusing in

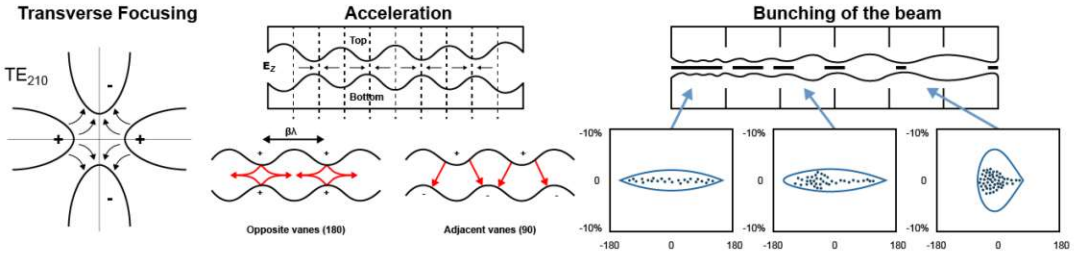

Fig. 2.9: The three working principles of the RFQ. The TE_{210} mode provides quadrupole focusing through transverse electric field components (left). Vane modulations and displacements introduce acceleration through longitudinal field components (center). An increase of the modulation period for larger energies ensures the synchronization similarly to the DTL and further bunches the beam (right). Adapted from Fig. 22 in [28].

both planes is achieved. Secondly, particle acceleration is possible through longitudinal modulation of the vanes. A longitudinal component to the electric field can be generated by placing opposite vanes at a phase difference of 180° and adjacent vanes at 90°. In order to achieve efficient acceleration, the modulation of the vanes must exhibit a periodicity of $\beta\lambda_{\mathrm{rf}}$, similarly to the IH-DTL structure. By continuously increasing the electrode vane period and amplitude, RFQ structures are also capable of bunching the beam. This is due to the change in the phase of the particles introduced by the modulated structure. Consequently, a continuous beam pulse that enters the RFQ exits as bunched beam pulse (see also [28] for a more detailed description).

Longitudinal Beam Dynamics in RFQ Structures

The longitudinal dynamics within an RFQ are conventionally described in the quasi-static approximation (see [29] for more details). This means that the Faraday induction contribution from the time dependent magnetic field is neglected and the RF field is only defined by the charges on the RFQ vane electrodes. Furthermore, even though the vane geometry changes as the particles accelerate, the mathematical description assumes the vanes to be periodic. Within the limitations posed by these approximations, a two term potential function ansatz can be used to solve the Laplace equation and thus the field configuration in the structure. A rigorous derivation of the field configuration can be found in [29]. By approximating the real RFQ vane structure by periodic cells with length $l = \beta_s\lambda_{\mathrm{rf}}/2$, which corresponds to half of the vane modulation period, consisting of thin acceleration regions and extended drift spaces similarly to the cells of the DTL, it can be shown that a similar form of the Panofsky equation is also valid for the RFQ structure.

$$\Delta W = qE_0TI_0(kr)l\cos(\phi_s) \tag{2.78}$$

The only difference to the Panofsky equation for DTL structure is the appearance of the zero order modified Bessel function $I(kr)$, with the radius r and the wave number of the vane modulation $k = 2\pi/l$. Similarly to the derivation of longitudinal dynamics in DTL structures, the Panofsky equation for RFQ structures allows to find differential equations for the energy and phase difference with respect to the synchronous particle.

$$\begin{aligned} \frac{d(W - W_s)}{ds} &= qE_0T(I_0(kr)\cos(\phi) - \cos(\phi_s)) \\ \frac{d(\phi - \phi_s)}{ds} &= -2\pi\frac{W - W_s}{mc^2\beta_s^3\lambda_{\mathrm{rf}}} \end{aligned} \tag{2.79}$$

These differential equations are considerably similar to the ones for the DTL structure. It can be shown that the stability within simple harmonic oscillations of the energy and phase differences is assured for $-\pi < \phi_s < 0$, equivalently to the stability within DTL structures. A more detailed picture of longitudinal dynamics within RFQ structures is given in [29].

In context of the helium beam commissioning, this suggests that the applied voltages have to be reduced significantly, similarly to the expectation for the IH-DTL.

Transverse Beam Dynamics in RFQ Structures

By explicitly calculating the electric fields within the RFQ structure, the non-relativistic transverse equations of motion for $u = x, y$ can be written as follows.

$$\ddot{u} + [A_{\mathrm{Q}} + A_{\mathrm{E}}\cos(ks)]u\sin(\omega_{\mathrm{rf}}t + \phi) \tag{2.80}$$

Here, A_{Q} is the quadrupole term, whereas $A_{\mathrm{E}}\cos(ks)$ accounts for the correction due to the electrode modulation with vane length $l = 2\pi/k$ which produces RF defocusing similarly to the DTL. A derivation of this equation of motion can be found in [29]. Using the synchronization condition necessary for particle acceleration $ks = \omega_{\mathrm{rf}}t$, one finds that the modulation term is proportional to

$$\cos(\omega_{\mathrm{rf}}t)\sin(\omega_{\mathrm{rf}}t + \phi) = \frac{1}{2}[\sin(\phi) + \sin(2\omega_{\mathrm{rf}}t + \phi)]. \tag{2.81}$$

The second term oscillates with twice the RF frequency and goes through one complete period during the time it takes the synchronous particle to transverse one cell of length $l = \beta_s\lambda_{\mathrm{rf}}/2$. Under the assumption that the real particle transverse momentum is small, its velocity is close to the synchronous particle's velocity and that it is only objected to acceleration forces in the thin regions at the boundaries of these cells, u can be assumed

to be constant within one cell. As a result, the term oscillating with the double RF frequency averages to zero. The equation of motion can then be written as follows.

$$\ddot{u} + \left[A_{\mathrm{Q}} \sin\left(\omega_{\mathrm{rf}} t + \phi\right) + \frac{A_{\mathrm{E}}}{2} \sin\left(\phi\right) \right] u = 0 \tag{2.82}$$

This equation is known as Mathieu's differential equation. One of its solutions is given by the following function.

$$u = \left[C_1 \sin\left(\Omega t\right) + C_2 \cos\left(\Omega t\right) \right] \left[1 + \epsilon \sin\left(\Omega t + \phi\right) \right] \tag{2.83}$$

Here, C_1 and C_2 are integration constants that are defined by the initial conditions. The first part of the solution is an oscillation with angular frequency Ω. It turns out that $\Omega \ll \omega_{\mathrm{rf}}$ and hence, the first part describes a smoothed transverse motion of the particle. The overall amplitude of this slow oscillation is modulated by the second part of the solution. It oscillates at the RF frequency and is called the flutter factor with the flutter amplitude ϵ for which generally $\epsilon \ll 1$ holds. Explicit values for Ω and ϵ can be obtained by theoretical considerations. Furthermore, it can be shown that the angular frequency of the smoothed oscillation Ω can be written as the sum of a quadrupole focusing term and an RF defocusing term. This RF defocusing term couples the transverse to the longitudinal motion.

In terms of stability, it can further be shown that the solutions to the Mathieu's differential equation in Eq. (2.83) are stable for $0 < \Omega \lambda_{\mathrm{rf}} / c < \pi$. More details about the transverse dynamics within an RFQ structure can be found in [29].

2.3.4 Beam Chopping and Bunching

As already stated, the acceleration through any DTL structure is only possible for bunched beams with bunch lengths of approximately half of the RF frequency. The injection into the synchrotron requires beam pulses of certain maximum length. However, the ion beams produced by ECRIS are continuous and have to be chopped into pulses and then bunched by the RF cavities. For the primary beam chopping an electrostatic deflector is employed. This device consists of two conducting plates that are oriented in such a way that they can deflect the ion beam. By periodically turning a voltage on and off, the beam can be chopped into pulses of around 30-50 µs. Due to the bunching characteristics of the RFQ, the macropulse is bunched into microbunches suitable for the acceleration by the IH-DTL. With an RF frequency of around 216 MHz, the bunch length is around 2 nanoseconds. In order to mitigate the loss of particles with initial phases outside the stable RF bucket region of the IH-DTL, a standing wave cavity, the so-called Buncher, is employed. It uses transverse electric fields to accelerate particles with larger phase and decelerates particles with smaller phase. As a result, after a specific drift distance, the initially slower ions will have caught up, whereas the

initially faster ones will have decreased their phase and the overall phase spread of the macropulse is minimal. By putting the IH-DTL at this position, the capture efficiency and thus the transport through the IH-DTL can be improved. Moreover, as the narrower phase interval of a bunched beam allows for the use of an ideal particle phase closer to the amplitude of the electric field, a Buncher enhances the acceleration efficiency and thus enables to build smaller acceleration structures. This design is called Combined Zero-Degree Structure (*german* Kombinierte Null Grad Struktur - KONUS) [30] and is used at the MedAustron accelerator facility.

3 Commissioning Tools

This chapter serves as a brief introduction to the relevant commissioning tools that are available for the MedAustron injector commissioning. It includes a description of the available beam diagnostics instrumentation as well as some measurement procedures that allow the characterization of the ion beam. Lastly, two beam dynamics simulation software packages used at the MedAustron are presented briefly.

3.1 Beam Dignostics (BD) Instrumentation

Within the MedAustron injector the following beam diagnostics (BD) devices allow for quantitative measurement and analysis of the ion beam parameters and are therefore crucial for the commissioning process.

Faraday Cup
The conceptually easiest way to measure beam intensity is the usage of a so-called Faraday cup. A Faraday cup consists of a conducting cup, usually made of copper, which is brought into the beam path to capture the ions. Especially, in low energy regimes the stopping range of the ions is sufficiently small for the beam to be fully absorbed within the cup. The resulting current on the cup can then be measured. Due to secondary electron emission from the Faraday cup, the measured current on the Faraday cup is increased and does not correspond to the beam current. Proper beam current measurements can be achieved by applying a voltage to the cup, which inhibits the loss of these secondary electrons [31]. At the MedAustron injector Faraday cups are operated at 1 kHz, which corresponds to a time resolution of approximately 1 ms. Due to the coarse resolution, Faraday cups are primarily employed to measure the intensity of non-pulsed beams, as for example in the source branches and the LEBT. Higher resolution Faraday cups are available after the IH-tank. However, they were not used for the helium commissioning efforts, as within the beam lattice sections of pulsed beams, there were other means of measuring the beam intensity, such as the beam current transformer, which is discussed in the following.

Beam Current Transformer

A non-invasive device to measure the beam intensity of pulsed beams is the beam current transformer. It consists of a ferromagnetic torus that is wound with a conducting wire. This wire serves as secondary winding to the ion beam and allows to transform the beam current into a measurement voltage in the secondary winding. The mathematical description is given by the formula of induced voltage as follows.

$$U_{\mathrm{meas}} = L\frac{dI_{\mathrm{b}}}{dt} \tag{3.1}$$

Here, L is the inductance of the secondary winding, I_{b} the beam current and U_{meas} the measured voltage. However, due to the dependence on the derivative, an integrator circuit has to be used in order to obtain the beam current. Usually, the torus is mounted in between non-conducting ceramic gaps in order to decouple the device from the metallic beam pipe. Additionally, the device is installed within a metal housing that ensures shielding from external electromagnetic fields [31]. Compared to the Faraday cups, the beam current transformers employed at the MedAustron injector feature a higher resolution of around 1 µs. This is enough to resolve the beam pulse. However, the microbunching structure, which features a periodicity of a few nanoseconds, cannot be measured with the current transformer.

Slit

In ion beam transport lattices slits can be used to select a specific spatial region of a beam. A conventional slit device consists of two pairs of plates, which can be moved into the beam line. One pair can move horizontally and thus generate a horizontal gap of variable size and position. The second pair moves vertically and generates a vertical gap. By superimposing the horizontal and vertical gaps, a rectangular gap can be produced. For low energies, the stopping power of the plates is large enough to completely absorb the particles and only the part of the beam within the gap can traverse the device. Slits are essential in the slit-grid procedure of emittance measurements.

Wire Scanner

A wire scanner consists of a single conducting wire that is moved through the beam pipe. When the beam impacts on the wire, secondary electrons are emitted, which can be measured as current. By plotting the measured current versus the wire position one obtains the beam profile. Conventionally, two consecutive wire scanners are installed in beam lattice structures. The first wire scanner measures the profile in the horizontal and the second one measures the profile in the vertical plane. As the velocity of the wire motion through the beam pipe is slow, wire scanners are primarily used for continuous beams [31].

Profile Grid Monitor
Similar to the wire scanner, the profile grid monitor (also referred to as secondary emission monitor, SEM Grid) uses secondary electron emission to determine the beam profile. However, instead of one wire moving through the beam a profile grid monitor consists of multiple wires oriented into a grid. The current on each wire can be read out independently and thus the whole beam profile can be taken simultaneously. In contrast to the wire scanner, the profile grid monitor can easily be applied for profile measurements of pulsed beams too [31].

Phase Probe Detector
Phase probe detectors allow to resolve the beam bunch structure non-invasively by measuring the current which is induced on a capacitive pickup electrode. A beam bunch passing a pickup generates an image current which can be measured by an external circuit. It can be shown that the image current changes its sign once the beam pulse passes the center of the capacitive pickup. Therefore, the measurement of a single beam is a sine like signal. Consequently, for a beam pulse consisting of many bunches the measurement resembles an oscillation. The periodicity of these oscillations allows to identify the bunch length, while the functional form permits to draw conclusions about the bunch structure. Even though the phase probe detector exhibits some similarities with the inductive beam current transformer, it allows for much more resolved measurements, due to the capacitive instead of inductive coupling [32].

3.2 Combined Measurements

Certain beam characteristics cannot be acquired by single device measurements. A full characterization of the beam often requires a combination of multiple measurements. In the following section, the combined measurements relevant to this diploma thesis are discussed briefly.

Time of Flight (TOF) measurement
Time of flight (TOF) measurements allow to obtain the energy of bunches by measuring the same bunch at two different phase probe detectors. Knowing the distance between the phase probe detectors as well as the time it takes the bunch to traverse this distance, allows to calculate the velocity of the bunch.

$$v = \frac{\Delta x}{\Delta t} \tag{3.2}$$

If the velocity v is known, the kinetic energy E_{kin} of the particles can be determined easily [33].

$$E_{\text{kin}} = E - E_0 = m_0\gamma c^2 - m_0 c^2 = \frac{m_0 c^2}{\sqrt{1 - \left(\frac{v}{c}\right)^2}} - m_0 c^2 \tag{3.3}$$

Here, m_0 is the rest mass of the ions and c the speed of light. Note that γ is the relativistic parameter and not the Twiss function. While this procedure is fairly simple, the identification of the same bunch on multiple phase probes complicates the situation. Within the prior setup employed at the MedAustron injector, the same bunch had to be manually identified on the first and second phase probe. Of course, this poses some significant margins for errors, as the identification of beam bunches via the human eye is not objective. In an effort to improve the whole underlying RF system, a new setup was developed, which allows to identify the bunches relative to the master oscillation of the LINAC [34]. The coupling to the master oscillator allows to identify bunches on the first and second phase probe automatically and thus ensures a correct measurement of the TOF and thus the beam energy.

Source Spectrum Measurement

Measuring the source spectrum is fundamental for identifying the constituents of an ion beam. The different ion contributions are measured selectively by scanning over spectrometer dipole magnet strengths while simultaneously measuring the beam intensity on a Faraday cup downstream. As the spectrometer magnet only transports ions within a certain range of charge-to-mass ratios, the measured beam intensity on the Faraday cup indicates the relative amount of specific ion species within the beam. Limitations of the source spectrum measurement arise when different ion types within the beam have very similar or equal charge-over-mass ratios. In this case, they appear as one peak in the spectrum. Source spectrum measurements are essential for the characterization of the source performance and the beam purity.

Low Energy Beam Emittance Measurement (Slit-Grid Method)

There are multiple ways to measure the beam emittance (see section 2.2.2 for more details). Commonly, within the low energy regime of ion beams, the so-called slit-grid method is used. A gap is produced by a slit device at a certain position. The portion of the beam that is transported through the gap is then measured on a profile grid or a wire scanner. The profile measurement allows to determine the angular distribution of the selected position interval. Therefore, this measurement setup enables the mapping of a small part of the phase space defined by the gap position and the angles corresponding to the measured beam profile. By moving the gap position over the whole beam line, it is possible to map the whole transverse phase space and retrieve the beam emittance. Even though it would be possible to measure the four-dimensional phase space with this procedure by using horizontal and vertical slits and profile monitors, conventionally the planes are measured separately. Emittance measurements are a crucial tool for the

commissioning process of any particle accelerator. In the context of the helium commissioning at the MedAustron accelerator facility, the emittance measurements served as a tool to characterize the source setpoint as well as its stability. Furthermore, the analysis of the emittance measurements after the source branch allowed for the application of beam dynamics simulations.

3.3 Measurement Analysis

The measurement data can be analyzed by a dedicated analysis framework called Python Algorithms Coded for Measurement data ANalysis (PACMAN) [35]. It allows for quick insight into the data and was extensively used during the commissioning activities presented in this diploma thesis. Apart from the analysis of single measurements, PACMAN also enables the convenient analysis of multi-measurement data, including emittance measurements [36, 37], TOF measurements [38] and the analysis of the beam trajectory on multiple beam profile monitors.

3.4 Beam Dynamics Simulations

The ion beam commissioning process is usually heavily supported by beam dynamics simulations that build upon the beam dynamics considerations of which the most basic ones were presented in section 2. At the MedAustron injector primarily the Methodical Accelerator Design-X (MAD-X) software package [39] by CERN is used to simulate the ion beam. However, within the low energy regime of the source branch, LEBT and LINAC the Trace3D software by the Los Alamos National Laboratory [40] turns out to be more suited, and thus was chosen as the main simulation tool for the helium commissioning process. In the following, both codes are presented briefly.

Methodical Accelerator Design-X (MAD-X)
Methodical Accelerator Design-X (MAD-X) is a software package aimed to support beam optics design in beam transfer lines and storage rings. It considers single-particle motion (see also sections 2.1.1 and 2.1.2) and allows for script-based simulation of beam lattice transport. Embedded into the MAD-X framework, the Polymorphic Tracking Code (PTC) [41] allows for efficient tracking of a large number of single particles through a beam lattice. Consequently, it is possible to generate a particle distribution from a beam emittance measurement (also non-Gaussian beam emittances) and track it through a beam lattice. However, the MAD-X framework does not support space charge effects. At the MedAustron accelerator facility a Python-based interface called pyMADX is used, which allows for more intuitive simulation scripts. Due to its lack of space charge considerations, MAD-X has not been used within this thesis and is only mentioned for completeness.

Trace3D
Trace3D is an interactive beam dynamics simulation software that provides tracking of Gaussian beam envelopes. These envelopes can be interpreted as beam emittance for which Trace3D allows the consideration space charge forces (see also section 2.2). The consideration of space charge is built upon the results provided by Sacherer [42]. One downside of the Trace3D framework is that it does not support automation of the simulation workflow. Within this diploma thesis Trace3D is used to simulate an initial machine setpoint for the commissioning of the LEBT, which serves as a starting point for beam-based optimizations. Furthermore, it is employed in the commissioning at the small beam pipe aperture at the position of the stripping foil after the IH-tank.

4 Source Branch Commissioning

As a first step in the commissioning process the third available ion source (S3) had to be put in operational state and commissioned to produce a continuous $^4He^{2+}$ beam. At the time of the writing there are no specific requirements to the source performance for potential future clinical applications. Consequently, the target intensity was chosen to be around 600-700 µA, which is in agreement with the commissioned intensity at HIT. In this chapter, the commissioning process up to the diagnostics tanks directly downstream of the spectrometer magnet (Fig. 4.1: S3-01-000-BDT, S3-01-001-BDT) shall be discussed. This does not only include the conventional beam commissioning but also the necessary hardware commissioning to bring the source branch into an operational state.

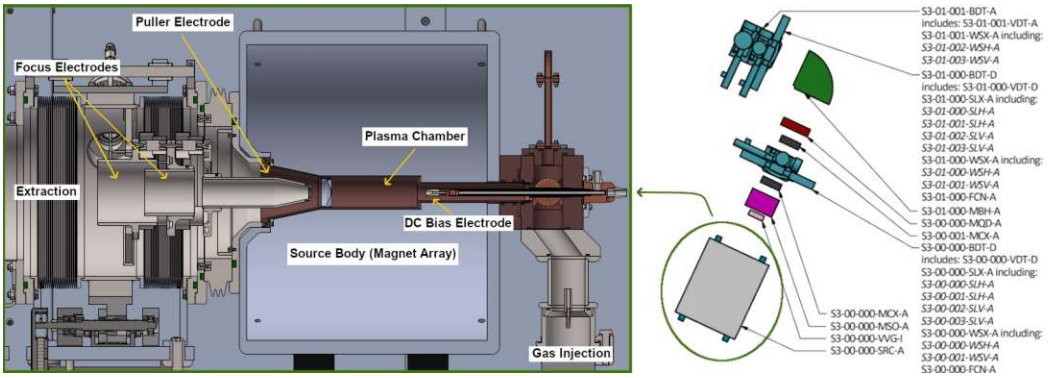

Fig. 4.1: S3 branch elements. Cross-section of source [21] (see section 2.3.1 for more details, left) and source branch layout (right) [7].

4.1 Source Hardware Commissioning

The third ion source installed at MedAustron (S3) was produced by Pantechnik in 2012 and was initially tested at the MedAustron test stand at CERN. As S3 was not required for clinical treatment, it was only used as a test stand with no specific requirements for the beam generation after its transportation to the MedAustron accelerator complex in Wiener Neustadt. It was not until end of 2019 that the hardware commissioning

was resumed as a first step of the Helium beam project. Due to the initiative of the Manufacturer Therapy Accelerator (MTA) department of EBG MedAustron GmbH, the source branch could be brought to an operational state in January 2021. The involvement of the author to the hardware commissioning was limited and thus is not within the scope of this thesis. However, a brief overview of the hardware commissioning steps will be given in order to emphasize its importance to the overall commissioning process. The hardware commissioning at the MedAustron accelerator facility is separated into four distinct phases which are labeled alphabetically.

Phase A

The first hardware commissioning phase is the installation of the corresponding devices. In principle Phase A of S3 branch was completed when the respective components were installed at the MedAustron facility in 2013. However, over the years components of the S3 branch have been used as spare parts for the clinically used source branches and thus, when the hardware commissioning resumed in 2019 some components were missing, malfunctioning or damaged. Therefore, several hardware issues had to be resolved to bring the source into a full operational state again. Among these the most relevant were:

- a leak on the spectrometer vacuum chamber
- a leak inside the cooling unit of the puller electrode

The damaged spectrometer vacuum chamber was sent in to be fixed by the source manufacturer Pantechnik and reinstalled after return. The leak on the puller electrode cooling unit resulted in the cooling fluid evaporating into the vacuum system and consequent high pressures of around 10^{-6} mbar within the extraction system of the source. For nominal operation this pressure should be around 10^{-7} mbar. The puller cooling tubes were exchanged and the pressure immediately returned to nominal values.

Phase B

After the installation, the local commissioning is performed as Phase B. This includes the functional verification of the single components as well as the establishment of the communication between the devices. During Phase B tests it was found that the current set on the spectrometer magnet drops by around 0.2 A in regular intervals of approximately one second before returning to its set value. The reason for this behavior could be identified within the locking mechanism that prevents access to the high voltage parts of the source during operation. Proper grounding reduced the fluctuations to 0.05 A, which is sufficient to guarantee consistent deflection by the spectrometer magnet and thus reproducible beam positions. Nevertheless, especially for the purpose of clinical treatment, these fluctuations should be investigated further in the future.

Phase C
Within Phase C the remote commissioning of the single components is executed. It includes assuring that the connection to the Front End Controllers (FECs) and the software integration of the devices is working properly. While the integration of the FECs worked seamlessly, the communication of the devices with the MedAustron Control System (MACS) frequently caused problems, even during the beam commissioning itself. This was due to the parallel usage of the MTA test system, by different projects and the accompanying frequent changes in the software configuration.

Phase D
Phase D consists of checking the remote operation of the devices with ion beam. As no ion beam was commissioned on S3, the remote commissioning with ion beam (Phase D) goes hand in hand with the first setup and measurements for the initial beam transport described in the next sections.

4.2 Initial Beam Transport

The figure of merit for the source commissioning is the extracted $^4He^{2+}$ intensity as well as the stability on the first Faraday cup after the spectrometer magnet (Fig. 4.1: S3-01-000-MBH, S3-01-000-FCN). Moreover, the emittance of the extracted beam is crucial, as the transmission through the LINAC structures requires comparably low emittances (see [43] for more details). As a first step, the source as well as the source branch magnets had to be set up to transport the beam. This initial setpoint then was subjected to various beam-based optimizations.

Concerning the ECR ion source parameters, the already commissioned setpoint for clinical hydrogen operation on S1 served as a starting point for the helium commissioning. Due to the fact that both hydrogen and helium are light elements with comparable ionization energies, this approach promised an initial beam of sufficient intensity to perform beam-based optimizations. The only major differences from the hydrogen setpoint can be found in the acceleration voltage of the source, which had to be adapted from 24 kV to 16 kV in order to accelerate the $^4He^{2+}$ beam to 8 keV/u after extraction. Furthermore, the injected RF power had to be increased in order to account for the difference in ionization energies. For the initial transport an RF power of 30 W was chosen. Lastly, the gas injection flow, which is a crucial parameter for a stable and sustained plasma generation, had to be adapted in order to reach a suitable injection pressure of around $2.6 \cdot 10^{-5}$ mbar. This corresponds to a gas flow of 60 % on the respective mass flow controller (MFC).

Due to the lack of beam instrumentation at the source extraction as well as the interference of $^4He^{1+}$ and $^4He^{2+}$, reliable beam dynamics simulations could not be performed in this section of the accelerator. Consequently, the initial beam transport had to be

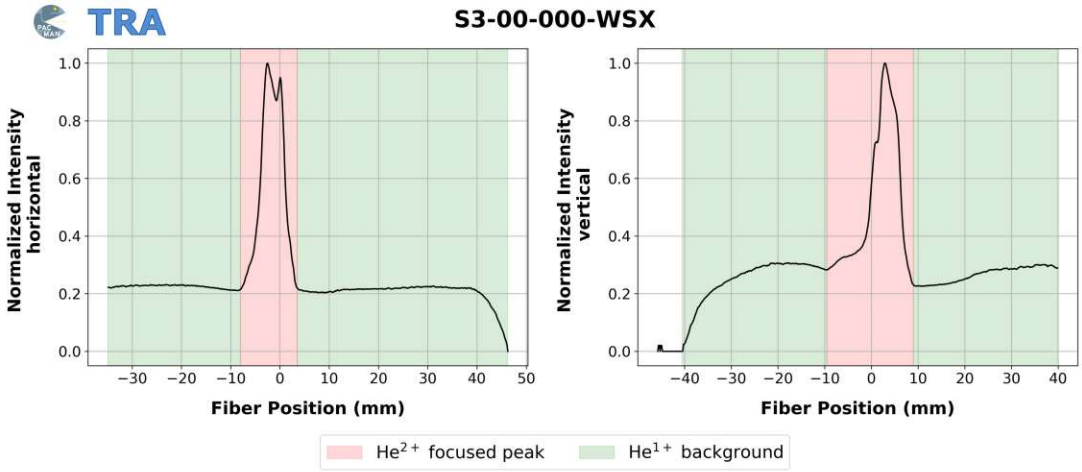

Fig. 4.2: Focused $^4He^{2+}$ beam on first diagnostics tank after the source extraction (S3-00-000-BDT, S3-00-000-WSX). The assumed focused $^4He^{2+}$ beam is colored in red while the less focused $^4He^{1+}$ forms the background in green.

achieved via beam-based optimizations. Firstly, the source focus voltage and solenoid magnet strengths directly after the extraction system (Fig. 4.1: S3-00-000-MSO) were scanned, while monitoring the beam intensity and profiles on the respective devices in the first diagnostics tank (Fig. 4.1: S3-00-000-BDT, S3-00-000-FCN, S3-00-000-WSX). The aim of this scan was to find a preliminary setup that focuses the $^4He^{2+}$ beam on the diagnostics tank. Figures of merit for this optimization were the corresponding profile measurements in which the larger focusing effect of the solenoid on the higher charged $^4He^{2+}$ can be seen in comparison to the very broad profiles of $^4He^{1+}$ (see Fig. 4.2)[1].

Subsequently, the focused beam on the first diagnostics tank served as an initial setpoint for the beam transport to the diagnostics tank downstream of the spectrometer. For this, the spectrometer magnet had to be set up to select $^4He^{2+}$ beam. In accordance to the discussions of dipole magnets in section 2.1.1, the required magnetic field for selection of a $^4He^{2+}$ beam at an energy of 8 keV/u along a section dipole with radius $\rho \approx 43.5$ cm can be calculated as follows.

$$B = \frac{p}{q\rho} \approx 0.059\,\mathrm{T} \tag{4.1}$$

With the spectrometer set up for selection of $^4He^{2+}$, a beam intensity of approximately

[1]Note that with the available diagnostics it is not guaranteed that the implied ion identification is correct. In principle, through very large focusing forces, the $^4He^{2+}$ beam could exhibit a focal point before the diagnostics tank and thus already be defocused at the position of the profile measurement, while the $^4He^{1+}$ beam is focused well at this position. However, considering the fact that the $^4He^{2+}$ beam is well transported through the spectrometer with only reasonable optimizations to the initial setpoint, it is very unlikely that the ion identification in Fig. 4.2 is incorrect.

220 µA was recorded on the consecutive Faraday cup (Fig. 4.1: S3-01-000-FCN). However, in order to optimize the source setpoint and judge on its performance a preliminary beam commissioning of the source branch up to the second diagnostics tank was performed. This included lowering the strength of the solenoid magnet (Fig. 4.1: S3-00-000-MSO) in order to shift the focal point from the first diagnostics tank farther down the beam line as well as an initial setup of the first defocusing quadrupole magnet (Fig. 4.1: S3-00-000-MQD). These efforts ultimately resulted in a measured current of 390 µA on the Faraday cup downstream of the spectrometer magnet (S3-01-000-FCN).

4.3 Source Optimizations

As aforementioned, the initial source branch setup was achieved by taking the source setpoint from the clinical hydrogen operation of S1 with adapted extraction acceleration voltage, RF power and gas injection together with an initial setup of the solenoid and quadrupole magnet in the source branch. While this already gave a beam of around 390 µA at the Faraday cup after the spectrometer magnet, optimizations to the source setpoint allowed to drastically increase the extracted $^4He^{2+}$ current as well as to improve the overall beam stability. These optimizations include the fine tuning of the plasma generation as well as the set up of the extraction system.

4.3.1 Plasma Generation

Firstly, a parameter scan of the injected RF frequency was performed to optimize for the ionization of $^4He^{2+}$ in the ECR plasma. A well-suited excitation frequency was found at 14.468 GHz. The modification of the frequency implies that the cavity resonance has to be tuned to assure proper resonance behavior. For the Pantechnik Supernanogan [21], this can be achieved by adaptation of the RF tuner position. The RF Tuner is a so-called stab tuner. It acts like an antenna to optimize the absorption of the RF frequency and limits the reflected power from the plasma for a given injected RF frequency. A scan over the whole range of RF tuner positions resulted in an optimum of +2.5 mm.

Due to the higher first and second ionization energies of helium compared to the ionization energy of hydrogen the injected forward power had to be increased to favor the generation of $^4He^{2+}$. Within the scan of the forward power a good compromise between beam intensity and beam stability could be found at around 50 W.

Further improvements in intensity and stability were achieved by tuning the DC bias voltage to 200 V. This can be traced back to additional electrons, that are introduced into the ECR plasma by the DC bias tip, thus favoring ionization. Even though higher voltages could potentially still increase the ionization efficiency and consequently the beam intensity, a setting of 200 V was chosen as a compromise between higher beam current,

stability and lifespan of the DC bias electrode tip. The final parameter configuration for the plasma generation is summarized in Tab. 4.1.

Source Parameter	**Value**
Helium gas injection	60 % flow on mass flow controller (MFC) 2 to $3 \cdot 10^{-5}$ mbar injection pressure
RF frequency	14.468 GHz
RF amplifier gain	5
RF signal generator attenuation	-11.4 dBm 50 W forward power
RF tuner Position	+2.5 mm
DC bias voltage	200 V

Tab. 4.1: Parameter configurations of the plasma generation.

4.3.2 Extraction

The subsequent step in commissioning of the ion source is tuning the extraction system. The extraction mechanism of the Pantechnik Supernanogan [21] relies on a puller electrode, which can be put on a negative potential with respect to ground and moved closer or further away from the plasma chamber by the so-called extraction motor. When setting up the voltage and position of this puller electrode, it turned out that positions closer to the plasma chamber produce higher extracted intensities while exhibiting larger beam emittances. This behavior could be observed independently of the applied puller voltage. As smaller emittances are usually better transported through the RFQ, and space charge effects increase the emittance size within the source branch and LEBT, the puller nose position was chosen farther away from the plasma chamber compared to the initial setpoint. The corresponding machine parameter called extraction motor position was chosen to be 0 mm. Another justification for the conservative choice of the puller electrode position can be found in beam stability. Generally, the extracted beam is much more stable for larger distances between the puller electrode and the plasma chamber. This can be understood by considering that the puller electrode's electric field configuration alters the plasma meniscus shape and thus the plasma itself. The closer the puller nose approaches the plasma lens, the higher the electric influence on the plasma, creating a more pronounced and curved plasma meniscus, which in turn can cause instabilities in the ECR plasma.

When scanning the puller electrode voltage, it was found that the beam intensity as function of the puller voltage exhibits a plateau. For too low or too high puller electrode voltages the beam intensities decrease and tend to become unstable exhibiting high fluctuations in beam intensity. This plateau behavior can be made plausible as follows.

Intuitively, it is clear that a low puller voltage is not effective in repelling electrons back into the plasma chamber. Thus, it is expected that sustaining the plasma might get inefficient due to the constant loss of ionizing electrons over the puller electrode's potential barrier. On the other hand, there is an upper limit to the puller voltage, where the ionization of rest gases as well as sparking between the puller electrode and the grounded beam pipe can lead to instabilities in the extracted beam. With the set-up of the plasma generation so far, this stable region was found between approximately -300 to -800 V. In the light of possible machine drift during long-term operation, a puller electrode voltage of -500 V was chosen. The selected parameters for the beam extraction are summarized in Tab. 4.2.

Source Parameter	**Value**
Source High Voltage	16000 V
Puller Voltage	-500 V
Focus Voltage	500 V
Extraction Motor Position	0 mm

Tab. 4.2: Parameter configurations of the extraction.

4.3.3 Source Drift and Parameter Adaptation

The source is affected by a long term intensity drift (see also [43]), which can be counteracted by adjusting the source setpoint. These adaptations are commonly applied for the clinical sources at the MedAustron accelerator complex in order to compensate for such intensity drifts. However, as instrumentation is limited, the plasma state cannot be fully characterized. Therefore, there is a need for metrics which at least give good indications that a similar output beam is achieved by the optimizations. For that reason, future optimizations to the S3 helium setpoint should be executed such that the following conditions are met. Firstly, the pressure at the gas injection has to be verified to be around $2.6 \cdot 10^{-5}$ mbar. Secondly, the RF signal generator attenuation has to be chosen such that a forward power of approximately 50 W is assured. Lastly, the current flowing from the source body at 16 kV to ground, which consists of the extracted beam plus leakage current has to be around 4.2 mA. At this point, it is also important to note, that any optimization to the source parameters should be attempted only after a proper warm-up time of at least half an hour as there might be changes in the plasma state and consequently in the extracted beam during this warm-up period.

4.4 Source Branch Optimizations

With the source generating a continuous helium beam, the optical and steering elements of the S3 branch could be set up in order to optimize the intensity and position of the $^4He^{2+}$ beam after the spectrometer magnet.

4.4.1 Optics Optimizations

As already elaborated in the discussion of the initial beam transport, beam dynamics simulations in the source branch are challenging and thus the optimizations of the optical elements were executed via beam-based optimizations.

In total, there are three optical elements up until the beam diagnostic tanks after the spectrometer magnet. The source focus electrode within the extraction system of the S3 as well as the already mentioned solenoid magnet (Fig. 4.1: S3-00-000-MSO) and a defocusing quadrupole (Fig. 4.1: S3-00-000-MQD). In order to avoid the necessity of a full three-dimensional parameter scan of these elements, the optimizations were separated into a two dimensional scan of the focus electrode voltage and the solenoid magnet strength and on the basis of this optimized setpoint a two dimensional scan of the solenoid magnet and the defocusing quadrupole. Even though this procedure does not guarantee to find the setpoint of maximum intensity, it gives good results within a reasonable expenditure of time. After these optimizations, a $^4He^{2+}$ beam current of approximately 630 µA was measured at the Faraday cup after the spectrometer magnet (Fig. 4.1: S3-01-000-FCN).

4.4.2 Beam Centering after Spectrometer Magnet

During the optics optimizations it became evident that beam position correction is necessary in the source branch as the wire scanner profile measurements after the spectrometer (Fig. 4.1: S3-01-000-WSX, S3-01-001-WSX) displayed deviations of the center of gravity from the center of the beam pipe in both transverse planes.

In order to correct these beam offsets, the four corrector dipoles (Fig. 4.1: S3-00-000-MCX, S3-00-001-MCX) have been used. Firstly, the beam was centered on S3-01-000-WSX with the first two correctors (S3-00-000-MCX). However, this setpoint still displayed a large offset in beam position on S3-01-001-WSX, which is an indication for the beam exiting the spectrometer magnet with a non-zero angle. To get a parallel beam out of the spectrometer, the two remaining correctors (S3-00-001-MCX) were used to counteract the kick introduced by the correction on the first two correctors. For this S3-00-001-MCX was initially set to the inverted strengths on S3-00-000-MCX, respectively. By subsequent changes to the strengths of S3-00-001-MCX, the beam could be centered sufficiently along both wire scanners.

4.5 Final Source Branch Setpoint

The optimized settings allowed for a centered $^{4}He^{2+}$ beam with intensity of approximately 640 µA at the diagnostics tank directly after the spectrometer magnet. This current corresponds to a continuous $^{4}He^{2+}$ beam with approximately $2 \cdot 10^{15}$ particles/s.

4.5.1 Spectrum and Beam Purity

As already mentioned in section 4.1, the extraction system of S3 exhibited a vacuum leak at the puller cooling circuit, thus introducing contaminants into the source. Generally, the risk of such a vacuum leak forming during continuous source operation is very small. However, service interventions, maintenance and repair work are much more likely to introduce leaks to the system and allow for the ionization of contaminants within the plasma chamber of the ECRIS. Especially for the operation of $^{4}He^{2+}$, leaks introducing air into the source could be very problematic due to the fact that among others $^{14}N^{7+}$, $^{16}O^{8+}$, $^{12}C^{6+}$ or $^{20}Ne^{10+}$ ions could be generated. In principle, these ion species could be transported simultaneously to the $^{4}He^{2+}$ beam through the machine as the charge-to-mass ratios are almost equal. Consequently, the possibility of active contaminant monitoring solutions, which allows for immediate identification of leaks to the air within the source, should be investigated in the future. Another possible cause of contamination are residual gases from parallel research and development activities. To ensure that the commissioning process was performed with a sufficiently pure helium beam, beam purity verification was necessary.

At the time of the writing, the beam purity verification is limited to source spectrum measurements (see also section 3.2). The result can be seen in Fig. 4.3. In the measured spectrum, the $^{4}He^{1+}$ peak at around 857 G as well as the $^{4}He^{2+}$ at 590 G are clearly visible. In regions of no helium peaks there are only very slight traces of contaminants present. These contaminants can be identified as oxygen and nitrogen ions from the air as well as hydrogen from parallel activities on S3. The range of the spectrum measurement (0-2950 G) allows to detect beam constituents with charge-to-mass ratios as low as $\frac{1}{43}$. However, the range in Fig. 4.3 is reduced as above 1300 G there are no traces of contaminants. Considering that contaminants are usually introduced through leaks to the air, the cooling system or residue from parallel research activity and thus display atomic masses way smaller than 43, it can be confidently stated that the beam is sufficiently pure for the first commissioning efforts. At this point it should be noted that the spectrum measurement cannot distinguish $^{4}He^{2+}$ from $^{14}N^{7+}$ or $^{16}O^{8+}$ as the corresponding peaks overlap. However, due to the very low contamination with other nitrogen and oxygen ion charge states within the spectrum, it is unlikely that the beam is significantly contaminated. Nevertheless, in the context of potential clinical application of helium, the active monitoring of nitrogen contamination is a crucial measure to be implemented in the future.

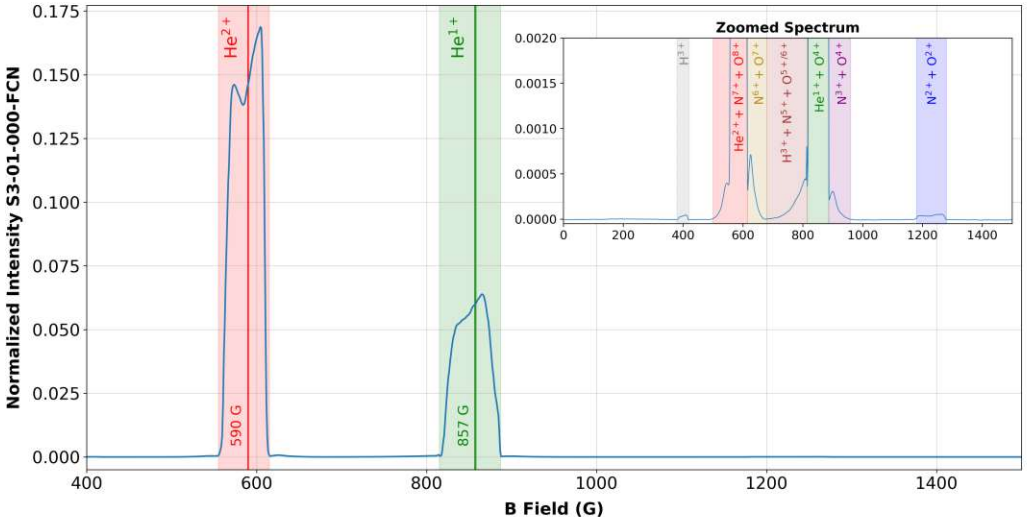

Fig. 4.3: Spectrum measurement of the extracted helium beam. The intensities are normalized to the total beam intensity, i.e. total area under the spectrum measurement curve. The zoomed spectrum measurement shows minor contaminants from unavoidable leaks to air and parallel research activity.

4.5.2 Stability and Reproducibility

Besides the beam intensity and purity, the source stability and reproducibility is of great importance for a reliable operation of the whole accelerator. It was assured that the extracted intensity is sufficiently stable over time and that the beam profiles are consistent in terms of shape and position, thus indicating reproducibility of the chosen setpoint. For a proper characterization of the reproducibility in terms of optics, multiple emittance measurements have been taken and analyzed.

Generally, an ECR ion source is considered stable if fluctuations in the extracted intensity are below a predefined threshold (usually $\pm 2.5\,\%$ for ECRIS in medical applications [43]) over several hours and the optical properties can be reproduced within this time. The measurements performed within this section were taken as part of the beam quality assurance (Beam QA) before the helium shifts. For this purpose, it was not possible to assure the stability of the extracted beam over several hours. Consequently, the beam stability and reproducibility will need to be reassessed if S3 is used in clinical operation.

Intensity Reproducibility and Stability

Before each shift dedicated to the helium commissioning, the beam intensity reproducibility was verified via measurements on the Faraday cup downstream of the spectrometer magnet (Fig. 4.1: S3-01-000-FCN). The average measurement time was around 60 seconds. In the left part of Fig. 4.4, these measurements taken over several months are summarized. The measured intensities of each individual measurement are condensed into box plots, which allows for easy comparison of the mean intensity and fluctuations. During the reproducibility tests the power supply of the high voltage that suppresses the emission of secondary electrons from the Faraday cup was damaged resulting in about 30 % increased beam current readings on S3-01-000-FCN. Thus, the measured beam intensities after the failure had to be adapted by an empirically determined factor of 0.675 and have to be interpreted carefully.

Furthermore, the source intensity was logged over several hours once to assure the stability of the source and source branch setpoint within ±2.5 % of the desired beam intensity. In the right part of Fig. 4.4 the results of this stability measurement are shown. It is apparent that within this test, the beam current does not fluctuate more than the required ±2.5 %, which corresponds to an intensity interval of approximately 625 to 655 µA.

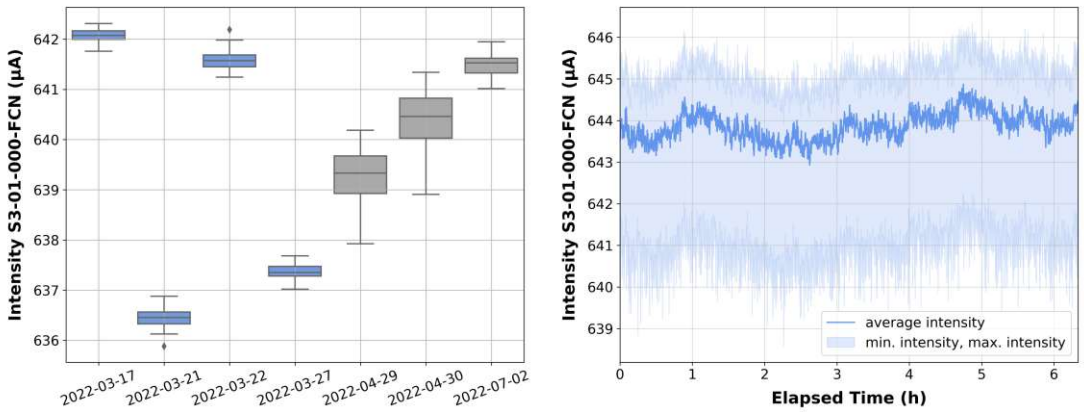

Fig. 4.4: Intensity reproducibility and stability measurements on S3-01-000-FCN. Reproducibility measurements over several months (left) and stability of the $^4He^{2+}$ beam intensity over multiple hours (right). Some intensities have been adapted by a correction factor of 0.675 due to the failure of the secondary electron repulsion on S3-01-000-FCN. The said measurements are indicated in gray.

Trajectory Reproducibility

Figure 4.5 illustrates the trajectory measurement along the source branch. It is evident that the beam profiles and steering indeed are reproducible over a larger period of time. The profiles have been normalized to the maximum measured intensity. Although reproducible profiles hint to reproducible optics, one should refrain from deriving conclusions solely based on the beam profiles as they do not convey the full optical properties of the beam.

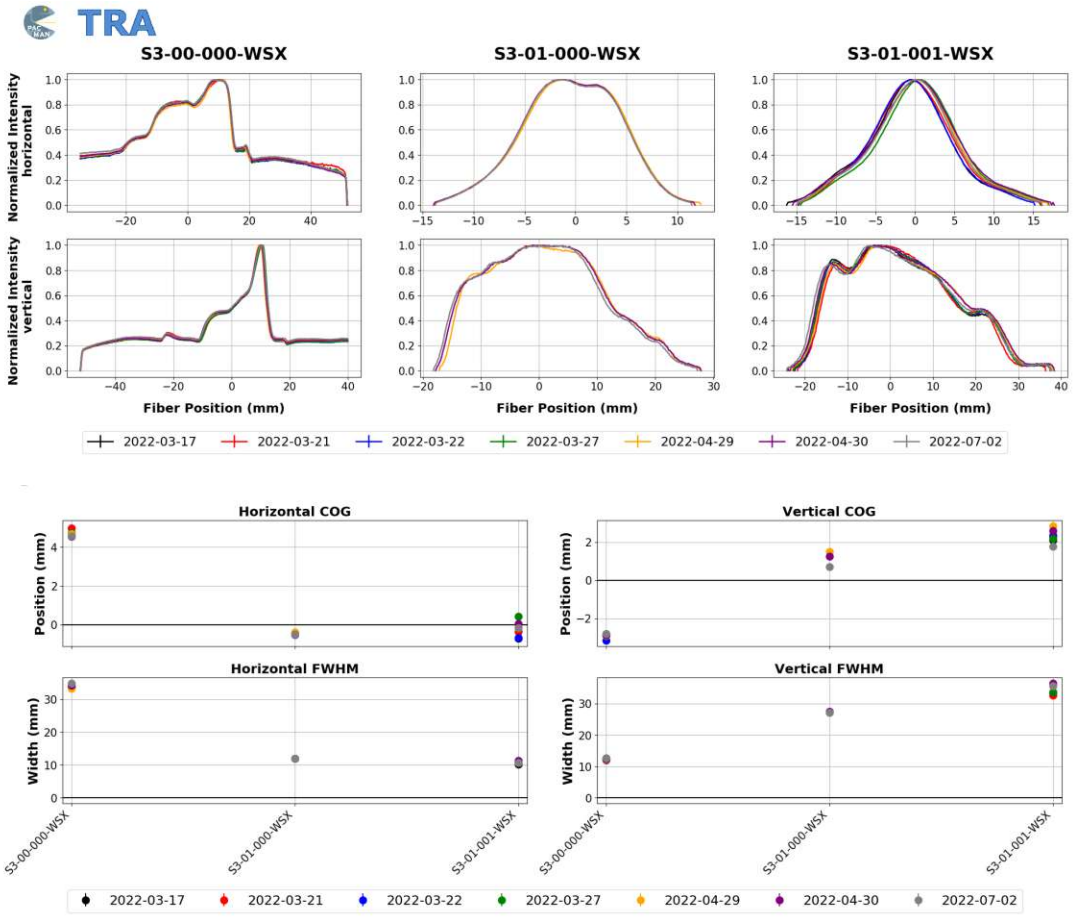

Fig. 4.5: S3 branch trajectory reproducibility measurements. Horizontal and vertical profiles normalized to the maximum intensity (top) and comparison of the center of gravity (COG) and full-width-half-maximum (FWHM) for the measured profiles (bottom). The measurements have been taken over several months. However, as S3-01-000-WSX was not operational until mid of April the beam profiles on this monitor could earliest be taken on 2022-04-29.

Emittance and Twiss Reproducibility

The (geometric) beam emittance was measured via the slit-grid method (see section 3.2) using a slit and a wire scanner downstream of the spectrometer (Fig. 4.1: S3-01-000-SLX, S3-01-001-WSX). Figure 4.6 shows emittance measurements, which have been taken over the period of several months. The analysis results have to be interpreted carefully as the analysis of the emittance measurements is inherently difficult for non-Gaussian beams. For this reason, the chosen fits of the automatic Twiss and rms emittance analysis within the PACMAN framework have been visually compared by the author in an attempt to minimize the error introduced by the analysis. Besides its role in the verification of the reproducibility, the beam emittance measurements were also used to define input parameters for the LEBT Trace3D simulations (see also section 5.1).

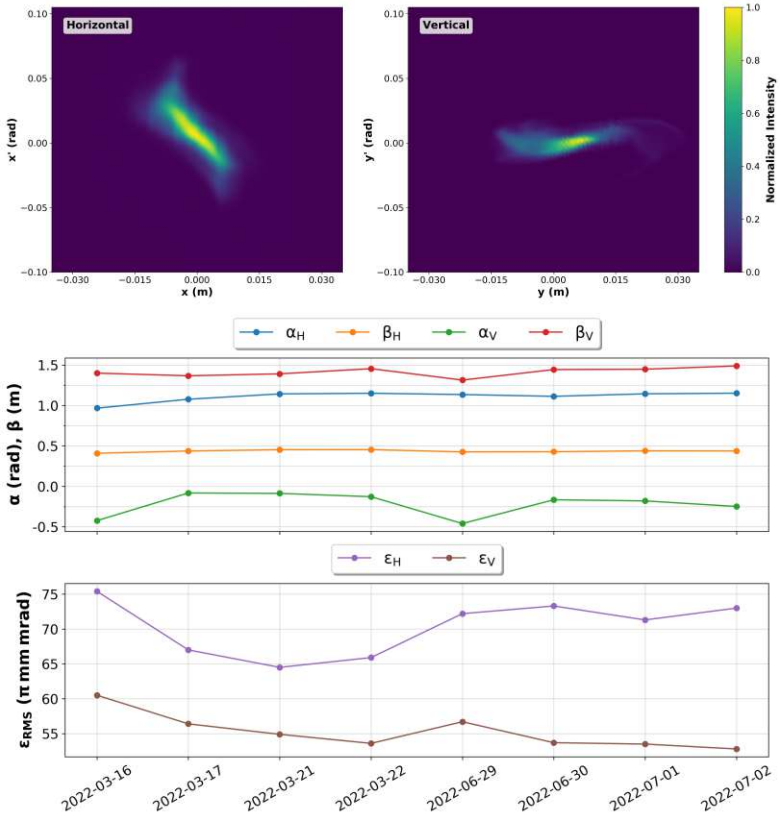

Fig. 4.6: Source branch beam emittance reproducibility measurements. Horizontal and vertical plot of the measured phase space intensities (top). Twiss parameters and rms emittance values measured at several occasions over more than three months (bottom). The measurements have been taken with the S3-01-000-SLX slit and the S3-01-001-WSX wire scanner pair.

4.6 Summary: Source Branch Commissioning

The third ion source (S3) was brought into operational state and commissioned to produce a continuous high-intensity $^4He^{2+}$ beam of around 640 µA. This was achieved by adapting the setpoint applied for clinical proton beam of S1 for the generation of $^4He^{2+}$. Initial beam transport through the source branch was achieved by scanning the optical elements as well as setting the spectrometer to select the right charge-to-mass ratio. Optimizations in the plasma generation, extraction, beam optics and steering allowed to achieve an extracted beam intensity in the desired range of 600-700 µA and center it on the wire scanners after the spectrometer magnet. The final setpoint was characterized in terms of beam intensity. Reproducibility and stability measurements were performed. A summary of the commissioning procedure is shown in Fig. 4.7.

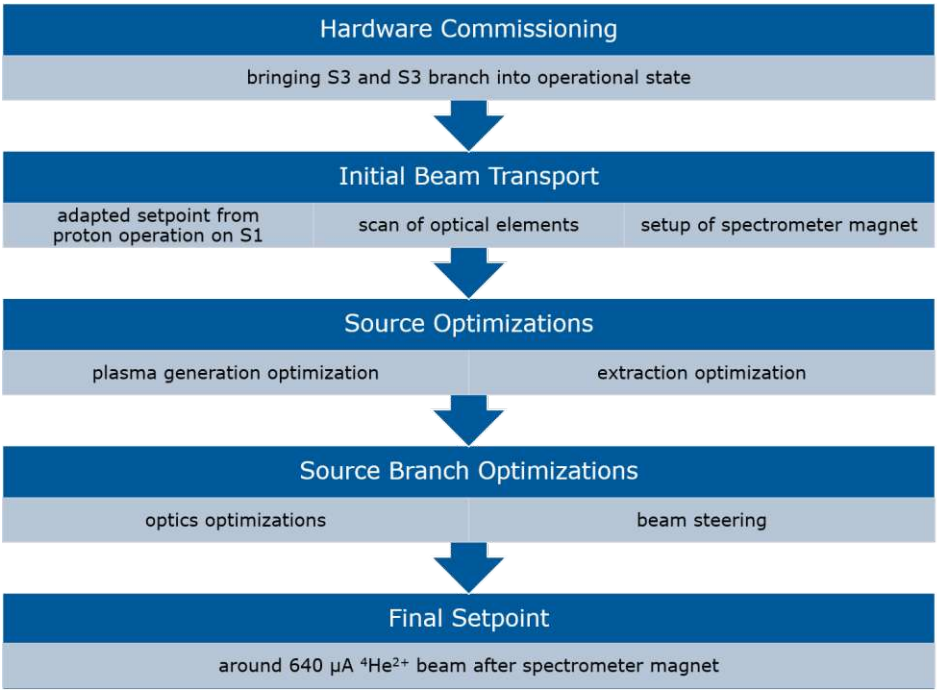

Fig. 4.7: Summarized source and source branch commissioning procedure.

5 LEBT Commissioning

With the source and source branch commissioned for extracting a reproducible and stable $^4He^{2+}$ beam, the focus could be shifted to commissioning the Low Energy Beam Transfer Line (LEBT). The LEBT commissioning process included the setup of beam dynamics simulations as well as beam steering and beam-based optimizations. The primary figure of merit for the LEBT commissioning is the transported beam intensity to the LEBT beam current transformer (Fig. 5.1: LE-01-000-CTA). However, the RFQ requires certain optical properties of the input beam for optimum acceleration and transmission. Measuring the current on to the Intertank Matching Section (IMS) beam current transformer (Fig. 6.1: LI-00-000-CTA) is crucial for assessing the performance of a selected LEBT setpoint. Lastly, the beam pulse structure as well as its stability and reproducibility are important figures of merit in the LEBT commissioning process and shall be discussed in this chapter.

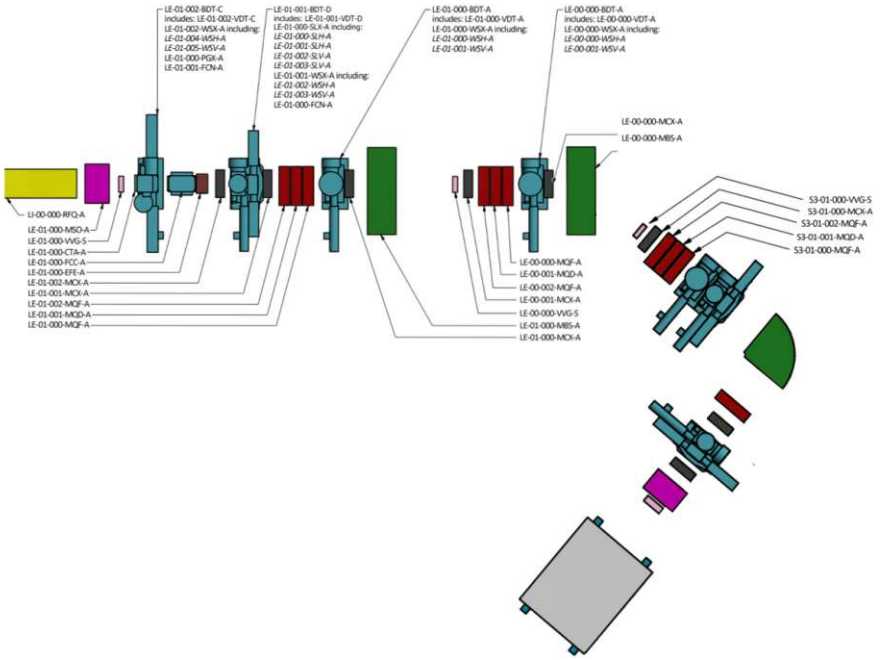

Fig. 5.1: LEBT elements (adapted from [7]).

5.1 Beam Dynamics Simulations

The initial setpoint for the LEBT optical elements, i.e. the quadrupole and solenoid magnet strengths, was found via beam dynamics simulations of the $^4He^{2+}$ beam from the position of the diagnostic tank directly downstream of the source spectrometer (Fig. 4.1: S3-01-000-BDT, S3-01-001-BDT) up to the entrance of the RFQ (Fig. 5.1: LI-00-000-RFQ). The simulations were performed using the Trace3D software by Los Alamos National Laboratory [40]. The aim of the simulation was to provide an initial setpoint that matches the optics acceptance criteria at the RFQ entrance sufficiently well, while keeping the beam envelope as small as possible to avoid losses. They are summarized in Tab. 5.1.

	α (rad)	β (m)	ϵ (π mm mrad)
Horizontal	0.5500	0.0184	180
Vertical	0.5500	0.0184	180

Tab. 5.1: RFQ entrance acceptance emittance and Twiss parameters [44].

As a first step to the setup of the beam dynamics simulation, the initial $^4He^{2+}$ beam properties had to be defined in order to match the extracted helium beam after the source spectrometer magnet. Table 5.2 summarizes the input parameters.

Parameter	**Value**
Rest Mass	3727.37938 MeV/c^2
Energy	4 u $\cdot$ 8 keV/u = 32 keV
Beam Current	0.64 mA
Frequency[1]	0.001 MHz

Tab. 5.2: Input beam parameters for Trace3D simulation of transport in the LEBT.

The initial optical properties of the simulated beam, i.e. rms emittances and Twiss parameters, have been set according to the results of the emittance reproducibility study presented in section 4.5.2. As at the time of the simulation setup only three consistent emittance measurements were available, the initial rms emittance and Twiss values were calculated as mean over these first three measurements (see Fig. 4.6: 2022-03-17 to 2022-03-22).

[1] Trace3D only supports pulsed beams and thus needs a bunching frequency as input parameter. However, a continuous beam can be simulated by setting a comparably low frequency, thus allowing one beam pulse to fill the whole beam lattice of interest at once. Calculation of the covered distance within a half period shows that the pulsing frequency is low enough to assure that there is beam simultaneously along the whole LEBT lattice.

Intrinsically, Trace3D uses an equivalent uniformly charged beam, which is simulated along the beam lattice for space charge estimation. As per the Trace3D manual [40], the equivalent uniform beam's emittance is five times the rms emittance of the distribution in order to obtain equivalent space charge forces. Considering this, the input emittance and Twiss values are chosen as follows.

	α (rad)	β (m)	ϵ_{input} (π mm mrad)
Horizontal	1.12 ± 0.07	0.45 ± 0.02	319 ± 5
Vertical	-0.10 ± 0.17	1.40 ± 0.02	275 ± 2

Tab. 5.3: Input optic parameters for Trace3D simulation of transport in the LEBT. The error is given as 1σ interval.

Matching the beam to the RFQ acceptance criteria can be performed using the in-built matching algorithm of Trace3D. The algorithm utilizes a *regula falsi* approach to optimize element parameters in order to fit the output beam Twiss parameters to the desired values in both planes. As the matching algorithm is limited to only four element parameters at a time, the matching procedure is an iterative process of matching different element parameters sequentially until a sufficient match is achieved. The graphical user interface (GUI) of the successful Trace3D simulation is illustrated in Fig. 5.2.

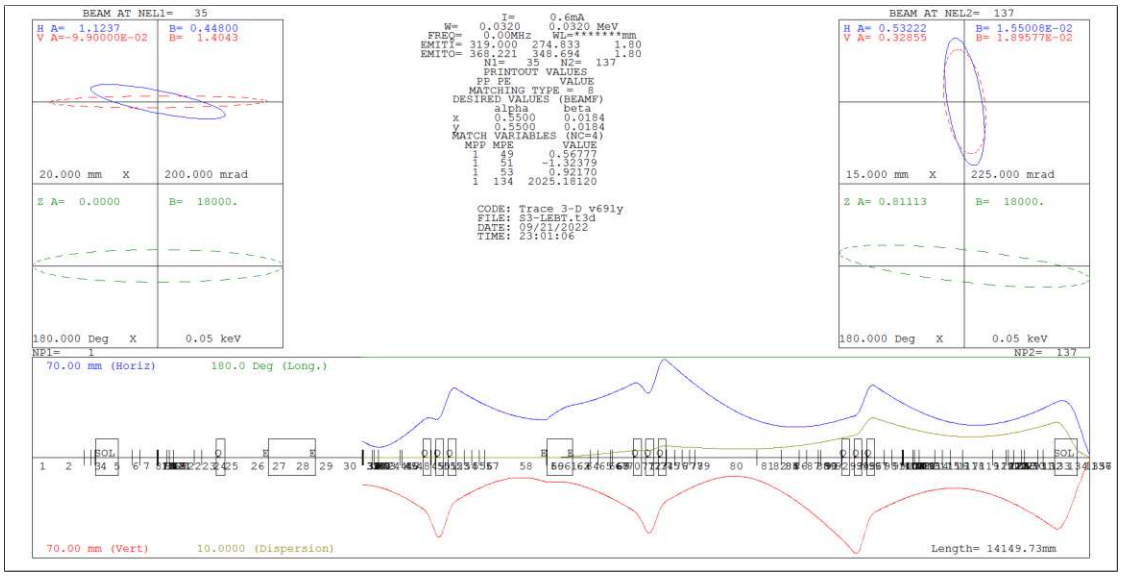

Fig. 5.2: Trace3D GUI: beam dynamics simulation of LEBT.

5.2 Initial LEBT Setpoint

The results of the beam dynamic simulations provided a first setpoint to the switching dipole (Fig. 5.1: LE-00-000-MBS-A), the LEBT quadrupole triplets (Fig. 5.1: all MQF/MQD) and the LEBT solenoid (Fig. 5.1: LE-01-000-MSO). As the Trace3D simulations do not take beam steering into account, the strengths of the corrector dipoles were not simulated and thus they were initially turned off. The electrostatic deflector (Fig. 5.1: LE-01-000-EFE) was set up in order to chop the beam into 50 µs pulses. Initial current transformer measurements at the end of the LEBT (Fig. 5.1: LE-01-000-CTA) immediately showed, that only a small fraction of the beam was transported through the LEBT. Subsequent beam trajectory measurements on the LEBT wire scanners (Fig. 5.1: all WSX) confirmed, that the beam position was significantly off-center, especially after the second switching dipole magnet (Fig. 5.1: LE-01-000-MBS), causing beam losses at aperture bottlenecks. The reason for the off-center beam position was quickly identified as the remanent magnetic field on LE-01-000-MBS, which is magnetized and subsequently turned off at the machine setup for helium operation. In order to judge on the initial setpoint extracted from the simulation, a rough steering of the beam was performed by adapting the simulated setpoint for the first switching dipole and selecting the corrector strengths such that the beam is roughly centered along the LEBT. Measurements of the LEBT current transformer yielded $^4He^{2+}$ beam currents of approximately 540 µA on LE-01-000-CTA, which corresponds to a transmission of around 84 % from source branch to LEBT. In order to transport the beam through the RFQ, the voltage of the RFQ had to be decreased due to the different charge-to-mass ratio of the $^4He^{2+}$ beam. Without extensive optimization, it was set to 2/3 of the value applied for proton and carbon beam. A proper setup of the RFQ was performed within the LINAC commissioning (see section 6.2.1). With this interim RFQ setpoint, the intensity on the current transformer in the Intertank Matching Section (IMS), LI-00-000-CTA, was found to be around 100 µA. Consequently, the RFQ transmission of the initial setpoint is approximately 18 %. This considerably low transmission hints to suboptimal injection into the RFQ. However, considering that a first transport through the LEBT was immediately achieved by applying the simulation output and rough beam steering, outlines the usefulness of beam dynamics simulations to an efficient commissioning process.

5.3 Beam Steering

As a first step to optimizing the initial LEBT setpoint, the beam was steered along the LEBT lattice. Besides mitigating losses, the importance of proper beam steering becomes evident when considering the effect of optic elements on an off-center beam. An instructive example is given by quadrupole magnets. Due to the form of transfer matrices in Eqs. (2.13) and (2.14), particles farther away from the origin of the quadrupole field, which usually coincides with the center of the beam pipe, experience larger deflections. For a particle position distribution that is sufficiently symmetrical around the center

of the beam pipe, the deflection of particles will be symmetrical too, and the center of gravity (COG) will consequently not change when traversing the magnet. However, if the position distribution is not symmetric around the center of the beam pipe, the deflection in one direction will predominate, thus effectively shifting the COG.

In terms of beam commissioning this poses a problem. Even though it is possible to transport the beam off-center, only slight changes in the setpoint of the optical elements can severely alter the beam trajectory and thus the injection efficiency into the LINAC. Therefore, to prevent future recommissioning efforts, the correct steering of the beam is an important step in the beam commissioning process. At the MedAustron accelerator facility, centering the beam in the quadrupole magnets is usually done via the so-called rapid alignment procedure (RAP). This procedure relies on scans over two corrector dipoles and a subsequent quadrupole, while measuring the COG on a beam positioning monitor downstream of the magnets. From the analyzed COG in dependence on the corrector and quadrupole strengths, a proper corrector setpoint to center the beam in the quadrupole can be determined [45]. While this procedure works well within the medium and high energy transfer lines, i.e. MEBT and HEBT line, there are some limitations which rendered its use in the LEBT line inefficient and less reliable. On the one hand, the strict separation of the non-clinically used (Fig. 5.1: S3 branch and LE-00 section) and clinically used devices prevented the application of automatic procedures, which is required for the efficient data acquisition for the RAP procedure. On the other hand, the layout of the LEBT and especially the grouping into quadrupole triplets complicates the procedure. While in principle it would be possible to only power one quadrupole of the triplet and center the beam in this magnets via RAP, it turns out that due to the low beam energies and consequent high space charge forces in the LEBT, considerable parts of the beam are most certainly lost before being detected by the beam position monitor. This greatly influences, if not prevents, the analysis of the COG via the respective PACMAN module and thus the efficient application of the RAP procedure itself.

For these reasons, it was decided to align the beam COG on the wire scanners using two corrector magnets upstream respectively, similarly to the beam centering after the source spectrometer (compare section 4.4.2). The validity of this approach was later confirmed as within the optics optimization presented in the following sections, the beam position did not change significantly. A comparison of the beam trajectory along the LEBT before and after the beam steering is shown in Fig. 5.3. In terms of transmission efficiency, the beam steering effort did neither increase the transport efficiency through the LEBT nor through the RFQ. However, the beam steering allowed to perform the beam-based optimizations to the RFQ injection presented in the following section while keeping the trajectory sufficiently centered along the beam line.

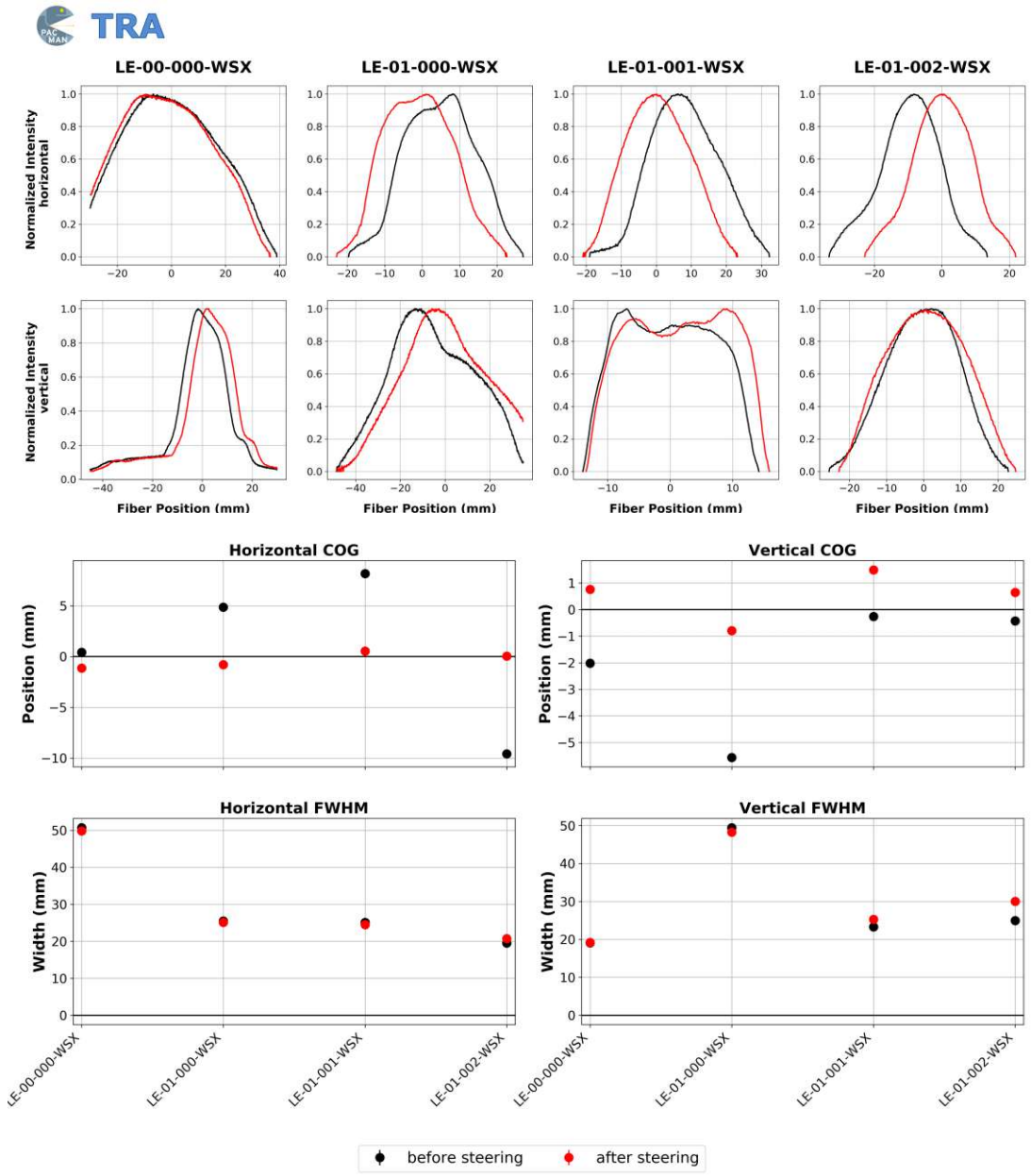

Fig. 5.3: Beam steering in LEBT. Horizontal and vertical profiles normalized to the maximum intensity (top) and comparison of the center of gravity (COG) and full-width-half-maximum (FWHM) for the measured profiles (bottom). The beam trajectory of the initial setpoint (black) still features large deviations of the COG. After the proper steering the beam is well-centered on all LEBT wire scanner profile monitors (red).

5.4 Beam-based Optimizations

Due to the lack of instrumentation at the end of the LEBT, the beam properties at the RFQ injection cannot be studied qualitatively. In contrast to the initial commissioning of proton beam at the MedAustron accelerator facility, for the helium commissioning there was no test bench available at the RFQ entrance. Consequently, the beam cannot be characterized at the RFQ entrance and any optimization to the setpoint has to be performed based on the transmission efficiency through the RFQ. These so-called beam-based optimizations allowed to optimize the transmission efficiency through the RFQ by adapting the injected beam.

For each of these scans it is important to be aware of hysteresis effects within the magnets that might alter the results. To ensure reproducibility, all the scans have been performed on the downwards slope of the hysteresis curves. During the preparation of the accelerator, the magnets were magnetized and then kept at their maximum setpoint. Consequently, the scans were performed from the highest to the lowest desired strength monotonically.

5.4.1 LEBT Stability Optimization

As a first step of the beam-based optimizations the strengths of the last LEBT quadrupole triplet (Fig. 5.1: LE-01-000-MQF, LE-01-001-MQD and LE-01-002-MQF) was scanned within -15 % to +20 % of the simulated setpoint strengths while monitoring the mean beam current on LE-01-000-CTA. Note that this scan was one-dimensional as all of the triplet's magnet strengths were altered in each iteration step. Even though with this diagonal scan of the parameter space many potential setpoints were disregarded, it allowed for a quick test of significantly different setpoints and thus for a quick judgment of the stability of the LEBT transport efficiency with changes in the optical properties of the beam. The result of the scan can be seen in Fig. 5.4. A setpoint of +5 % with respect to the simulated triplet strength was selected, as this measurement is well within the flattop region of the scan, thus indicating a certain amount of stability, while still being reasonably close to the simulated setpoint.

This procedure would also have been applicable for optimizing the other LEBT triplets. However, due to time constraints, these scans could not be performed. A justification for prioritizing the last LEBT triplet can be found by considering that a sufficiently small beam envelope size is more relevant in the end section of the LEBT due to smaller beam pipe apertures within the electrostatic deflector (Fig. 5.1: LE-01-000-EFE).

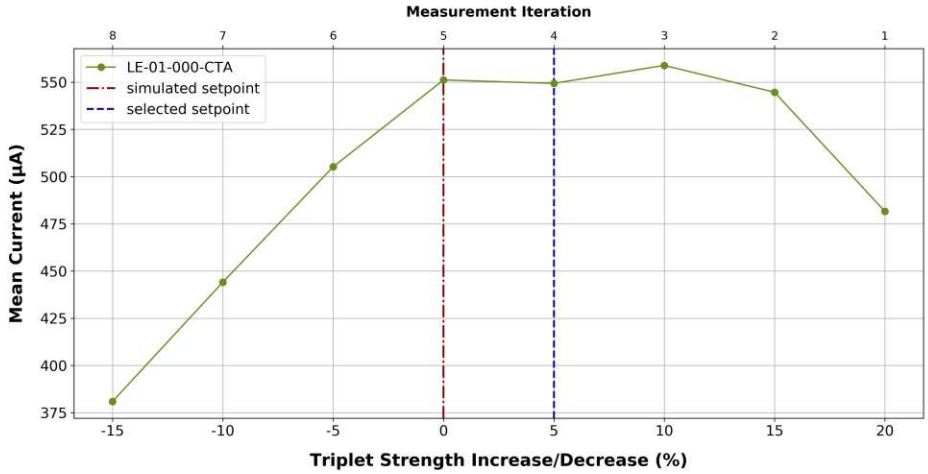

Fig. 5.4: Diagonal parameter space scan of last LEBT triplet. A setpoint of +5 % with respect to the simulated triplet strength was chosen as a compromise between stability with optical changes and proximity to the simulated setpoint.

5.4.2 RFQ Injection Optimization

The high transport efficiency through the LEBT combined with the comparably low transmission through the RFQ hints at an inefficient injection into the RFQ. This can have multiple reasons.

- The optical properties of the beam at the RFQ entrance are considerably different from the designed optics. This would manifest itself in different Twiss parameters and rms emittance size.
- The beam position at the RFQ entrance is off-center.
- The beam enters the RFQ with an angle.
- The RFQ is not set up correctly (part of LINAC commissioning, see chapter 6.2.1).

The most efficient way to act on the optics is to scan over several solenoid strengths around the simulated setpoint. This corresponds to shifting the focal point of the beam along the center axis due to the focusing properties of the solenoid magnet (see the considerations on solenoidal magnetic fields in section 2.1.1). The steering and angle can be optimized via a two-dimensional scan of the horizontal and vertical strengths of the last two correctors. Similarly, to the beam steering in the source branch and LEBT, it is expected that an optimum is found for different kick directions on the correctors, corresponding to centering the beam via the first corrector and straightening it along the center axis on the second one.

Optics Optimization via Solenoid Strength Scan

To optimize the optics at the RFQ entrance, a parameter scan of the solenoid field strength was performed around the simulated setting. The results in Fig. 5.5 show a clear maximum of the transmission for a solenoid strength of around $8.35\,\mathrm{m}^{-1}$. Compared to the simulated setpoint at a normalized field of around $7.8\,\mathrm{m}^{-1}$, the adaptation of the solenoid strength allowed for a significant increase of the transported beam current to around $340\,\mu\mathrm{A}$, which corresponds to a transmission efficiency of over $60\,\%$.

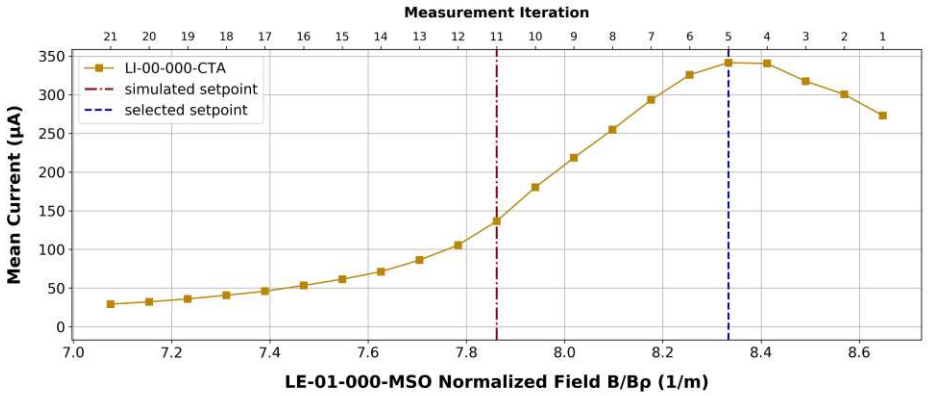

Fig. 5.5: Scan of LEBT solenoid magnet strength. Mean current on LI-00-000-CTA as a function of the solenoid strength.

Injection Optimization via Corrector Dipole Scan

The subsequent optimization step concerned the steering into the RFQ. The optimum setpoint was identified via two-dimensional scans on the last two LEBT correctors (Fig. 5.1: LE-01-001-MCX and LE-01-002-MCX), while monitoring the mean current on the current transformer after the RFQ. As the number of settings scales quadratically with the number of measurement points on each magnet, it is important to find good initial conditions and identify a small enough region to scan through. These initial conditions were given by the configuration for these magnets after the proper beam steering.

The results of the corrector scans are shown in Fig. 5.6. Overall, it is apparent that there are regions of high intensity. For the horizontal scan displayed on the left, the optimum is well resolved in the center of the scanned parameter space. The vertical scan was performed with the already optimized horizontal corrector settings and thus exhibits larger intensities. The settings for the corrector pair were chosen according to the maximum beam current, but also ensuring that the setpoint lies within a sufficiently large parameter space region of high intensity, again assuring a sufficient reliability of the setpoint against slight variation in the beam properties. As expected, the optimum strengths retrieved from this scan exhibit inverse kicks for consecutive corrector dipoles.

This is in line with the assumption that optimum transmission is reached when the first corrector is used for centering the beam, while the second one straightens it onto the beam pipe center axis.

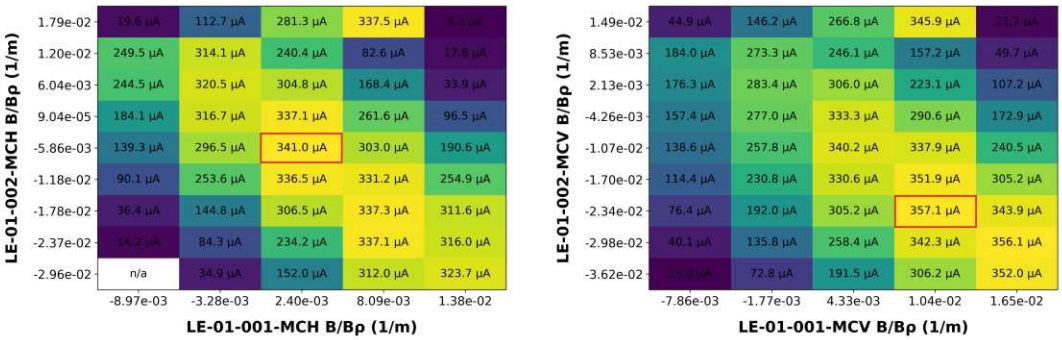

Fig. 5.6: 2D strength scan on last LEBT correctors. Horizontal (left) and vertical (right) scan of the last two corrector dipoles in the LEBT. The measured intensities are mean beam currents on LI-00-000-CTA. The selected configuration is framed in red.

5.5 Final LEBT Setpoint

The final setpoint is the result of the beam dynamic simulations, the beam steering and the applied beam-based optimizations. A transmission of approximately 89 % from source branch to LEBT was achieved, while a transmission from LEBT to the IMS of approximately 62 % was reached. Considering the longer beam lattice for S3 compared to S1 and S2 as well as the fact that the RFQ is designed for a different charge-to-mass ratio, these results are satisfactory. The beam pulse length was fixed at 50 µs. The proper setup of the pulse length can only be achieved when commissioning the injection into the synchrotron, as the injection efficiency into the synchrotron highly depends on the pulse length. A summary of the commissioning results is given in Tab. 5.4.

Monitor	Current (µA)	Part./s	Part. in Pulse	Transmission (%)
S3-01-000-FCN	640	$2 \cdot 10^{15}$	-	-
LE-01-000-CTA	570	$1.7 \cdot 10^{15}$	$8.8 \cdot 10^{10}$	89
LI-00-000-CTA	355	$1.1 \cdot 10^{15}$	$5.2 \cdot 10^{10}$	62

Tab. 5.4: Beam current and particle numbers after LEBT commissioning.

5.5.1 Beam Pulse Structure

Besides the mean beam intensities, also the beam pulse structure is a figure of merit for successful LEBT commissioning. On the LEBT current transformer, the beam pulse exhibits a pronounced flattop of constant beam current. This is due to the electrostatic deflector (LE-01-000-EFE) slicing 50 µs pulses out of the continuous beam in the LEBT. After the RFQ, the beam pulse is bunched into microbunches with 2 ns length due to the resonant RF frequency of around 216.816 MHz within the LINAC cavities (see section 2.3.3 and 2.3.4 for more details).The time resolution of the current transformer measurements is not fine enough to resolve this microbunch structure. Therefore, the figure of merit regarding the current transformer measurements is a pronounced flattop with small ripple. Nevertheless, the time resolution of the current transformer is still way finer than the one of the Faraday cup, thus allowing to resolve fluctuations in the microsecond range. In the source branch and in the LEBT, no other accelerator component than the ECR ion source is operating at frequencies high enough to introduce fluctuations in this frequency range. Therefore, the LEBT current transformer (LE-01-000-CTA) measurement is crucial for the identification of very high frequency instabilities in the source. Two representative current transformer measurements of $^{4}He^{2+}$ beam pulses are plotted in Fig. 5.7. For the selected helium setpoint these instabilities on the LEBT flattop are comparably low, which confirms the stability of the selected source setpoint on a short timescale. The beam pulse after the RFQ also exhibits a flattop, while as expected, the microbunches are not visible.

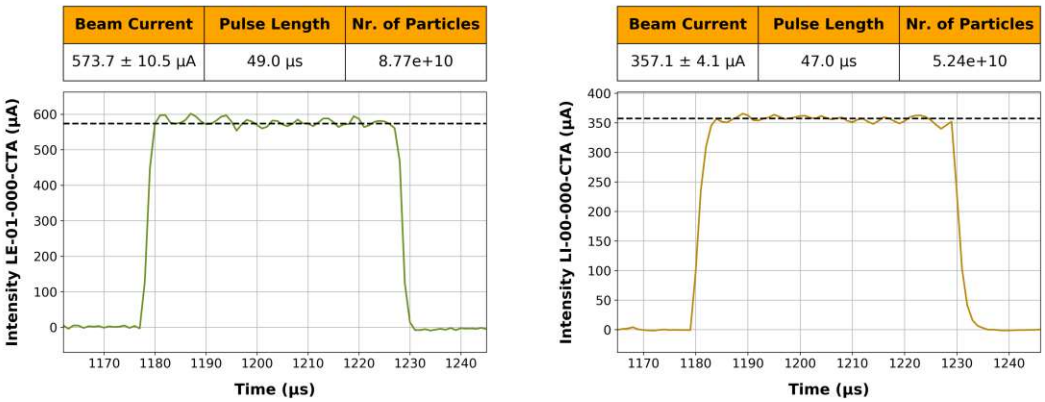

Fig. 5.7: Beam pulses on current transformers at the end of the LEBT (LE-01-000-CTA, left plot) and after the RFQ (LI-00-000-CTA, right plot). The time is given relative to respective measurement trigger command.

5.5.2 Reproducibility

Similarly to the reproducibility measurements in the source branch, the reproducibility measurements of the intensity and the trajectory were performed for the final LEBT setpoint. These measurements were performed as beam quality assurance for the dedicated helium shifts. Due to time constraints during these QA measurements, it was decided against acquiring the emittance in the LEBT as a part of the reproducibility measurements.

Intensity Reproducibility and Stability

Figure 5.8 shows the intensity stability measurements acquired on the LEBT current transformer (LE-01-000-CTA). The intensity measured on the current transformer in the IMS (LI-00-000-CTA) cannot be taken into account in the LEBT reproducibility measurements as the setup of the RFQ changed with the LINAC commissioning efforts. Similarly to the source intensity measurements in section 4.5.2, the measured intensities are condensed into box plots, in order to allow for easy comparison of the mean intensity and fluctuations. The left plot shows the long term stability over multiple months. The measurement data, from which each box plot is constructed, was taken from multiple measurements taken on the same day and therefore corresponds to multiple beam pulses. It is evident that the beam is sufficiently reproducible on LE-01-000-CTA over longer periods (see left plot of Fig. 5.8). Moreover, the stability in the short-term was investigated by sending multiple pulses after one another and measuring the current. Again the reproducibility is apparent (see right plot of Fig. 5.8).

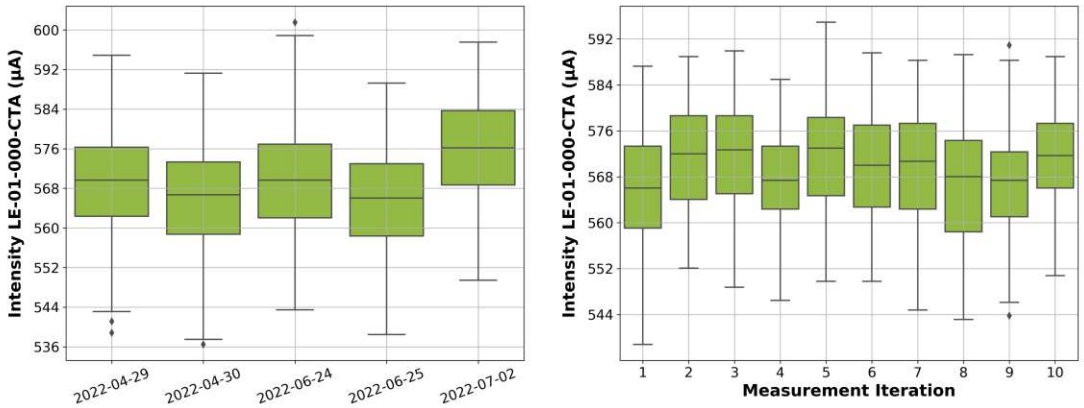

Fig. 5.8: Intensity reproducibility and stability measurements on current transformer at the end of the LEBT (LE-01-000-CTA). Reproducibility measurements taken on different occasions (left) and stability of the $^{4}He^{2+}$ beam intensity over multiple beam pulses measured immediately after one another (right).

Trajectory Reproducibility

The reproducibility of the trajectory is evaluated analogously to the one in the source branch (see 4.5.2). It is evident in Fig. 5.9, that the reproducibility is slightly worse compared to the source branch. However, this is not surprising considering that the LEBT beam lattice is much longer and small deviations from the beam path, which might not be visible in the source branch, propagate and aggravate over the course of the LEBT. Nevertheless, the steering proved to be stable enough to deliver reproducible intensities in the LEBT and the IMS, and thus is considered sufficiently reproducible.

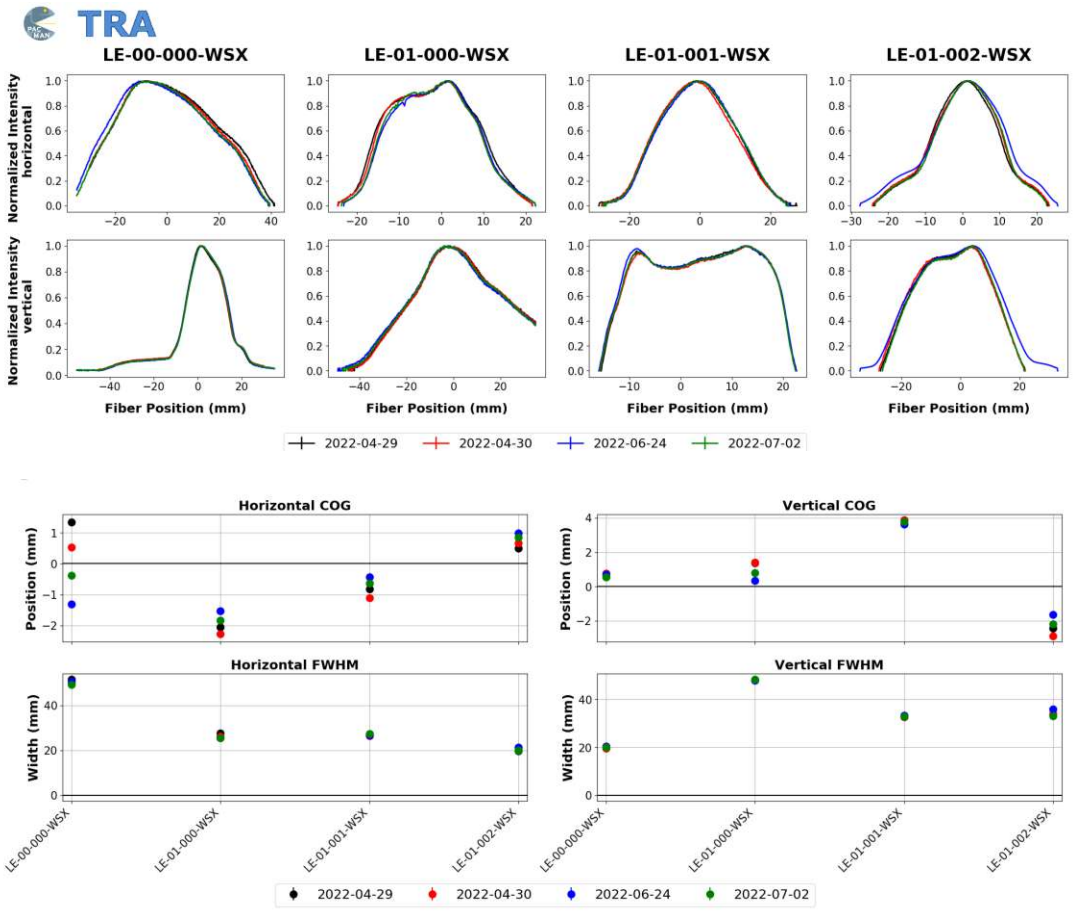

Fig. 5.9: LEBT trajectory reproducibility measurements. Horizontal and vertical profiles normalized to the maximum intensity (top). Comparison of the COG and FWHM for the measured profiles (bottom).

5.6 Summary: LEBT Commissioning

The LEBT was commissioned for the transport of $^4He^{2+}$ beam and optimum injection in to the LINAC. The application of Trace3D beam dynamics simulations as well as a rough beam steering allowed for an initial setpoint which already transports 540 µA of $^4He^{2+}$ beam to the end of the LEBT. A fine steering of the beam was performed before applying beam-based optimizations. These optimizations were on the one hand performed to verify that the transport efficiency is sufficiently resilient against slight changes of the input beam as well as to optimize the injection into the RFQ. The final setpoint was characterized in terms of intensity and beam pulse structure. Reproducibility measurements have been performed in the form of intensity measurements on current transformer and trajectory measurements on wire scanners. A summary of the LEBT commissioning procedure is shown in Fig. 5.10.

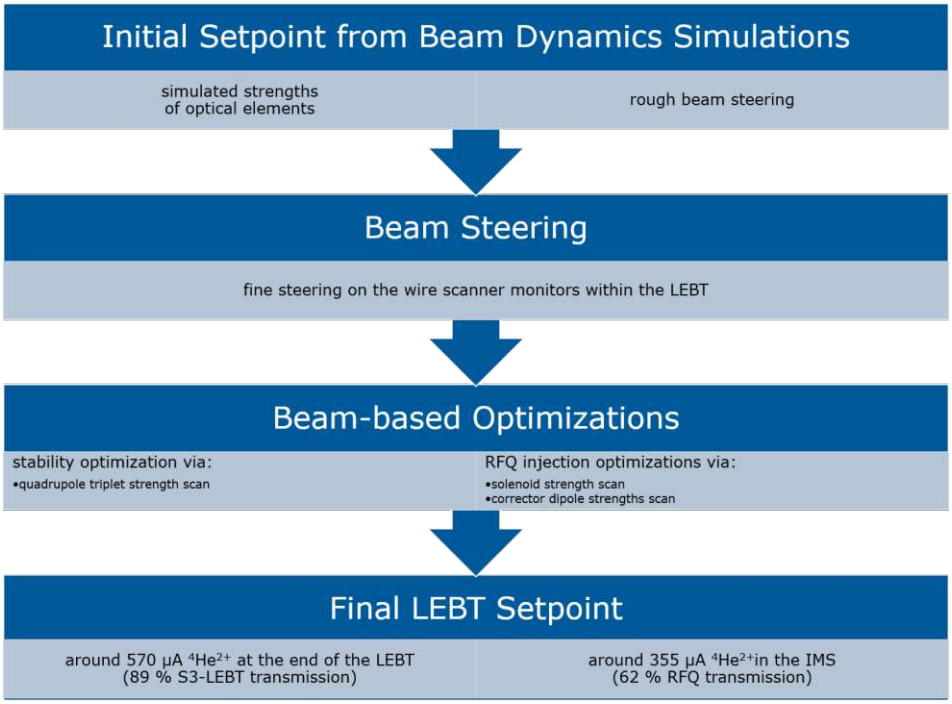

Fig. 5.10: Summarized LEBT commissioning procedure.

6 LINAC Commissioning

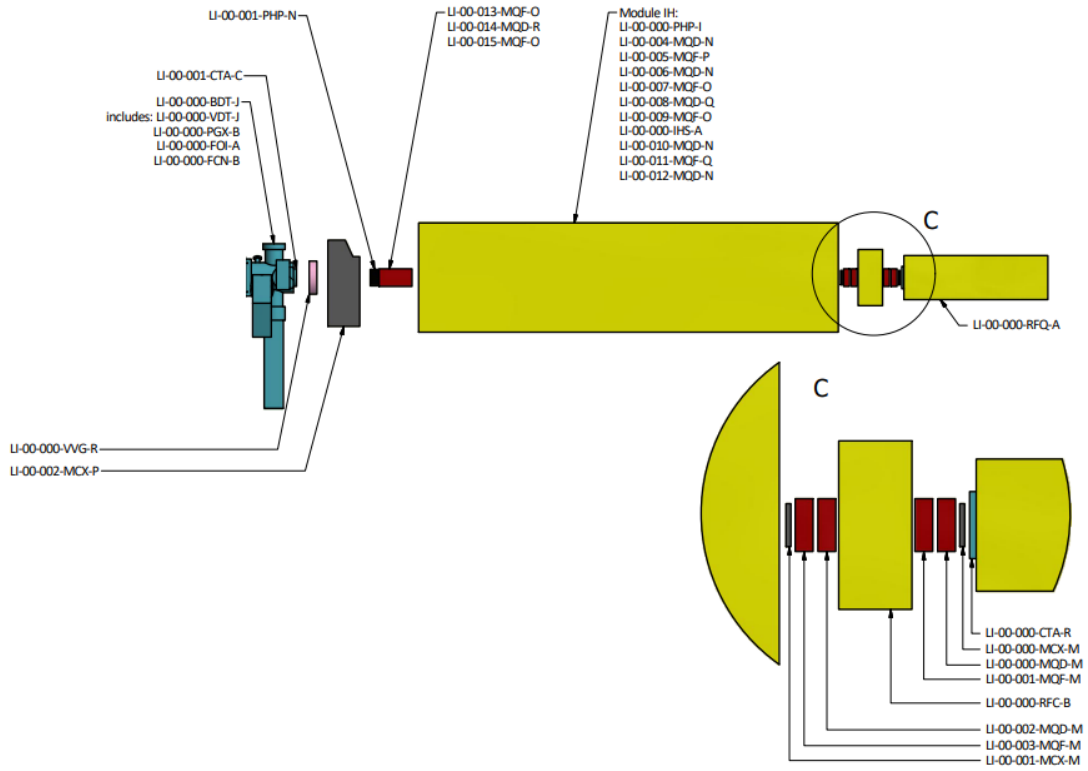

Fig. 6.1: LINAC elements with zoomed Intertank Matching Section (IMS) (adapted from [7]). A zoomed in illustration of the Intertank Matching Section (IMS) is shown (C).

This chapter summarizes the commissioning of $^4He^{2+}$ beam in the MedAustron LINAC. The LINAC commissioning process was more challenging than the source and LEBT commissioning as the cavities within the LINAC structure are designed for optimized transport and acceleration of proton and carbon ions with charge-to-mass ratio of $1/3$, while the $^4He^{2+}$ beam exhibits a charge-to-mass ratio of $1/2$. Moreover, the beam diagnostics instrumentation within the LINAC is limited. The only instrumentation available

is a current transformer within the IMS (Fig. 6.1: LI-00-000-CTA) as well as a current transformer and profile grid monitor after the IH-tank (Fig. 6.1: LI-00-001-CTA, LI-00-000-PGX). Due to this limited beam diagnostics instrumentation, the LINAC commissioning procedure heavily depends on beam-based optimizations. The figures of merit for these optimizations are the transported current as well as the beam pulse stability and energy.

6.1 Initial LINAC Setpoint

Due to the limited instrumentation and the consequent necessity of beam-based optimizations, it was crucial to find a suitable initial setpoint. This chosen setpoint had to transport a large enough beam intensity through the LINAC such that the effects of the optimizations applied afterwards could be judged unambiguously. Assuming that the beam output of the RFQ is similar for helium and proton beam, an initial setpoint could be found by rescaling the voltages on the RFQ, IH-tank and buncher cavity as well as the quadrupole magnet strengths to the charge-to-mass ratio of the $^4He^{2+}$ beam. This corresponds to a rescaling factor of $2/3$. For this initial setpoint, the corrector dipole strengths were kept at zero. As the energy and thus the velocity of the $^4He^{2+}$ beam are assumed to be close to the one for the proton beam, the phases of the buncher and IH-tank with respect to the LINAC master oscillator, were taken from the clinical proton beam operation. This initial setpoint allowed for the transport of approximately 350 µA of $^4He^{2+}$ beam into the IMS and around 20-30 µA after the IH-tank. The total transmission efficiency through the LINAC for this initial setpoint is approximately 4 %. Starting from this initial setpoint the proper longitudinal setup (RF cavity voltages and phases) and the proper transverse setup (setup of beam optics and steering elements) could be performed.

6.2 Longitudinal Setup

For the sake of an efficient commissioning process, it was assumed that the longitudinal properties of the beam are sufficiently independent from the transverse ones, thus allowing for separate optimization of the RF cavity parameters, the beam optics and the beam steering. Each RF cavity can be tuned in terms of applied voltage and phase. The RF cavity voltage can be set by the so-called amplitude parameter, while the phase of the RF wave in the cavity can be set with respect to a master oscillator. An exception is given by the RFQ, whose only parameter is the amplitude (voltage). For more details on the LINAC RF cavities see section 2.3. A theoretical consideration of the electromagnetic configuration within an easy cavity geometry is given in Appendix B.

6.2.1 RFQ Optimization

As a first step of the longitudinal optimization the amplitude (applied cavity voltage) of the RFQ was scanned. The scan was performed starting from the rescaled RFQ amplitude parameter setpoint for proton operation, which was 49.6 at the time of the writing. In order to be able to assess the direct effect of the RFQ setpoint on the transmission through the IH-tank, the buncher cavity was turned off during this scan.

The results of the RFQ amplitude (cavity voltage) scan are shown in Fig. 6.2. It turns out that the current on the current transformer in the IMS (LI-00-000-CTA) as a function of the RFQ amplitude parameter forms a plateau. The initial (rescaled) setpoint, which is around 33, does not give the best results in terms of transmission efficiency through the RFQ and IH-tank. For the subsequent commissioning, the second maximum was selected at an amplitude setpoint of around 38.25. As this setpoint is larger than the rescaled one, it is expected that the energy in the IMS will be higher than the nominal output energy of the RFQ (400 keV/u)[1]. Consequently, the phase configuration of the buncher and IH-tank is expected to be different than for proton and carbon operation, in order to compensate for the faster traversing of the $^4He^{2+}$ beam through the IMS.

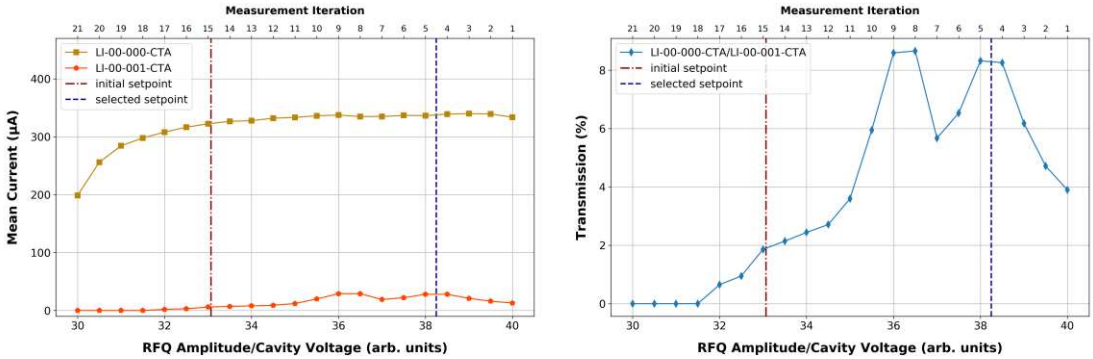

Fig. 6.2: Amplitude/cavity voltage optimization of RFQ. Beam currents on the LINAC current transformers during the amplitude scan (left) and transmission efficiency through the IH-tank (right).

6.2.2 IH-Tank Optimization

For the IH-tank phase and amplitude (applied cavity voltage) optimizations simple scans were performed around the initial setpoint, with the buncher cavity turned off. For the

[1]Note that this statement is an assumption as it is not *ad hoc* clear that the correlation between amplitude and applied RFQ voltage is linear and thus that the rescaled amplitude corresponds to the correctly rescaled voltage. However, the hypothesis of higher beam energy in the IMS is supported by the fact that the respective optimum IH-tank and buncher phases with respect to the LINAC master oscillator are smaller compared to the proton and carbon setpoint, indicating a higher velocity in the IMS.

setup of the IH-tank this is even more essential as it assures to match the output energy of the RFQ to the IH-tank phase for optimum capture efficiency, without potential energy kicks from the buncher cavity.

The respective results are illustrated in Fig. 6.3. Both scans feature a clear maximum, which was adopted as the optimum setpoint. For the IH-tank amplitude this maximum is situated at around 36. This is comparably close to the rescaled setpoint of 34.67, which was calculated from the IH-tank amplitude of 52 for proton operation at the time of the writing. The IH phase was selected at 57 degrees. As expected, the selected optimum setpoint for the phase is smaller compared to the phase applied for the proton beam, hinting at a slightly larger particle velocity in the IMS.

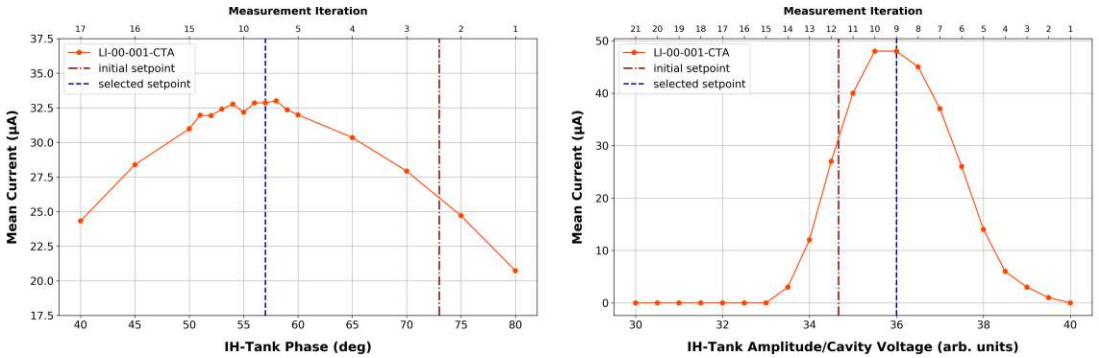

Fig. 6.3: Phase (left) and amplitude/cavity voltage (right) optimization of IH-tank. Beam currents are measured on the current transformer after the IH-tank (LI-00-001-CTA).

6.2.3 Buncher Optimization

Subsequent to optimizing the transmission through the RFQ and IH-tank, the focus was shifted to the buncher cavity setup. The RFQ output energy and the IH-tank phase are matched as a result of the optimizations described in the previous sections. It is therefore expected that the proper setup of the buncher cavity, i.e. a setup that does not introduce an energy kick, will lead to an optimum in the beam transmission through the IH-tank. In order to identify this optimum, simple scans around the initial phase and amplitude setpoints were performed, similar to the ones for the IH-tank. The results of the scans are shown in Fig. 6.4. As expected, both scans feature a pronounced maximum in transported current. Again, the optimum in phase is located at a considerably smaller value than for the initial setpoint, taken from the currently applied settings for proton beam. This again supports the hypothesis of higher velocities of $^4He^{2+}$ particles in the IMS. A setpoint of 27 of buncher amplitude and -17 degrees of buncher phase was selected, which corresponds to the setpoint of maximum transported beam current through the IH-tank.

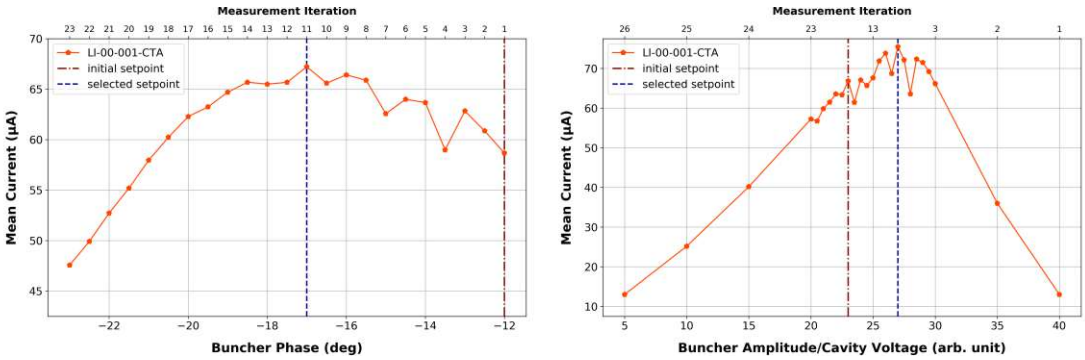

Fig. 6.4: Phase (left) and amplitude/cavity voltage (right) optimization of buncher cavity. Beam currents are measured on the current transformer after the IH-tank (LI-00-001-CTA).

6.3 Transverse Optimization

The RF cavity parameter optimization allowed to increase the transmission through the IH-Tank to over 70 µA on LI-00-000-CTA. This corresponds to a transmission of around 20 % through the IH-tank and a transmission of 12 % through the whole LINAC. As discussed in the previous sections, the results of these longitudinal optimizations suggest a slightly higher beam energy in the IMS compared to the design energy. A full simulation of the LINAC using Trace3D was attempted, but ultimately could not deliver appropriate results due to the uncertainties within the beam energy and the initial Twiss parameters. For this reason, the transverse optimization of the $^4He^{2+}$ beam in the LINAC section had to be performed again via beam-based optimization scans, similarly to the ones employed in the LEBT.

At this point some peculiarities of the LINAC magnets shall be mentioned as their operation significantly deviates from the ones in the LEBT. Firstly, due to the uncertainties in beam energy (and thus the magnetic rigidity $B\rho$) within the LINAC, it is not possible to use the normalized fields $B/B\rho$. Especially for the quadrupole triplets within the IH-tank, the description by normalized magnetic fields is problematic as the magnetic rigidity $B\rho$ changes between each quadrupole triplet depending on the beam energy. At the MedAustron accelerator facility, all LINAC magnet strengths are referenced by the applied currents. Secondly, the magnets within the LINAC section are only powered to their nominal setpoint at the time of the beam passage. In between these duty pulses they are kept idle. This results in the violation of the convention of operating the magnets on the downward-slope of the hysteresis curve, which is applied at the source branch and LEBT of the MedAustron accelerator facility. However, it turns out that this violation of the hysteresis curve only has negligible effects on the beam. Consequently, within the LINAC, the order in which the magnet strengths are scanned is not important.

6.3.1 IMS and IH-Tank Injection Optimization

The first step of the transverse optimizations is the tuning of the $^4He^{2+}$ beam injection into the IH-tank. Similarly to the RFQ, the IH-tank features optical acceptance criteria for optimum transmission. Consequently, the applied procedure is very similar to the optimization of the RFQ injection presented in section 5.4.2.

Injection Optimization via Corrector Dipole Scans

The optimization of the two available corrector dipoles in each plane within the IMS (Fig. 6.1: LI-00-000-MCX and LI-00-001-MCX) allowed to optimize the injection of the beam into the IH-tank. The procedure applied is equivalent to the one presented for the injection optimization into the RFQ (see section 5.4.2). However, as the correctors were kept off up to this point in the commissioning process, a suitable initial setup had to be found. This initial setpoint was found via single parameter scans of all the corrector dipole strengths.

The results of the two-dimensional corrector strength optimization is shown in Fig. 6.5. As expected, the optimum setpoint is found for corrector strengths of opposite sign, which hints at the first corrector dipole correcting for the beam position, while the second corrector straightening the beam along the beam pipe center-axis into the IH-tank. The new corrector setpoint in the IMS significantly improves the current transported through the IH-tank to from 70 µA to approximately 150 µA on LI-00-001-CTA, while marginally decreasing the current on the IMS current transformer from 350 µA to 340 µA on LI-00-000-CTA.

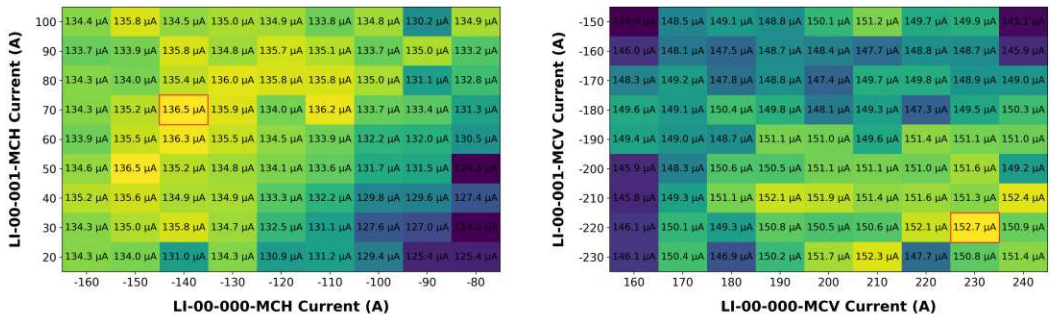

Fig. 6.5: 2D strength scan on IMS correctors. Horizontal (left) and vertical (right) scan of the available corrector dipoles. The measured intensities are mean beam currents on LI-00-001-CTA. The selected configuration is framed in red.

Optics Optimization via Quadrupole Doublet Scan

As a second step of the IMS optimization, a scan of the two available individually powered quadrupole doublets (Fig. 6.1: LI-00-000-MQD/LI-00-001-MQF and LI-00-002-MQD/LI-00-003-MQF) was performed. The basic idea was to shift the entrance of the IH-tank, i.e. effectively altering the dimensions of the IMS, within Trace3D simulations and extract a matching setpoint to the IH-tank acceptance criteria for each of these offsets. This procedure allows to quickly test various focusing configurations without having to perform the whole four-dimensional quadrupole doublet strength scan. As there are no means to measure the beam emittance within the IMS, the emittance and Twiss parameters measured during the initial commissioning of proton beam at the MedAustron facility were used as input to the simulations. Furthermore, the beam was assumed to have the nominal RFQ output energy of 400 MeV/u. Of course, this is not representative of the real $^4He^{2+}$ beam, as the RFQ output optics as well as the beam energy are most certainly significantly different from the proton beam. Therefore, the simulated offset does not reflect the real focusing properties of the $^4He^{2+}$ beam in the IMS but is just a convenient way to identify quadrupole doublet configurations with different focal characteristics.

The result of the scan (see Fig. 6.6) displays optimum beam transport through the IH-tank for a simulated IH-tank entrance offset of +35 mm with respect to the design IH-tank entrance position. At this optimum the measured beam current on LI-00-001-CTA was approximately 160 µA.

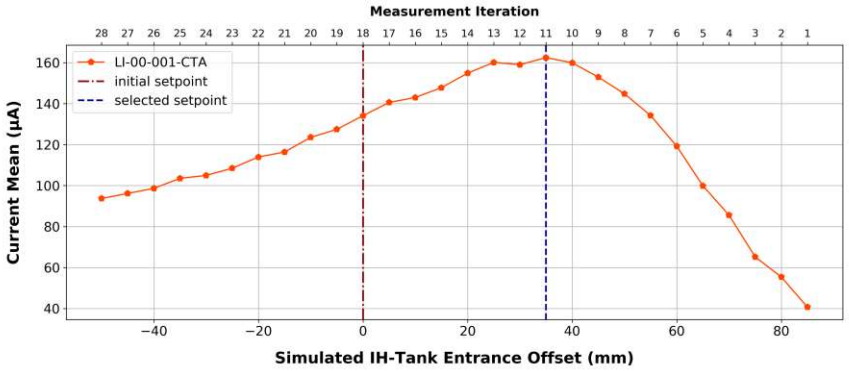

Fig. 6.6: Shifting focal point scan of IMS quadrupole doublets. As the simulations are not representative of the real ion beam, the simulated IH-tank entrance offset does not reflect the real focal point, but just allows for a convenient identification of quadrupole doublet configurations which feature different focal characteristics.

6.3.2 IH-Tank Transport Optimizations

Subsequent to the optimization of the injection into the IH-tank, the focus was shifted to the IH-tank itself, which contains twelve quadrupole magnets grouped into four triplets to counteract the radial defocusing force within the DTL structures (see section 2.3.2 for more details).

Optics Optimization via Quadrupole Scans

For the optimization of the IH-tank quadrupole magnets, multiple scans were performed. Due to the sheer number of scans necessary to optimize nine quadrupole magnets, it is not possible to show each and every one of them within this thesis. However, it shall be stated, that each of the scans featured a pronounced optimum, that was adapted as setpoint. In this thesis only the applied scans and the final result shall be discussed.

As a first optimization attempt, all IH-tank quadrupole magnets were scanned simultaneously around the initially applied (rescaled) setpoint. These scans served the purpose of identifying significant over- or underfocusing of the beam within the IH-tank. The results of this scan show that the optimum is found at the initial (rescaled) setpoint. This implies that no severe over- or underfocusing is present in the IH-tank.

A second approach focused on scanning the three quadrupole triplet strengths separately, i.e. performing three separate scans, one for each triplet, similarly to the scan of the last triplet in the LEBT (see section 5.4.1). After performing this scan and the consequent adaptation to the optimum setpoints, the quadrupole magnet strengths were scanned completely separate from one another.

A third optimization step, consisted of nine single quadrupole strengths scans. Eventually, a beam current of approximately 190 µA was measured on LI-00-001-CTA after the applied optimizations.

6.3.3 Optimizations downstream of the IH-Tank

The final step of the LINAC commissioning was the adaptation of the last LINAC quadrupole triplet, situated after the IH-tank, in order to fit the beam through the small beam pipe aperture at the position of the stripping foil (Fig. 6.1: LI-00-000-FOI). The aperture commissioning at the stripping foil is essential as it allows for optimizing the transport into the MEBT. In terms of the stripping foil itself, it was decided to keep it in the beam path for helium operation even though the $^{4}He^{2+}$ ions are already fully ionized. There are two main reasons for the choice of keeping the stripping foil in the beam path.

Firstly, after the stripping foil, the carbon beam consists of $^{12}C^{6+}$ atoms, which exhibit a charge-to-mass ratio of $1/2$. Therefore, an initial setpoint for the commissioning of $^{4}He^{2+}$

beam after the stripping foil can be found by applying the already commissioned carbon setpoint. In order to ensure that the incoming beam of both ion types is as similar as possible, the stripping foil was left in the beam path, so potential effects of the stripping foil on the beam act on both ion beam types. Secondly, leaving the stripping foil in the beam path reduces switching times between the operation of proton, carbon and helium beams.

Aperture Commissioning at the Stripping Foil

The aperture commissioning at the stripping foil made use of Trace3D beam dynamics simulations, with the aim of finding a setpoint for the last LINAC quadrupole triplet (Fig. 6.1: LE-00-013-MQF, LE-00-014-MQD and LE-00-015-MQF) that ensures a sufficiently small aperture at the stripping foil position. In preparation to this optimization the MEBT elements were preliminary set up according to the already commissioned carbon setpoint and roughly steered using the available corrector dipoles in the MEBT. The simulation input Twiss parameters and emittances were extracted from an emittance measurement in the MEBT section, that was subsequently backtracked to the exit of the IH-tank, while the simulation input energy was chosen as the nominal energy of 7 MeV/u after the IH-tank.

The success of the aperture commissioning by application of the Trace3D simulation was assessed by checking the transported beam current to the first current transformer within the MEBT (ME-03-000-CTA). Prior to applying the simulated setpoint, i.e. with strength of the last IH-tank triplet according to the previous optimization efforts, a beam current of around 170 µA was measured on ME-03-000-CTA. Application of the simulated setpoint to the last triplet allowed for a beam of around 185 µA on ME-03-000-CTA, which corresponds to over 90 % transmission into the MEBT. Considering that the MEBT was not properly set up, this result is surprising and gives hope for very efficient commissioning of the rest of the accelerator with the carbon settings as initial setpoint.

6.4 Final LINAC Setpoint

After the optimizations, the final LINAC setpoint exhibits a transmission of around 60 % from the end of the LEBT into the IMS and a transmission of around 56 % through the IH-tank. The total transmission through the LINAC is around 34 %. These results are far below what is achieved for proton and carbon. However, considering that the RF cavities are not designed for the charge-to-mass ratio of $^{4}He^{2+}$ beam, these results are satisfactory. The performance of the final setpoint is shown in Tab. 6.1.

Monitor	Current (µA)	Part./s	Part. in Pulse	Transmission (%)
LE-01-000-CTA	570	$1.7 \cdot 10^{15}$	$8.8 \cdot 10^{10}$	-
LI-00-000-CTA	345	$1.1 \cdot 10^{15}$	$5.1 \cdot 10^{10}$	60
LI-00-001-CTA	193	$6.0 \cdot 10^{14}$	$2.9 \cdot 10^{10}$	56

Tab. 6.1: Beam current and particle numbers after LINAC commissioning.

6.4.1 Beam Pulse Structure

Similar to the consideration for the final LEBT setpoint, the stability of the beam pulse in terms of intensity can be studied via current transformer measurements. Representative measurements on LI-00-000-CTA and LI-00-001-CTA, shown in Fig. 6.7, confirm that the beam pulse intensity is sufficiently stable in the IMS as well as after the IH-tank.

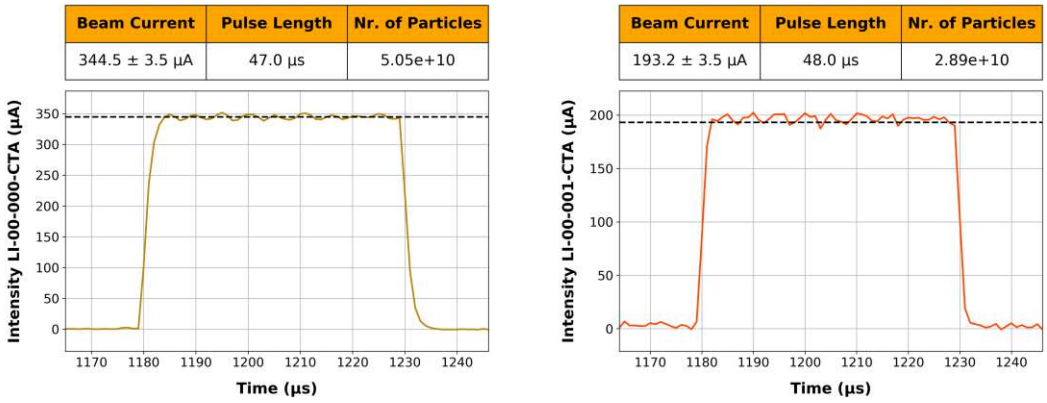

Fig. 6.7: Beam pulses on LINAC current transformers. Measurement on LI-00-000-CTA (left) and LI-00-001-CTA (right). The time is given relative to respective measurement trigger command.

With the much finer resolution of the phase probe measurements available after the IH-tank, it is possible to resolve the microbunch structure of the beam pulse and thus verify that the transport through the LINAC gives a properly bunched beam pulse. In Fig. 6.8 a measurement on the phase probe after the IH-tank (Fig. 6.1: LI-00-001-PHP) is shown. The periodicity of the signal is expected to be around four nanoseconds as this corresponds to the period of the RF oscillation. The fact that the periodicity of the measurement signal is in good agreement with this value hints at a proper acceleration through the LINAC section. Note that this result is not *a priori* expected, due to the design of the RF cavities for different charge-to-mass ratios.

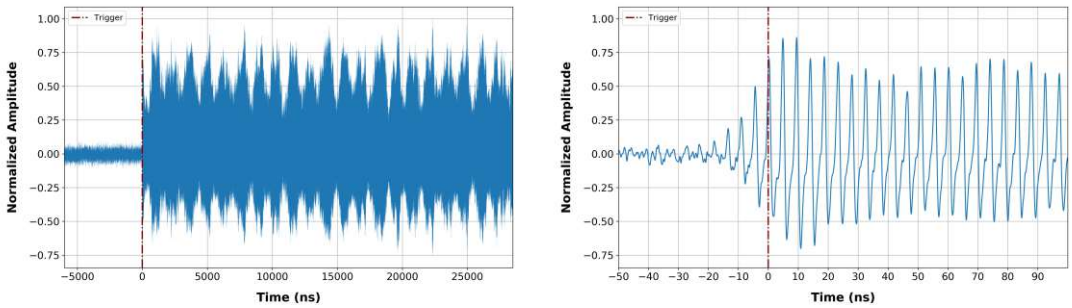

Fig. 6.8: Beam pulse on phase probe detector (LI-00-001-PHP). The time axis is given relative to respective measurement trigger command. The amplitude was normalized to the maximum measured value. Beam pulse over the whole measurement range of the oscilloscope (left). Zoomed start of the beam pulse. Beam bunches of are visible in the periodicity of the measurement signal (right).

6.4.2 Beam Energy

In contrast to the IMS, the phase probes after the IH-tank enable to determine the beam energy. The back-end electronic hardware used for the measurement was a development setup [34], allowing to measure the TOF beam energy over the whole pulse via two phase probes (LI-00-001-PHP and the first phase probe of the MEBT, ME-00-000-PHP). The energy after the IH-tank was found to be around 7.1 MeV/u. Even though the measured energy is slightly higher than the nominal IH-tank output energy of 7 MeV/u, this result is sufficiently close to the nominal energy and thus can be accepted. However, an optimization of the IH-tank output energy might still be necessary when commissioning the helium beam injection into the synchrotron.

In Fig. 6.9 a representative result of the phase probe TOF measurement for the 50 µs helium pulse is shown. The mean energy is at around 7.098 MeV/u, while the fluctuations range from approximately 7.091 to 7.103 MeV/u. This corresponds to $\Delta E/E$ of around $1.7 \cdot 10^{-3}$, which is overall sufficiently stable for the further commissioning efforts.

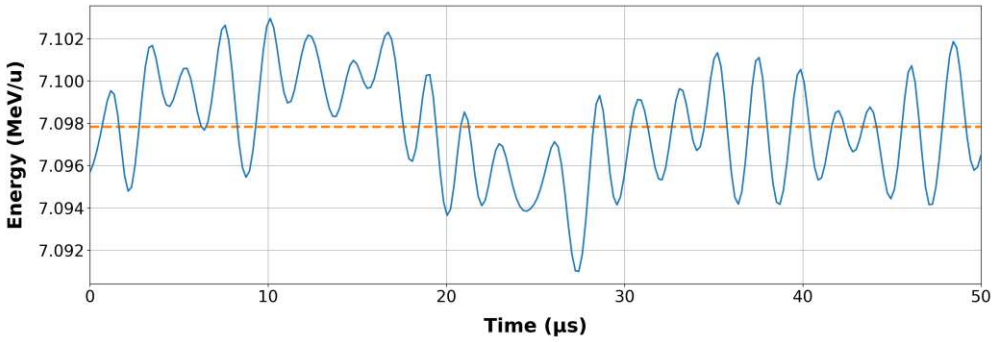

Fig. 6.9: Energy acquired downstream of the IH-tank using TOF measurements.

6.4.3 Reproducibility

The reproducibility of the helium beam in the IMS and after the IH-tank, was assessed as in the source branch and LEBT. However, due to the limited beam diagnostics instrumentation within the LINAC, the reproducibility can only be verified through intensity measurements on the current transformers in the IMS and after the IH-tank as well as by TOF energy measurements after the IH-tank.

Intensity Reproducibility and Stability

Figure 6.10 shows the results of the intensity reproducibility measurements on the two current transformers in the LINAC. While the shot-to-shot stability evident (right plots in Fig. 6.10), the intensity is not fully reproducible over a longer period of time (left plots in Fig. 6.10). Especially, the drop of beam current on LI-00-001-CTA from almost 200 µA (2022-07-03) to approximately 180 µA (2022-07-30) questions the reproducibility of the selected setpoint. This drop was caused due to some beam centering efforts on the last LINAC corrector (Fig. 6.1: LI-00-002-CTA) in the course of the MEBT commissioning. On the 24th and 25th of August 2022, the RF amplifier of S3 was malfunctioning resulting in non-reproducible plasma conditions within the ECR ion source and consequently non-reproducible beam with high intensity fluctuations over the entire source branch LEBT and LINAC section.

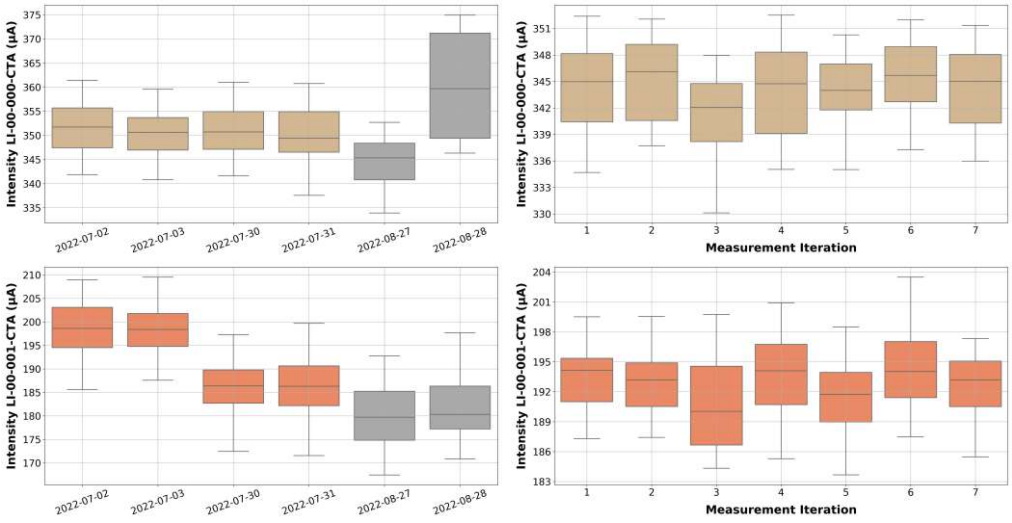

Fig. 6.10: Intensity reproducibility and stability measurements on LINAC current transformers. Measurement on LI-00-000-CTA (top) and LI-00-001-CTA (bottom). Reproducibility measurements measured on different occasions (left) and stability of the intensity over multiple beam pulses measured immediately after one another (right). The measurements indicated in gray are not reliable due to malfunction of the ion source.

Beam Energy Stability

The preliminary TOF setup used to measure the beam energy after the RFQ was only available during one of the beam commissioning shifts. For this reason no long term stability of the measured energy can be presented at this point. Although there is an alternative procedure to measure the energy via TOF, it was decided against applying it, as the analysis of the flight time as well as the calculation of the beam energy has to be performed manually, which is prone to error. However, during the availability of the new TOF setup [34] (see also section 3.2), measurements over several beam pulses were performed to ensure that the energy does not significantly change between different beam pulses.

Figure 6.11 shows the beam energies of twenty individual beam pulses. The extracted energies over each beam pulse were condensed into boxplots, similarly to the representation of the intensity reproducibility. Overall, the energy output of the IH-tank appears very stable over the measured pulses.

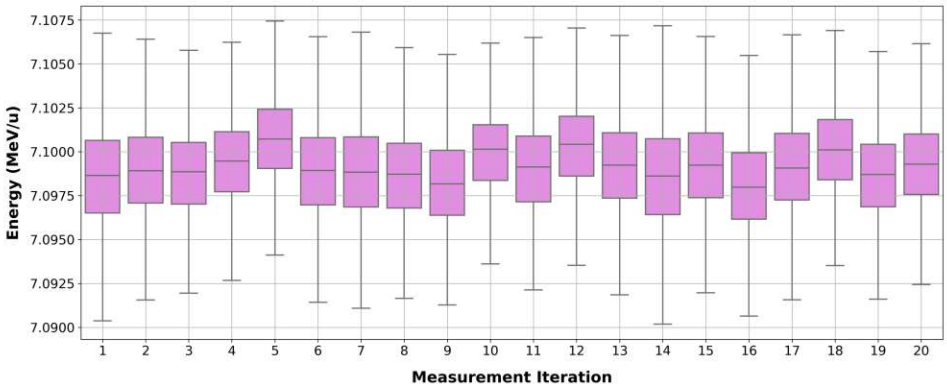

Fig. 6.11: Beam energy reproducibility measurements

6.5 Summary: LINAC Commissioning

The LINAC was commissioned for acceleration of $^4He^{2+}$ beam to 7 MeV/u. The commissioning procedure included the application of an initial setpoint, which served as starting point for beam-based optimizations. This initial setpoint was retrieved from rescaling the proton setpoint used for clinical operation to the charge-to-mass ratio of the $^4He^{2+}$ ions. The RF cavity parameters were optimized for optimum transmission efficiency. The beam optics and steering in the Intertank Matching Section (IMS) were optimized for proper injection into the IH-tank. Within, the IH-tank, the available quadrupole triplets were optimized for transmission efficiency. The first quadrupole triplet after the IH-tank was used to commission the helium beam to the small beam pipe aperture

at the position of the stripping foil. The final LINAC setpoint was characterized in terms of beam current, beam pulse structure and beam energy. Reproducibility measurements were performed. A summary of the LINAC commissioning procedure is shown in Fig. 6.12.

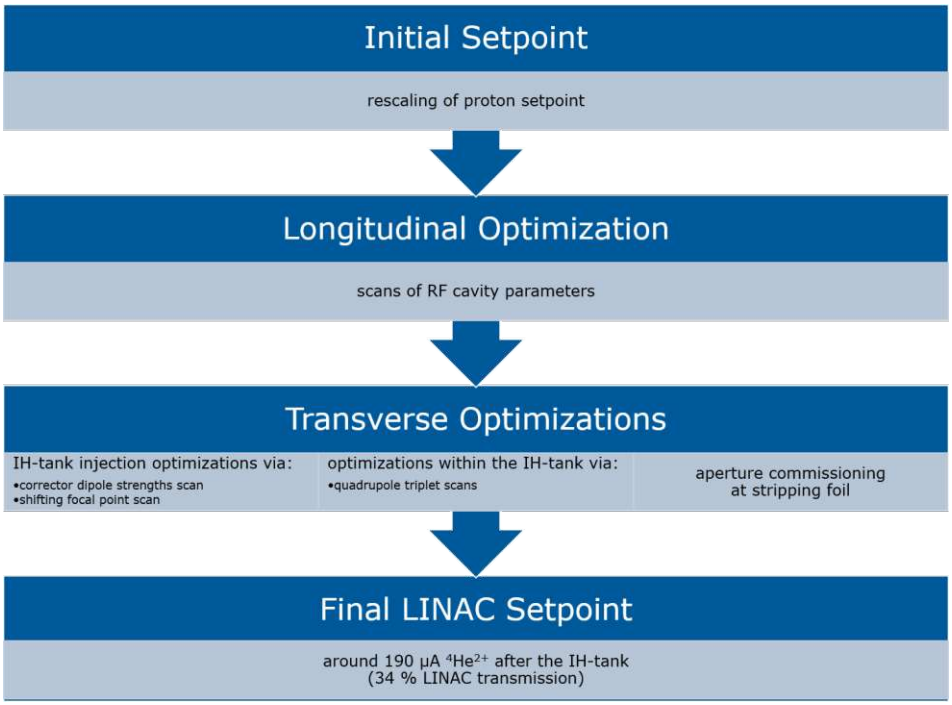

Fig. 6.12: Summarized LINAC commissioning procedure.

7 Conclusion and Outlook

The commissioning of $^4He^{2+}$ beam in the MedAustron injector marks a first major milestone of providing helium ion beam at the MedAustron facility. Once the commissioning is completed, the MedAustron accelerator will be one of few facilities world-wide that deliver helium for clinical and research purposes. In the course of this diploma thesis, the author assisted the local commissioning team in the setup of the source branch, the Low Energy Beam Transfer Line (LEBT) and the Linear Accelerator (LINAC).

The source commissioning focused on delivering a high intensity, stable and reproducible $^4He^{2+}$ beam into the LEBT utilizing an adapted initial setpoint taken from the clinical proton operation. Optimizations to the source setpoint, the optical elements and the beam trajectory allowed to extract approximately 640 µA of $^4He^{2+}$ beam. The beam purity was verified via a spectrum measurement. However, due to limited instrumentation more tests on potential contamination have to be performed. The reproducibility of the setpoint was ascertained by multiple intensity, beam trajectory and emittance measurements. These measurements were obtained utilizing a reliable workflow at the beginning of each commissioning shift (beam quality assurance, Beam QA).

The LEBT section was initially set up using magnet strengths provided by Trace3D beam dynamics simulations aiming for optimum transport and matching to the acceptance criteria of the RFQ. Subsequent optimizations to the beam steering and optical properties allowed for a beam intensity of around 570 µA on the current transformer at the end of the LEBT. This corresponds to a LEBT transmission of approximately 89 %.

The initial LINAC setpoint was obtained by rescaling the applied voltages on the RF cavities and the strengths on the magnets taken from the clinical proton setpoint. While this initial setpoint only transported 20-30 µA of helium beam through the LINAC, beam-based optimizations of the cavity RF parameters as well as the beam steering and beam optics elements increased the beam intensity to 190 µA on the current transformer at the end of the LINAC lattice. This corresponds to a transmission of around 34 % through the whole LINAC, which is satisfactory considering that the RF cavities within the LINAC are designed for proton and carbon beam. The output energy was verified to be at around 7.1 MeV/u via time of flight (TOF) measurements. This is sufficiently close to the nominal output energy of 7 MeV/u.

In Tab. 7.1 the measured helium beam intensities after the LINAC commissioning are summarized.

Monitor	**Position**	**Current (µA)**	**Transmission (%)**
S3-00-000-FCN	after S3 spectrometer	640	-
LE-01-000-CTA	end of LEBT	570	89
LI-00-001-CTA	after IH-tank	193	34

Tab. 7.1: Measured beam currents after LINAC commissioning.

Subsequent to the LINAC setup, the helium commissioning continued with the transport optimization through the Medium Energy Beam Transfer Line (MEBT). As after the stripping foil located at the end of the LINAC lattice, the charge-to-mass ratio of the helium ions ($^{4}He^{2+}$) is identical to the one of the carbon ions ($^{12}C^{6+}$), the initial setup for the MEBT can be easily achieved by applying the clinical carbon configuration. This procedure promises an efficient further helium commissioning along the MEBT, within the synchrotron and the High Energy Beam Transfer Line (HEBT) into the non-clinical irradiation room (IR1), where the helium beam is planned to be available by the end of 2024. The potential clinical application of helium beam is still to be evaluated within the next years.

Appendix

Appendix A: Equations of motion in curvilinear reference system

Curvilinear Reference System

In beam dynamics it is practical to choose a coordinate system, which is moving with the reference (also referred to as design) particle. The particle movement can consequently be described as deviation from this reference trajectory.

Mathematically the curvilinear coordinates can be expressed in a Frenet-Serret coordinate system. The latter has one axis always parallel to the design beam path as well as a normal and a binormal axis. An illustration of this reference system is shown in Fig. 2.1. In order to get a transformation law from the cartesian to the curvilinear coordinate system, one firstly notes that the reference path vector $\boldsymbol{r}_0$ as well as the deviation from the design path $\delta\boldsymbol{r}$ can be uniquely parameterized by the length of the design beam path up to the element of interest s as follows.

$$\boldsymbol{r}(s) = \boldsymbol{r}_0(s) + \delta\boldsymbol{r}(s) \tag{A.1}$$

It can be shown that a right-handed coordinate system which moves along a piece-wise flat trajectory, i.e. a curve with vanishing torsion, can be defined as follows.

$$\boldsymbol{u}_{x_s}(s), \qquad \boldsymbol{u}_{y_s}(s) = \boldsymbol{u}_{x_s}(s) \times \boldsymbol{u}_s(s), \qquad \boldsymbol{u}_s(s) = \frac{d\boldsymbol{r}_0}{ds} \tag{A.2}$$

Here, $\boldsymbol{u}_s$ is a unit vector tangential to the reference particle trajectory, $\boldsymbol{u}_{x_s}$ is a unit vector that is perpendicular to $\boldsymbol{u}_s$ and lies in the plane of the trajectory and $\boldsymbol{u}_{y_s}$ is the binormal unit vector to $\boldsymbol{u}_s$ and $\boldsymbol{u}_{x_s}$. Deviations from the reference beam trajectory $\delta\boldsymbol{r}$ can be expressed solely by the transverse coordinates of this coordinate system x_s, y_s. Therefore, one can write the location vector as follows.

$$\boldsymbol{r} = \underbrace{\boldsymbol{r}_0(s)}_{\text{ref. path}} + \underbrace{x_s(s)\boldsymbol{u}_{x_s}(s)}_{\text{hor. deviaiton}} + \underbrace{y_s(s)\boldsymbol{u}_{y_s}(s)}_{\text{ver. deviation}}, \tag{A.3}$$

The transformation law can be obtained by differentiating this relation with respect to s.

$$\begin{aligned}\frac{d\boldsymbol{r}}{ds} &= \frac{d\boldsymbol{r}_0}{ds} + \frac{dx_s}{ds}\boldsymbol{u}_x + x_s\frac{d\boldsymbol{u}_{x_s}}{ds} + \frac{dy_s}{ds}\boldsymbol{u}_{y_s} + y_s\frac{d\boldsymbol{u}_{y_s}}{ds} \\ &= \boldsymbol{u}_s + \frac{dx_s}{ds}\boldsymbol{u}_x + x_s\frac{d\boldsymbol{u}_{x_s}}{ds} + \frac{dy_s}{ds}\boldsymbol{u}_{y_s} + y_s\frac{d\boldsymbol{u}_{y_s}}{ds}\end{aligned} \tag{A.4}$$

The derivatives of $\boldsymbol{u}_{x_s}$ and $\boldsymbol{u}_{y_s}$ are correlated to $\boldsymbol{u}_s$ via the Frenet-Serret formulas.

$$\frac{d\boldsymbol{u}_{x_s}}{ds} = \kappa_x\boldsymbol{u}_s, \qquad \frac{d\boldsymbol{u}_{y_s}}{ds} = \kappa_y\boldsymbol{u}_s, \qquad \frac{d\boldsymbol{u}_s}{ds} = -\kappa_x\boldsymbol{u}_x - \kappa_y\boldsymbol{u}_y \tag{A.5}$$

Here, κ_x and κ_y are the curvatures of the reference beam trajectory in the respective planes. As the reference trajectory is assumed to have vanishing torsion, either κ_x or κ_y is equal to zero depending on the plane in which the design beam path lies. Insertion of these relations into Eq. (A.4) and subsequent "multiplication" with ds yields the transformation law

$$d\boldsymbol{r} = \boldsymbol{e}_x dx + \boldsymbol{e}_y dy + \boldsymbol{e}_z dz = \boldsymbol{u}_{x_s} dx_s + \boldsymbol{u}_{y_s} dy_s + \boldsymbol{u}_s h ds. \tag{A.6}$$

Here, the abbreviation $h = (1 + \kappa_x x_s + \kappa_y y_s)$ has been introduced. It is evident that for straight elements, i.e. $\kappa_x, \kappa_y = 0$, the curvilinear reference system coincides with a cartesian reference system. In further considerations x_s will be referred to as the horizontal and y_s as the vertical component. Furthermore, the index s will be omitted for the transverse curvilinear coordinates to enhance readability.

A more detailed derivation can be found in [9] and [10] on which this section is based.

Transverse Equations of Motion

The following derviation of the equations of motion and their linearization in the next two sections closely follows the one in [10].

Particles in beam transport structures experience the Lorentz force due to electric and magnetic fields. The Lorentz force is given by the following expression

$$\boldsymbol{F} = \frac{d\boldsymbol{p}}{dt} = q(\boldsymbol{E} + \boldsymbol{v} \times \boldsymbol{B}), \tag{A.7}$$

Here, q is the charge of the particle, $\boldsymbol{p}$ its relativistic momentum, $\boldsymbol{E}$ the electric field, $\boldsymbol{B}$ the magnetic induction and $\boldsymbol{v}$ the particle velocity. As often only stationary $\boldsymbol{B}$ fields are used for transverse beam manipulation, $\boldsymbol{E}$ is set to zero. Further noting that $\boldsymbol{p} = m\gamma\boldsymbol{v}$,

with the rest mass m, the relativistic γ and the velocity $\boldsymbol{v}$, gives the following expression. Note, that as magnetic fields cannot accelerate charged particles γ and $|\boldsymbol{v}| = v$ are constants with respect to time.

$$m\gamma\frac{d\boldsymbol{v}}{dt} = m\gamma\frac{d^2\boldsymbol{r}}{dt^2} = q\boldsymbol{v}\times\boldsymbol{B} = q\frac{d\boldsymbol{r}}{dt}\times\boldsymbol{B}, \tag{A.8}$$

This is the equation of motion in terms of general vectors. In accelerator physics, however, the aim is to describe particle motion in terms of the curvilinear reference system introduced in the previous section. In order to write the equations of motion in this curvilinear system, it is useful to transform the left-hand and the right-hand side of Eq. (A.8) separately.

As a first step, σ is defined as a parameter of the real particle trajectory. It can be understood as the length traveled from the beginning of the considered particle motion up to a certain point in time, similar to the parameter s for the design beam path (see also Fig. 2.1). By applying the chain rule the time derivative can be expressed in terms of derivatives of s, one obtains the following relation.

$$\frac{d}{dt} = \frac{d\sigma}{dt}\frac{d}{d\sigma} = v\frac{ds}{d\sigma}\frac{d}{ds} = \frac{v}{\sigma'}\frac{d}{ds} \tag{A.9}$$

Here, the real particle velocity $v = \frac{d\sigma}{dt}$ and the prime as an indication of derivation with respect to s is introduced. These notations will be adopted generally in the following in order to enhance readability. The relation Eq. (A.9) now enables to substitute the time derivatives in Eq. (A.8) with the corresponding derivatives with respect to s. Mathematically, it is possible to do this transformation as there is a one to one correlation between any point in time and the traveled distance of the particle.

$$\begin{aligned}\frac{d\boldsymbol{r}}{dt} &= \boldsymbol{v} = \frac{v}{\sigma'}\boldsymbol{r}' \\ \frac{d^2\boldsymbol{r}}{dt^2} &= \frac{d}{dt}\left(\frac{d\boldsymbol{r}}{dt}\right) = \frac{v}{\sigma'}\frac{d}{ds}\left(v\frac{\boldsymbol{r}'}{\sigma'}\right) = \frac{v^2}{\sigma'^2}\left(\boldsymbol{r}'' - \frac{\sigma''}{\sigma'}\boldsymbol{r}'\right)\end{aligned} \tag{A.10}$$

The derivative $\boldsymbol{r}'$ has already been calculated in Eq. (A.4). If one also uses the definition of $h = 1 + \kappa_x x + \kappa_y y$ from Eq. (A.6), the expression of $\boldsymbol{r}'$ can be simplified to

$$\boldsymbol{r}' = x'\boldsymbol{u}_x + y'\boldsymbol{u}_y + h\boldsymbol{u}_s. \tag{A.11}$$

The second derivative of $\boldsymbol{r}$ with respect to s can be calculated by differentiating $\boldsymbol{r}'$ and considering the product rule, the derivatives of the basis vectors in Eq. (A.5) and $h' = \kappa_x' x + \kappa_x x' + \kappa_y' y + \kappa_y y'$.

$$\begin{aligned} \boldsymbol{r}'' &= x''\boldsymbol{u}_x + x'\boldsymbol{u}_x' + y''\boldsymbol{u}_y + y'\boldsymbol{u}_y' + h'\boldsymbol{u}_s + h\boldsymbol{u}_s' = \\ &= (x'' - h\kappa_x)\boldsymbol{u}_x + (y'' - h\kappa_y)\boldsymbol{u}_y + (x'\kappa_x + y'\kappa_y + h')\boldsymbol{u}_s \end{aligned} \tag{A.12}$$

By inserting $\boldsymbol{r}'$ and $\boldsymbol{r}''$ into the second line of Eq. (A.10), an explicit expression for $\frac{d^2\boldsymbol{r}}{dt^2}$ can be calculated. After some algebraic transformations one can derive the following relation.

$$\begin{aligned} \frac{d^2\boldsymbol{r}}{dt^2} =& \frac{v^2}{\sigma'^2}\left[(x'' - h\kappa_x - \frac{\sigma''}{\sigma'}x')\boldsymbol{u}_x + (y'' - h\kappa_y - \frac{\sigma''}{\sigma'}y')\boldsymbol{u}_y\right] + \\ & \frac{v^2}{\sigma'^2}\left[(x'\kappa_x + y'\kappa_y + h' - \frac{\sigma''}{\sigma'}h)\boldsymbol{u}_s\right] \end{aligned} \tag{A.13}$$

Apart from this time derivative on the left-hand side of equation A.8, the cross product on the right-hand side also has to be evaluated. In order to achieve this, the magnetic field components are written in terms of the curvilinear coordinates. The cross product itself keeps its shape, as the curvilinear reference frame is orthonormal and right-handed.

$$\begin{aligned} \boldsymbol{v} \times \boldsymbol{B} &= \frac{v}{\sigma'}\boldsymbol{r}' \times \boldsymbol{B} = \\ &= \frac{v}{\sigma'}(x'\boldsymbol{u}_x + y'\boldsymbol{u}_y + h\boldsymbol{u}_s) \times (B_x\boldsymbol{u}_x + B_y\boldsymbol{u}_y + B_s\boldsymbol{u}_s) = \\ &= \frac{v}{\sigma'}\left[(y'B_s - hB_y)\boldsymbol{u}_x - (x'B_s - hB_x)\boldsymbol{u}_y + (x'B_y - y'B_x)\boldsymbol{u}_s\right] \end{aligned} \tag{A.14}$$

Now all the components needed in order to write the equations of motion in Eq. (A.8) in the curvilinear reference system are available.

$$\begin{aligned} \boldsymbol{F} = m\gamma\frac{d^2\boldsymbol{r}}{dt^2} &= q\boldsymbol{v} \times \boldsymbol{B} \\ m\gamma\frac{v^2}{\sigma'^2}\left[(x'' - h\kappa_x - \frac{\sigma''}{\sigma'}x')\boldsymbol{u}_x + (y'' - h\kappa_y - \frac{\sigma''}{\sigma'}y')\boldsymbol{u}_y + (x'\kappa_x + y'\kappa_y + h' - \frac{\sigma''}{\sigma'}h)\boldsymbol{u}_s\right] &= \\ = \frac{qv}{\sigma'}\left[(y'B_s - hB_y)\boldsymbol{u}_x - (x'B_s - hB_x)\boldsymbol{u}_y + (x'B_y - y'B_x)\boldsymbol{u}_s\right] & \end{aligned} \tag{A.15}$$

Separating this vector equation into its components and using $p = |\boldsymbol{p}| = m\gamma v$ yields three differential equations.

$$
\begin{aligned}
x'' - h\kappa_x - \frac{\sigma''}{\sigma'}x' &= \frac{q\sigma'}{p}(y'B_s - hB_y) \\
y'' - h\kappa_y - \frac{\sigma''}{\sigma'}y' &= -\frac{q\sigma'}{p}(x'B_s - hB_x) \\
x'\kappa_x + y'\kappa_y + h' - \frac{\sigma''}{\sigma'}h &= \frac{q\sigma'}{p}(x'B_y - y'B_x)
\end{aligned}
\tag{A.16}
$$

In principle these are the transverse equations of motion for a charged particle along a trajectory parameterized by σ in the curvilinear reference system. Of course, in this form, they are not very useful as it is not *a priori* clear how one has to handle σ as well as its derivatives.

In order to use Eq. (A.16) to describe the particle motion within the curvilinear reference system in terms of parameters that are more accessible than σ and its derivatives, one can exploit the fact that the set of equations in Eq. (A.16) is not linearly independent. Therefore, one can eliminate $\frac{\sigma''}{\sigma}$ in the first two differential equations. Consequently, these two equations only depend on σ'. Fortunately, one can further express σ' quiet easily by considering the norm of $\frac{d\boldsymbol{r}}{dt}$ in Eq. (A.10) together with Eq. (A.11).

$$
|\boldsymbol{v}| = \frac{v}{\sigma'}|\boldsymbol{r}'| = \frac{v}{\sigma'}\sqrt{x'^2 + y'^2 + h^2} \quad \Rightarrow \quad \sigma' = \sqrt{x'^2 + y'^2 + h^2} \tag{A.17}
$$

An important deduction from the equations of motion can be found by considering the design beam path. By construction, the transverse curvilinear coordinates x, y as well as their derivatives x', y' are zero for the reference trajectory. As a result, it follows that $h = 1 + \kappa_x x + \kappa_y y = 1$ and thus $h' = 0$. Then, from the third equation of motion, it is immediately apparent that $\frac{\sigma''}{\sigma'} = 0$ and from Eq. (A.17) that $\sigma' = 1$. Thus, for the reference particle trajectory, the first two equations of motion in Eq. (A.16) simplify to the following expressions.

$$
\begin{aligned}
\kappa_x &= \frac{q}{p}B_y(0,0,s) \\
\kappa_y &= -\frac{q}{p}B_x(0,0,s)
\end{aligned}
\tag{A.18}
$$

On the other hand, the local bending radius of a particle in a magnetic field can be obtained by the following expression, which can be easily derived by solving the equations of motions given by the Lorentz force in polar coordinates for $\boldsymbol{E} = 0$ and $\boldsymbol{B} = B\hat{\boldsymbol{e}}_r$.

$$
\rho = \frac{p}{qB} \tag{A.19}
$$

Therefore, it is possible to identify the local curvature as the inverse of the local reference path bending radius, which is in accordance to the differential geometry definition of curvature.

$$\begin{aligned} \kappa_x &= \frac{1}{\rho_x} = \frac{q}{pB_y(0,0,s)} \\ \kappa_y &= \frac{1}{\rho_y} = -\frac{q}{pB_x(0,0,s)} \end{aligned} \tag{A.20}$$

The connection between the design beam path and the magnetic field at the reference orbit position greatly simplifies the design of beam transport lattices as a homogeneous magnetic field can be easily calculated by the desired curvature of the trajectory.

For completeness, the magnetic rigidity shall be mentioned at this point as it is a key parameter in accelerator physics. It is defined as the ratio of the momentum of a particle to its charge.

$$B\rho = \frac{p}{q} \tag{A.21}$$

Linearization of the Transverse Equations of Motion

It is useful to introduce approximations in order to bring the equations of motion into a compact form that allows for analytical solutions.

The transverse equations of motion from Eq. (A.16) can be linearized by only considering the first order terms in x, x', y, y' as well as the particle momentum p and magnetic field $\boldsymbol{B}$. This approach yields a simple form but neglects quadratic or higher-order effects such as momentum dependent focusing (chromaticity) or higher-order multipole components. Furthermore, B_s is assumed to be zero as the focus is set to transverse magnetic fields. The discussion for strictly longitudinal fields with $B_x, B_y = 0$ and $B_s \neq 0$ is analogous but shall not be presented here. Under these prerequisites, the equations of motion can be written as follows.

$$\begin{aligned} x'' - h\kappa_x - \frac{\sigma''}{\sigma'}x' &= -\frac{q\sigma'}{p}hB_y \\ y'' - h\kappa_y - \frac{\sigma''}{\sigma'}y' &= \frac{q\sigma'}{p}hB_x \\ x'\kappa_x + y'\kappa_y + h' - \frac{\sigma''}{\sigma'}h &= \frac{q\sigma'}{p}(x'B_y - y'B_x) \end{aligned} \tag{A.22}$$

In principle one could solve the third equation in Eq. (A.22) for $\frac{\sigma''}{\sigma'}$ and insert the result into the first and second equation in Eq. (A.22). However, it turns out that a

simpler expression can be obtained by approximating σ' with its lowest order Taylor polynomial.

$$\sigma' = h\sqrt{1 + \frac{x'^2}{h^2} + \frac{y'^2}{h^2}} \approx h \quad \Rightarrow \quad \sigma'' \approx h' \tag{A.23}$$

From Eq. (A.23), it is possible to calculate $\frac{\sigma''}{\sigma'}$. As our expansion is of first order, terms, which are of the form $h'\kappa_x x$ and $h'\kappa_y y$, are omitted, as they contain quadratic contributions of the form xx', xy', $x'y$ and yy'. The first order approximation of the ratio of σ'' and σ' is therefore given by the following expression.

$$\frac{\sigma''}{\sigma'} = \frac{h'}{h} = \frac{h'}{1 + \kappa_x x + \kappa_y y} \approx h'(1 - \kappa_x x - \kappa_y y) \approx h' \tag{A.24}$$

In the equations of motion in Eq. (A.22) also the particle momentum appears. As the real particle momentum p is not expected to differ significantly from the designed particle momenta p_0, it can be expressed as the sum of the p_0 and a small contribution $\Delta p = p_0\delta$, where δ is the fractional offset from the reference momentum.

$$p = p_0(1 + \frac{\Delta p}{p_0}) = p_0(1 + \delta) \tag{A.25}$$

As the momentum appears in the denominator in the equations of motion A.22 and the fractional momentum offset δ is small, it is useful to apply a linear approximation via a first order Taylor expansion of the inverse momentum around p_0.

$$\frac{1}{p} = \frac{1}{p_0(1 + \delta)} \approx \frac{1}{p_0}(1 - \delta) \tag{A.26}$$

Inserting these first order approximations into Eq. (A.22) yields the following differential equations.

$$\begin{aligned} x'' - h\kappa_x &= -(1 - \delta)\frac{qh^2}{p_0}B_y \\ y'' - h\kappa_y &= (1 - \delta)\frac{qh^2}{p_0}B_x. \end{aligned} \tag{A.27}$$

However, these equations are still not fully linearized as there are higher order contributions in h^2 as well as B_x and B_y. To linearize these terms, firstly, the magnetic field can be approximated by a Taylor expansion of first order, which can be understood as only taking dipole and quadrupole fields into account.

$$\boldsymbol{B} \approx \boldsymbol{B}_0 + \nabla \boldsymbol{B} \tag{A.28}$$

Here, $\boldsymbol{B}_0 = \boldsymbol{B}(0,0,s)$ is the homogeneous magnetic field and $\nabla \boldsymbol{B} = \nabla \boldsymbol{B}|_{0,0,s}$ is the Jacobian matrix of $\boldsymbol{B}$ along the design particle trajectory. Writing out this equation in terms of its components yields the following expressions.

$$\begin{aligned} B_x &\approx B_{x0} + \left.\frac{\partial B_x}{\partial x}\right|_{(0,0,s)} x + \left.\frac{\partial B_x}{\partial y}\right|_{(0,0,s)} y \\ B_y &\approx B_{y0} + \left.\frac{\partial B_y}{\partial x}\right|_{(0,0,s)} x + \left.\frac{\partial B_y}{\partial y}\right|_{(0,0,s)} y \end{aligned} \tag{A.29}$$

As this field is stationary, the Maxwell equations for stationary magnetic fields in vacuum have to be fulfilled. These equations allow us to immediately eliminate two degrees of freedom in the Taylor expansion in Eq. (A.29).

$$\begin{aligned} \nabla \cdot \boldsymbol{B} = 0 \quad &\Rightarrow \quad \frac{\partial B_x}{\partial x} = -\frac{\partial B_y}{\partial y} \\ \nabla \times \boldsymbol{B} = 0 \quad &\Rightarrow \quad \frac{\partial B_x}{\partial y} = \frac{\partial B_y}{\partial x} \end{aligned} \tag{A.30}$$

The remaining two magnetic field gradients can be transformed into the normalized gradient K_0 and the skew normalized gradient $\overline{K}_0$. The main advantage of using this gradient notation is that the prefactors are condensed into the normalization and the equations of motion appear in a very simple form. Note that this normalization is given by the inverse magnetic rigidity $B\rho$ in Eq. (A.21).

$$K_0 = \frac{q}{p_0}\left(\frac{\partial B_y}{\partial x}\right)\Bigg|_{(0,0,s)} \qquad \overline{K}_0 = \frac{q}{p_0}\left(\frac{\partial B_x}{\partial x}\right)\Bigg|_{(0,0,s)} \tag{A.31}$$

By considering the relation between the curvature and magnetic field at the reference particle trajectory in Eqs. (A.18) and (A.20), the magnetic field approximation can be written as follows.

$$\begin{aligned} B_x &= \frac{p_0}{q}(-\kappa_y + \overline{K}_0 x + K_0 y) \\ B_y &= \frac{p_0}{q}(\kappa_x + K_0 x - \overline{K}_0 y) \end{aligned} \tag{A.32}$$

Insertion of the magnetic field, $h = 1 + \kappa_x x + \kappa_y y$ and the first order approximation of $h^2 \approx 1 + 2\kappa_x x + 2\kappa_y y$ into Eq. (A.27) while only considering terms up to the first order in x, y, x', y' and δ yields the linearized transverse equations of motion. At this point it shall be stated again, that the derivation is only strictly correct for magnets that do not have higher-order multipole components than quadrupole terms. The equations of motion can be expressed as

$$\begin{aligned} x'' + (K_0 + \kappa_x^2)x - \overline{K}_0 y &= \kappa_x \delta \\ y'' - (K_0 - \kappa_y^2)y - \overline{K}_0 x &= \kappa_y \delta. \end{aligned} \tag{A.33}$$

It is immediately evident that the skew normalized gradient $\overline{K}_0$ couples the differential equations. Usually, in a beam transport lattice the quadrupole magnets will be aligned such that the magnetic gradients coincide with the transverse components and the skew normalized gradient vanishes. As also often the deflection is confined to the horizontal plane κ_y can also be set to zero. The resulting simplified equations are given by the following expressions.

$$\begin{aligned} x'' + (K_0 + \kappa_x^2)x &= \kappa_x \delta \\ y'' - K_0 y &= 0 \end{aligned} \tag{A.34}$$

By comparing these differential equations to the well-known ones of a harmonic oscillator, it is evident that the term $(K_0 + \kappa_x^2)x$ has focusing or defocusing properties depending on its sign. This can be understood by considering that this term takes the place of the "restoring force" within the analogy of a harmonic oscillator. The magnetic gradient K_0 is responsible for focusing or defocusing due to the quadrupole components of the magnetic field, whereas κ_x^2 is responsible for the beam focusing due to dipole components, also referred to as weak focusing. Note that as $\kappa_x^2 > 0$ dipole fields always have focusing properties in the bending plane. For the purpose of beam commissioning, K_0 can be set to zero for dipole magnets and κ_x can be assumed to be zero for quadrupole magnets. A stable solution for the horizontal equation of motion can only be found for $(K_0 + \kappa_x^2) > 0$ and for the vertical equation of motion only for $K_0 < 0$. It is immediately evident that this condition cannot be fulfilled by a single dipole or a single quadrupole magnet. Therefore, there is a need for multiple different magnets in the beam transfer lattice. In each of this magnets either κ_x or K_0 will be constant and different from zero depending on if it is a dipole or quadrupole magnet. In the drift spaces in between the magnets K_0 and κ_x are zero as there is no magnetic field present. Therefore, K_0 and κ_0 can be condensed into two discontinuous but piece-wise constant functions as follows.

$$
\begin{aligned}
K_x(s) &= \begin{cases} 0 & \text{if drift space at position given by s} \\ \kappa_x^2 & \text{if dipole magnet at position given by s} \\ K_0 & \text{if quadrupole magnet at position given by s} \end{cases} \\
K_y(s) &= \begin{cases} 0 & \text{if drift space at position given by s} \\ 0 & \text{if dipole magnet at position given by s} \\ K_0 & \text{if quadrupole magnet at position given by s} \end{cases} \\
A_x(s) &= \begin{cases} 0 & \text{if drift space at position given by s} \\ \kappa_x & \text{if dipole magnet at position given by s} \\ 0 & \text{if quadrupole magnet at position given by s} \end{cases}
\end{aligned}
\tag{A.35}
$$

Writing the equations of motion in terms of these functions yields two second order Hill-type differential equations [14], which serve as starting point to the development of transverse linear beam dynamics.

$$
\begin{aligned}
x'' + K_x(s)x &= A_x(s)\delta \\
y'' - K_y(s)y &= 0
\end{aligned}
\tag{A.36}
$$

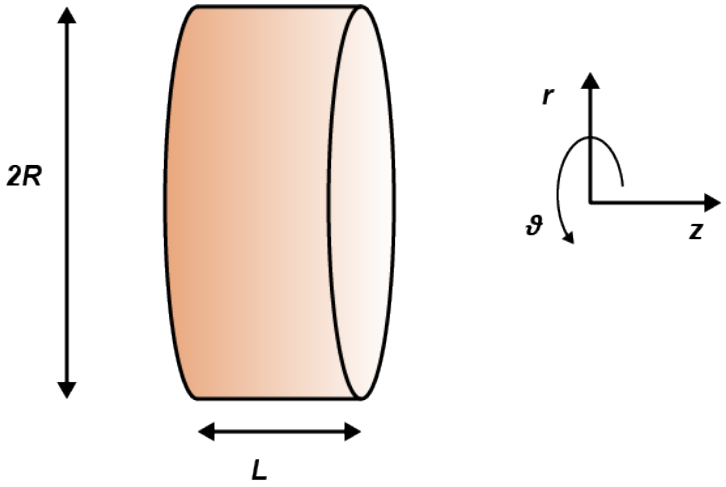

Fig. A.1: Illustration of the pillbox cavity. The cavity consists of a hollow cylinder with radius R and length L. For the mathematical description a cylindrical coordinate system with the z axis along the symmetry axis of the cylinder is chosen. Adapted from Fig. 5 in [24].

Appendix B: The Pillbox RF Cavity

The pillbox RF cavity consists of a cylindrical hollow conductor as seen in Fig. A.1. Even though its mathematical description is slightly more complicated than the one of a simple rectangular box cavity, it is more relevant to the discussion of LINAC structures, as they often feature cylindrical cavities similar to the discussed pillbox cavity.

The derivation of the field configuration within a resonant cavity starts from the electromagnetic wave equations.

$$\begin{aligned} \Delta \boldsymbol{E}(\boldsymbol{r},t) - \frac{1}{c^2}\frac{\partial^2}{\partial t^2}\boldsymbol{E}(\boldsymbol{r},t) = 0 \\ \Delta \boldsymbol{H}(\boldsymbol{r},t) - \frac{1}{c^2}\frac{\partial^2}{\partial t^2}\boldsymbol{H}(\boldsymbol{r},t) = 0 \end{aligned} \tag{A.37}$$

Each of these equations can be separated into a time-dependent and a position-dependent differential equation. Consequently, a separation of variables can be used to derive a solution.

$$\begin{aligned} \boldsymbol{E}(\boldsymbol{r},t) = \boldsymbol{E}(\boldsymbol{r})e^{i(\omega t - \boldsymbol{k}\cdot\boldsymbol{r})} \\ \boldsymbol{H}(\boldsymbol{r},t) = \boldsymbol{H}(\boldsymbol{r})e^{i(\omega t - \boldsymbol{k}\cdot\boldsymbol{r})} \end{aligned} \tag{A.38}$$

These equations describe plane waves propagating in the direction of $\boldsymbol{k}$. Any superposition of these waves is also a solution to the wave equations. The solutions of interest to RF cavities, are the superpositions, that fulfill the boundary conditions for electromagnetic fields at the transition of the vacuum inside the cavity to the conducting walls. The valid solutions have to fulfill the following boundary conditions.

$$\begin{aligned} E_{\parallel}(\boldsymbol{r}_w) &= 0 \\ H_{\perp}(\boldsymbol{r}_w) &= 0 \end{aligned} \tag{A.39}$$

Here, $\boldsymbol{r}_w$ is the position vector on the inner wall of the conducting shell. For the purposes of particle acceleration, one does not have to consider every possible solution. Instead the two major classes of solutions shall be presented, namely the transverse magnetic (TM) and the transverse electric (TE) modes. Per definition the TM modes combine all solutions exhibiting transverse magnetic fields and the TE modes the ones exhibiting transverse electric fields [24, 46]. It can be shown that the solutions for standing waves inside the cavity take the following form in cylindrical coordinates (r, θ, z) [47, 48].

$$\text{TM Modes:} \begin{cases} E_r = -E_0 \frac{p\pi R}{L x_{mn}} \sin\left(\frac{p\pi z}{L}\right) J'_m\left(\frac{x_{mn} r}{R}\right) \cos(m\theta) e^{i\omega^{\mathrm{TM}}_{mnp} t} \\ E_\theta = E_0 \frac{mp\pi R^2}{r L x_{mn}^2} \sin\left(\frac{p\pi z}{L}\right) J_m\left(\frac{x_{mn} r}{R}\right) \sin(m\theta) e^{i\omega^{\mathrm{TM}}_{mnp} t} \\ E_z = E_0 \cos\left(\frac{p\pi z}{L}\right) J_m\left(\frac{x_{mn} r}{R}\right) \cos(m\theta) e^{i\omega^{\mathrm{TM}}_{mnp} t} \\ H_r = i E_0 \frac{m\omega^{\mathrm{TM}}_{mnp} R^2}{c\eta r x_{mn}^2} \cos\left(\frac{p\pi z}{L}\right) J_m\left(\frac{x_{mn} r}{R}\right) \sin(m\theta) e^{i\omega^{\mathrm{TM}}_{mnp} t} \\ H_\theta = i E_0 \frac{\omega^{\mathrm{TM}}_{mnp} R}{c\eta x_{mn}} \cos\left(\frac{p\pi z}{L}\right) J'_m\left(\frac{x_{mn} r}{R}\right) \cos(m\theta) e^{i\omega^{\mathrm{TM}}_{mnp} t} \\ H_z = 0 \end{cases}$$

$$\text{TE Modes:} \begin{cases} E_r = i H_0 \frac{m\eta\omega^{\mathrm{TE}}_{mnp} R^2}{c r x'^2_{mn}} \sin\left(\frac{p\pi z}{L}\right) J_m\left(\frac{x'_{mn} r}{R}\right) \sin(m\theta) e^{i\omega^{\mathrm{TE}}_{mnp} t} \\ E_\theta = i H_0 \frac{\eta\omega^{\mathrm{TE}}_{mnp} R}{c x'_{mn}} \sin\left(\frac{p\pi z}{L}\right) J'_m\left(\frac{x'_{mn} r}{R}\right) \cos(m\theta) e^{i\omega^{\mathrm{TE}}_{mnp} t} \\ E_z = 0 \\ H_r = H_0 \frac{p\pi R}{L x'_{mn}} \cos\left(\frac{p\pi z}{L}\right) J'_m\left(\frac{x'_{mn} r}{R}\right) \cos(m\theta) e^{i\omega^{\mathrm{TE}}_{mnp} t} \\ H_\theta = -H_0 \frac{mp\pi R^2}{r L x'^2_{mn}} \cos\left(\frac{p\pi z}{L}\right) J_m\left(\frac{x'_{mn} r}{R}\right) \sin(m\theta) e^{i\omega^{\mathrm{TE}}_{mnp} t} \\ H_z = H_0 \sin\left(\frac{p\pi z}{L}\right) J_m\left(\frac{x'_{mn} r}{R}\right) \cos(m\theta) e^{i\omega^{\mathrm{TE}}_{mnp} t} \end{cases} \tag{A.40}$$

Here, R and L are the dimensions of the cavity (see Fig. A.1), $\eta = \sqrt{\mu_0/\epsilon_0}$ and $J_m(x)$ is the m-th order Bessel function with its derivative given by $J'(x)$. The n-th root of the m-th order Bessel function is given by x_{nm}. Analogously, the n-th root of the derivative of the m-th order Bessel function is given by x'_{mn}. From the explicit solution, it is evident that the natural numbers n and m define the solution in terms of the radial and azimuthal behavior as they ensure the fulfillment of the boundary conditions for $r = R$ and $\theta \in [0, 2\pi]$. On the other hand p ensures that the boundary conditions are met for the covers of the cylindrical cavity. The resonance frequency depends on m, n and p as well as the type of mode (TM or TE). Instead of a continuous spectrum, only certain frequencies are allowed within the cavity. These resonance frequencies are given by the following expressions.

$$\begin{aligned} \omega_{mnp}^{\mathrm{TM}} &= c\sqrt{\left(\frac{x_{mn}c}{R}\right)^2 + \left(\frac{p\pi}{L}\right)^2} \\ \omega_{mnp}^{\mathrm{TE}} &= c\sqrt{\left(\frac{x'_{mn}c}{R}\right)^2 + \left(\frac{p\pi}{L}\right)^2} \end{aligned} \tag{A.41}$$

The indices m, n and p uniquely identify the field configuration. Therefore, instead of writing down the complex analytical form, the solutions in Eq. (A.40) are conventionally referred to as TM_{mnp} for transversal magnetic and TE_{mnp} for transverse electric modes. This notation is also used for different cavity geometries, e.g. the aforementioned rectangular cavities.

List of Figures

List of Tables

Abbreviations

BD	beam diagnostics
Beam QA	beam quality assurance
CERN	Conseil Européen pour la Recherche Nucléaire
CNAO	Centro Nazionale Adroterapia Oncologica
COG	center of gravity
DC	direct current
DTL	drift tube LINAC
EBG	*german* Errichtungs- und Betriebsgesellschaft
ECR	electron cyclotron resonance
ECRIS	electron cyclotron resonance ion source
FECs	Front End Controllers
FWHM	full-width-half-maximum
GmbH	*german* Gesellschaft mit beschränkter Haftung
GUI	graphical user interface
HEBT	High Energy Beam Transfer Line
HEPHY	Institute for High Energy Physics of the Austrian Academy of Sciences
HIT	Heidelberg Ion-Beam Therapy Center
IH	interdigital H-mode
IH-DTL	interdigital H-mode drift tube LINAC
IMS	Intertank Matching Section
INFN	Istituto Nazionale di Fisica Nucleare
IR1	Irradiation Room 1
IR2	Irradiation Room 2
IR3	Irradiation Room 3
IR4	Irradiation Room 4

KONUS	*german* Kombinierte Null Grad Struktur
LEBT	Low Energy Beam Transfer Line
LINAC	Linear Accelerator
MACS	MedAustron Control System
MAD-X	Methodical Accelerator Design-X
MEBT	Medium Energy Beam Transfer Line
MFC	mass flow controller
MTA	Manufacturer Therapy Accelerator
NCR	Non-Clinical Research
PACMAN	Python Algorithms Coded for Measurement data ANalysis
PTC	Polymorphic Tracking Code
PTCOG	Particle Therapy Co-Operative Group
RAP	rapid alignment procedure
RF	radio frequency
RFQ	radio frequency quadrupole
rms	root-mean-square
S1	Source 1
S2	Source 2
S3	Source 3
SEM	secondary emission monitor
TE	transverse electric
TM	transverse magnetic
TOF	time of flight

Bibliography

[1] B. Jones. "The case for particle therapy". In: *The British Journal of Radiology* 79.937 (2006), pp. 24–31. DOI: 10.1259/bjr/81790390.

[2] Particle Therapy Co-Operative Group (PTCOG). 2022. URL: https://www.ptcog.ch/ (visited on 10/10/2022).

[3] W. Saunders et al. "Helium-Ion Radiation Therapy at the Lawrence Berkeley Laboratory: Recent Results of a Northern California Oncology Group Clinical Trial". In: *Radiation Research* 104.2 (1985), pp. 227–234.

[4] Andrea Mairani et al. "Roadmap: helium ion therapy". In: *Physics in Medicine and Biology* 67.15 (Aug. 2022). DOI: 10.1088/1361-6560/ac65d3.

[5] "Heidelberg Ion Beam Therapy Center treats first patient using helium ion therapy with RayStation". In: *RaySearch Laboratories* (Oct. 2021). URL: https://www.raysearchlabs.com/media/press-releases/2021/heidelberg-ion-beam-therapy-center-treats-first-patient-using-helium-ion-therapy-with-raystation/.

[6] M. Regler. *The Early History of Med-AUSTRON [sic!]* Verein AUSTRON. 2016. URL: http://info.tuwien.ac.at/austron/reports/TheHistoryofMedAUSTRON.pdf (visited on 01/05/2021).

[7] M. Fürtinger. *Master Layout Beamline Elements MAPTA*. MA-1004929. Version 2.0. EBG MedAustron GmbH. Oct. 16, 2019.

[8] O. Triebl. *Naming Convention MAPTA / MAPTA v2*. ES-081117-a-UDO. Version 14.0. EBG MedAustron GmbH. Jan. 17, 2020.

[9] H. Wiedemann. "Elements of Classical Mechanics". In: *Particle Accelerator Physics*. 4th ed. Springer International Publishing AG Switzerland, 2019. Chap. 4, pp. 83–98. DOI: 10.1007/978-3-319-18317-6.

[10] M. Martini. "An Introduction to transverse beam dynamics in accelerators". In: CERN/PS 96-11 (PA) (1998).

[11] B. Holzer. *Introduction to Transverse Beam Dynamics*. CERN. Oct. 4, 2016. URL: https://cas.web.cern.ch/sites/default/files/lectures/darmstadt-2009/holzer-1.pdf (visited on 01/08/2022).

[12] E. D. Courant and H. S. Snyder. "Theory of the alternating-gradient synchrotron". In: *Annals of Physics* 3.1 (1958), pp. 1–48. DOI: 10.1016/0003-4916(58)90012-5.

[13] H. Wiedemann. “Dynamics of Coupled Motion”. In: *Particle Accelerator Physics*. 4th ed. Springer International Publishing AG Switzerland, 2019. Chap. 20, pp. 669–697. DOI: 10.1007/978-3-319-18317-6.

[14] G. W. Hill. “On the Part of Motion of the Lunar Perigee which is Function of the Mean Motions of the Sun and Moon”. In: (Jan. 1886). DOI: 10.1007/bf02417081.

[15] H. Wiedemann. “Particle Beams and Phase Space”. In: *Particle Accelerator Physics*. 4th ed. Springer International Publishing AG Switzerland, 2019. Chap. 8, pp. 213–251. DOI: 10.1007/978-3-319-18317-6.

[16] K. Li. “Collective Effects - an introduction”. In: *CAS - CERN Accelerator School 2021: Introduction to Accelerator Physics*. July 2021. DOI: 10.48550/ARXIV.2107.06109.

[17] J. D. Callen. *Draft Material For ”Fundamentals of Plasma Physics” Book*. 2003. URL: http://homepages.cae.wisc.edu/~callen/ (visited on 10/20/2021).

[18] R. Geller. “Motion in coordinate space containing RF fields and magnetic fields”. In: *Electron cyclotron resonance ion sources and ECR plasmas*. Institute of Physics Publ., 1996. Chap. 1.5.3, pp. 100–105.

[19] R. Geller. “Electron motion in time space”. In: *Electron cyclotron resonance ion sources and ECR plasmas*. Institute of Physics Publ., 1996. Chap. 1.5.4, pp. 105–112.

[20] R. Geller. “Confinement in magnetic mirror fields”. In: *Electron cyclotron resonance ion sources and ECR plasmas*. Institute of Physics Publ., 1996. Chap. 1.6, pp. 115–131.

[21] *Pantechnik - Supernanogan*. 2013. URL: https://www.pantechnik.com/ecr-ion-sources/ (visited on 11/15/2022).

[22] N. Gambino et al. “Commissioning of the MedAustron injector for carbon ion treatment beams”. In: *AIP Conference Proceedings* 2011.1 (2018), p. 090026. DOI: 10.1063/1.5053407.

[23] L. W. Alvarez. “The design of a proton linear accelerator”. In: *Physical Review*. Vol. 70. 9-10. American Physical Society. 1946, pp. 799–800.

[24] A. Degiovanni. “Accelerating Structures”. In: *CERN Yellow Report* (2018). DOI: 10.23730/CYRSP-2017-001.91.

[25] F. Tecker. “Longitudinal beam dynamics”. In: *Proceedings of the CAS-CERN Accelerator School* (2014), pp. 1–22. DOI: 10.5170/CERN-2014-009.1.

[26] T. Wangler. “Longitudinal Particle Dynamics”. In: *RF Linear Accelerators*. John Wiley & Sons, Ltd, 2008. Chap. 6, pp. 175–200. DOI: 10.1002/9783527623426.

[27] T. Wangler. “Transverse Particle Dynamics”. In: *RF Linear Accelerators*. John Wiley & Sons, Ltd, 2008. Chap. 7, pp. 201–231. DOI: 10.1002/9783527623426.

[28] D. Alesini. *Linac*. CERN, 2021. DOI: 10.48550/ARXIV.2103.16500.

[29] T. Wangler. “Radiofrequency Quadrupole Linac”. In: *RF Linear Accelerators*. John Wiley & Sons, Ltd, 2008. Chap. 8, pp. 232–281. DOI: 10.1002/9783527623426.

[30] R. Tiede et al. “KONUS Beam Dynamics Designs Using H-Mode Cavities”. In: *Proceedings of Hadron Beam 2008* (Jan. 2008).

[31] H. Koziol. “Beam Diagnostics for Accelerators; 2005 ed.” In: (2005). DOI: 10.5170/CERN-2005-004.154. URL: https://cds.cern.ch/record/499098.

[32] P. Strehl. “Capacitive Pickups, Basics”. In: *Beam Instrumentation and Diagnostics*. 1st ed. Springer, Berlin, Heidelberg, 2006. Chap. 5.2, pp. 157–179. DOI: 10.1007/3-540-26404-3.

[33] P. Strehl. “Beam Energy Determination by Time of Flight”. In: *Beam Instrumentation and Diagnostics*. 1st ed. Springer, Berlin, Heidelberg, 2006. Chap. 5.3.1, pp. 179–185. DOI: 10.1007/3-540-26404-3.

[34] M. Wolf et al. “Development and Integration of a New Low-Level RF System for MedAustron”. In: *JACoW* LINAC2022 (2022), THPOPA12. DOI: 10.18429/JACoW-LINAC2022-THPOPA12.

[35] A. Wastl et al. “PACMAN- The MedAustron Measurement Data Analysis Framework”. In: *Proceedings of IPAC2016* (2016).

[36] A. Kerschbaum. *Development and Implementation of a new Emittance Analysis Application for the MedAustron Injector Complex*. 2018.

[37] M. Kausel. *PACMAN Injector Emittance Modules: Noise Handling, Analysis and RFQ Acceptance*. 2022.

[38] P. Langhans. *Time of flight analysis for protons and carbon ions in the Medium Energy Beam Transfer Line of MedAustron*. 2020.

[39] H. Grote, F. Schmidt, and L. Deniau. *The MAD-X Program (Methodical Accelerator Design) User’s Reference Manual*. CERN. 2016.

[40] K. R. Crandall and D. P. Rusthoi. *TRACE 3-D Documentation*. 3rd ed. LA-UR-97-886. Los Alamos National Laboratory. 1997.

[41] É. Forest, F. Schmidt, and E. McIntosh. *Introduction to the Polymorphic Tracking Code*. CERN–SL–2002–044 (AP). CERN. Geneva, Switzerland, July 24, 2002.

[42] F. J. Sacherer. “RMS envelope equations with space charge”. In: (Nov. 1970), 17 p. URL: https://cds.cern.ch/record/322516.

[43] N. Gambino et al. “Impact of Ion Source Stability for a Medical Accelerator”. In: *23rd International Workshop on ECR Ion Sources*. 2019. DOI: 10.18429/JACoW-ECRIS2018-MOB2.

[44] U. Ratzinger et al. “Design Study of a 7AMeV RF LINAC”. In: (July 2008).

[45] L. Adler. *MAIPTA-ABC common beam commissioning procedures*. DC033-20301-2101271. Version 0.3. EBG MedAustron GmbH. June 7, 2022.

[46] E. Jensen. “RF Cavity Design”. In: (2014), 25 p. DOI: 10.5170/CERN-2014-009.405.

[47] S. De Silva et al. *Fundamentals of RF cavities*. Thomas Jefferson National Accelerator Facility. June 2016. URL: https://casa.jlab.org/publications/viewgraphs/USPAS2016/L_10_Fundam_RF_Cav.pdf (visited on 01/09/2022).

[48] S. Belomestnykh. *RF basics; TM cavity design and fabrication*. Fermi National Accelerator Laboratory. June 23, 2016. URL: https://casa.jlab.org/publications/viewgraphs/USPAS2016/L_10_Fundam_RF_Cav.pdf (visited on 01/09/2022).